TECHNISCHE UNIVERSITÄT MÜNCHEN

Lehrstuhl für Nanoelektronik

Organic photodiodes for industrial sensing and medical imaging

Francesco Arca

Vollständiger Abdruck der von der Fakultät für Elektrotechnik und Informationstechnik der Technischen Universität München zu Erlangung des akademischen Grades eines

Doktor-Ingenieurs (Dr.-Ing.)

genehmigten Dissertation.

Vorsitzender: Univ.-Prof. Gordon Cheng, Ph.D.

Prüfer der Dissertation:

1. Univ.-Prof. Paolo Lugli, Ph.D.
2. Univ.-Prof. Dr. rer. nat. Franz Kreupl

Die Dissertation wurde am 03.06.2013 bei der Technischen Universität München eingereicht und durch die Fakultät für Elektrotechnik und Informationstechnik am 15.11.2013 angenommen.

to my family

Abstract

In den letzten fünfzehn Jahren wurde verstärkt an amorphen und kristallinen Halbleitern als Röntgendetektor für verschiedene medizinische, sicherheitstechnische und industrielle Anwendungen geforscht. Bisher erhältliche Sensoren basieren vor allem auf amorphem Selen sowie kristallinem oder amorphem Silizium.

In dieser Arbeit wird eine neue Art von Detektor auf Basis organischer Halbleiter beschrieben. Diese Sensoren bestehen aus organischen Photodioden, welche mit einem anorganischen Szintillator kombiniert sind. Der wichtigste Vorteil dieser Technologie besteht darin großflächige Photodioden ohne höhere Kosten herstellen zu können, bei gleichzeitig höherer Sensitivität. Weiter können diese leicht an verschiedenste Röntgenspektren adaptiert werden.

Die Einflüsse von Halbleiter-, Zwischenschicht- und Kathodenmaterial sowie Diodenfläche, Dicke der organischen Schicht und dem benutzen Lösungsmittel auf die Charakteristika der Photodiode werden dargestellt. Der Zusammenhang zwischen Röntgendetektion und Bauelementphysik wird diskutiert.

Abstract

In the last fifteen years there has been much research in using amorphous and crystalline semiconductors as X-ray detectors for different X-ray sensor applications. Up to now many different X-ray sensors are available on the market based on amorphous selenium (a-Se), crystal silicon (c-Si) or amorphous Silicon (a-Si) for medical, security and industrial imaging applications.

In this thesis it is discussed a new class of X-ray sensors based on organic semiconductors. The detectors here presented are organic photodiodes coupled with an inorganic scintillator layer. The main advantages of the organic technology are the large active area fabrication possibility, the low temperature solution processing, the tailored spectral sensitivities possibilities. It is discussed that the dark current is important in the determination of the minimum detectable X-ray radiation dose. Furthermore, it is discussed, how photodiode characteristics such as dark current or external quantum efficiency are influenced by the semiconductor, cathode or interlayer material, the active area of the diode, the thickness of the active layer or the solvent used during the fabrication process.

It is shown the importance of the interface traps in limiting not only the dynamic response but also the sensitivity of the devices. In particular, here is discussed how the dynamic response of the organic diodes can be improved three orders of magnitude at low light intensity by replacing the blocking layers to satisfy the dynamic constraint.

Table of contents

1. Introduction

X-ray detectors exist for over 100 years, however in the last fifteen years the analog chemistry-based film technologies has been gradually replaced by digital solutions. Despite the digital revolution began in the early 1970's with the introduction of the microprocessor, digital X-ray imagers appear only many years later mostly because the lack of suitable X-ray optics requires large-area imaging devices which are harder and more costly to fabricate [Graeve]. Typical market for digital X-ray sensors covers the spectrum from industrial applications such as non-destructive inspection, process monitoring to security inspection, scientific instrumentation and medical imaging.

There are essentially two different techniques to detect X-ray photons namely indirect and direct X-ray conversion. In the indirect conversion devices, a scintillator material is used to generate fluorescence at a wavelength that matches the spectral sensitivity of the X-ray detector. The X-rays are first converted to light via a scintillating phosphor, and then the light emitted by the scintillator is detected by the detector. In direct conversion devices, an X-ray absorber is used as the principal detecting element to convert the incident X-ray photons directly in collectable charge carries.

The X-ray sensors have usually to be devices with large active area due to optic limitations to concentrate more X-ray photons into a small area. In addition, X-ray detection for medical diagnostics requires high X-ray transparent devices for shadow-free images. To reduce the total X-ray absorption of the detector the scintillator layer must be very thin. With typical dose rates such as applied in radiography the X-ray conversion of the thin film scintillator results in an extremely low green emission of a few nW cm^{-2} which requires highly sensitive detectors. Device sensitivity and response time needs to fit to today's digital X-ray imaging systems for medical diagnostics operating at low dose rates of < 1 mGy at energies of typically 70 keV with pulse lengths of ~1 ms.

Organic materials gained increased scientific and industrial interest in the last decade as alternative to solid-state solutions. In particular solution-processed organic

photodiodes (OPDs) are attractive as thin-film alternative for solid-state photosensor due to the cost-effective processing, the possibility to process the OPD at low temperature and to fabricate arbitrary-shaped devices with several cm^2 of active area. Furthermore the physical and chemical characteristics of the organic materials can be tuned with the organic materials to the desiderate application.

In this thesis will be discussed a new class of X-ray sensors based on organic semiconductors. Here, an organic photodiode fabricated by spray-coating technique is coupled with a thin layer of inorganic material for X-ray sensing. In the first part of the thesis light measurements of different organic photodiodes are shown. In particular, it is presented how diodes characteristics such as dark current, external quantum efficiency or dynamic response change with varying the used cathode or interlayer material, the thickness of the active layer, the used solvent or the device active area. It will be demonstrate that the capacitance of the diode and the relative RC time constant is not the limiting parameter for the device dynamic response. In particular diode cut-off frequency at low light intensity deteriorates to a few Hz due to trap states. With replacing the electron blocking layer three orders of magnitude in dynamic response can be gained. Furthermore it is shown that with the spray-coating technique, low intermix occurs between layers of different materials also if the same solvent is used. As an application, an organic photodiode for NIR sensing based on a low band-gap material with P3HT as interlayer is presented.

In the second part of the thesis X-ray measurements are presented. Organic detectors with different stacks are coupled with a thin scintillator layer and irradiated by X-ray photons with different dose rates. It will be show how X-ray sensitivity change with varying the layer stack in agreement with the light measurements. Results match requirements for industrial and medical applications.

Finally, a circuit capable to drive thin diodes with large active area is presented.

Thesis is organized in 6 chapters. In the **chapter 1** motivations for this study and an introduction on X-ray sensing with organic photodiodes is given while in the **chapter 2** working principles and the electrical characterization of a photodiode are presented. At

the end of the chapter 2 organic photodiodes based on the bulkheterojunction are discussed.

In **chapter 3** the used materials, the processing techniques and the characterization methods are presented. In **chapter 4** light measurements are presented. In particular it is discussed how OPD characteristics such as dark and photocurrent, external quantum efficiency or dynamic response are influenced by the interlayer or cathode material, the device area, the used solvent or the thickness of the semiconductor. OPD current drift with time and effect of the temperature on the device are also discussed. In **chapter 5** X-ray measurements are presented and it will be shown that an organic photodiode stacked with a thin scintillator layer can detect X-ray photons.

2. Photodiode Theory

Light is an electromagnetic radiation presenting wave properties but because of its wave-particle duality it behaves as a particle when interacting with a material. Both the wave and the particle properties of the light have to be considered when analysing its interaction with the matter. The particles associated with light, or with any electromagnetic wave, called photons, are characterized by energy directly related to the light wavelength when the radiation is considered as a wave:

$$E_{PH} = \frac{hc}{\lambda} \left[eV\right] \tag{2.1}$$

with h Plank's constant, c the speed of the light in vacuum and λ the wavelength.

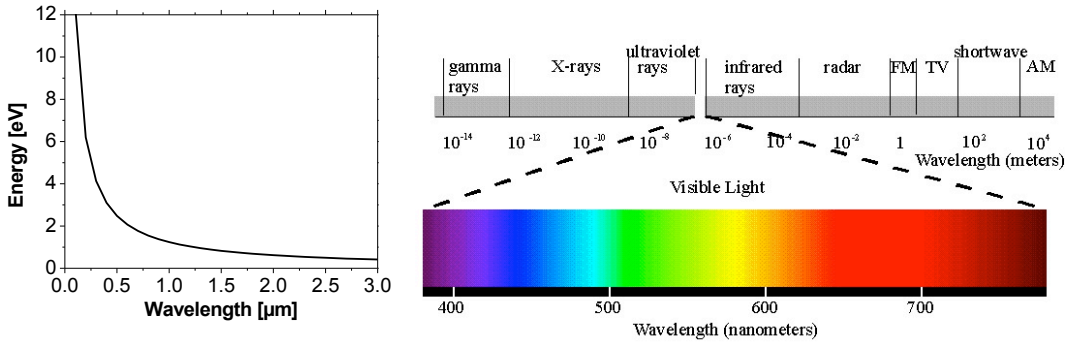

Figure 2.1: a) Photon energy with varying wavelength. b) light spectra.

A large amount of photons make a ray of light, which can be characterized by its wavelength and intensity.

A photodetector (PD) is a device that converts an incident ray of photons into electric current, proportional to the incident ray intensity. Photocurrent is the result of an electron-hole pair generation subsequent to the absorption of the light by the semiconductor material. Since a photodiode generates power due to the photovoltaic effect, it can operate with or without the need for an external power source (a photodiode can operate in both photovoltaic and photoconductive mode).

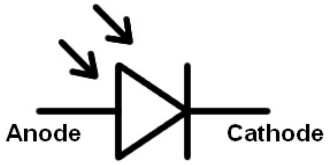

Figure 2.2: Circuital photodiode symbol. The current flows from the anode to the cathode.

In the photovoltaic mode the photodiode is unbiased while for the photoconductive mode an external reverse bias is applied. The two fundamental photodiode circuits are shown in Fig. 2.3. In the photovoltaic mode photodiode works as solar cell and convert light into electrical energy.

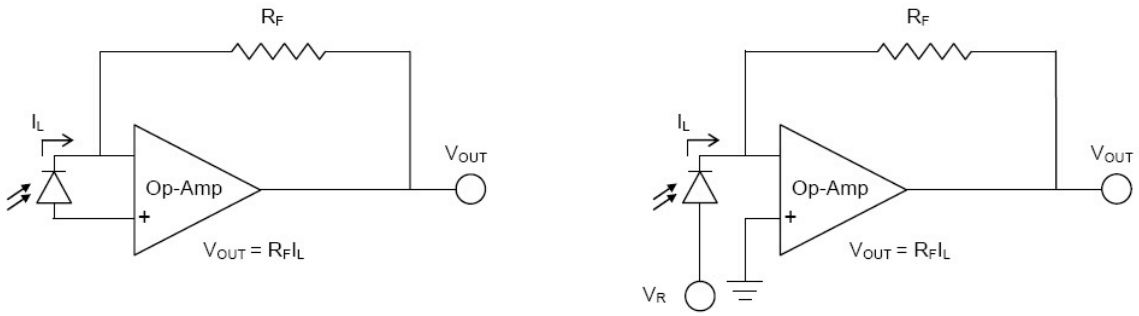

Figure 2.3: Application circuits example of a photodiode a) photovoltaic mode. b) photoconductive mode.

The most common types of photodiodes are PIN, PN, Avalanche photodiode, Schottky photodiode and organic photodiode. Although there are several different types of photodiodes working in many different ways, they all utilize the same physic working principles.

2.1 Photodiode working principle

Every semiconductor material is characterized by a band gap, defined as the energy gap between the valence band and the conduction band. At absolute zero temperature the valence band is completely filled and the conduction band empty. Increasing the

temperature electrons become excited filling partially the conduction band. When light strikes the semiconductor, material electrons are stimulated and, if the photon energy is greater than the band gap energy Eg, electrons are promoted to the conduction band, leaving holes in their place in the valence band.
Both thermal and light excitations generate an electron-hole pair increasing the carrier's density. The resulting electrons in the conduction band and the holes in the valence band can be drifted by an electric field, generating a current.
The depth at which the photons are absorbed depends upon their energy; the lower the energy of the photons, the deeper they are absorbed. In general short wavelength photons (ex. UV) are absorbed in a thin top surface layer while semiconductor becomes transparent to long wavelengths. Moreover, photons with energies smaller than the band gap are not absorbed at all.

The aligned Fermi levels of the two electrodes create a negative internal field $E = -V/d$, known as the built-in field, that helps drive electrons toward the cathode and holes toward the anode. This electric field drives the photogenerated electrons and holes in opposite directions toward their respective electrodes, from where they are then extracted into the external circuit in the form of a current.

2.2 Photodiode electrical characteristics

I-V Characteristic

The current vs. voltage characteristic (IV) observed on a PD in the dark state is similar to the curve of a conventional rectifying diode: when the photodiode is forward biased, there is an exponential increase in the current while when the photodiode is reverse biased a small reverse saturation current is measured.

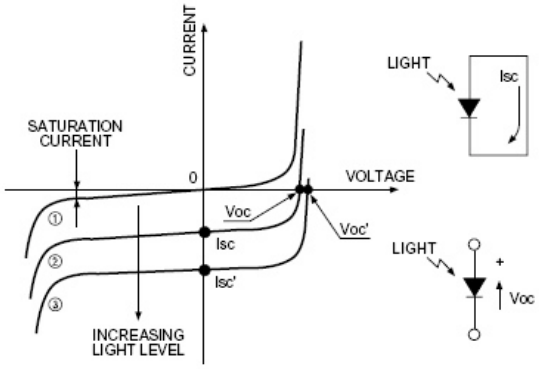

Fig 2.4: Exemplary of an IV measured on a photodiode in the dark (1) and with increasing illumination (2) and (3) [Hamamatsu]. V_{OC} and I_{SC} are depicted in figure.

Three different regions can be identified in the diode IV as function of the applied voltage.

- **V = 0**. In this state no external bias is applied and the photodiode behaves as a solar cell.
- **V>0** In this state the current increases exponentially. This state is also known as forward bias mode.
- **V<0** In this case a reverse bias is applied to the photodiodes and the measured current (saturation) is extremely low, ideally zero.

Contrary to solar cells, photodiodes usually operates with an external bias applied. In general, a reverse bias applied to the photodiode leads to an internal electric field larger in magnitude than the built-in field. This has as benefits an improved photosensitivity and a more rapidly charges sweeps, shortening the device response time.

The ideal diode current-voltage characteristic (Fig. 2.4) in dark is given by the Schottky equation for a rectificating diode

$$I_D = I_S \cdot \left(e^{\left(\frac{q \cdot V}{n \cdot K \cdot T}\right)} - 1 \right) [A] \qquad (2.2)$$

where I_D is the diode dark current, I_S the reverse saturation current, q the electron charge, V the applied voltage, n the ideal factor, K the Boltzmann constant and T the absolute temperature.
When an incident light strikes the photodiode the curve shift by the quantity I_{PH}

$$I_{TOT} = (I_S \cdot e^{(\frac{q \cdot V}{n \cdot K \cdot T})} - 1) + I_{PH} \quad [A] \tag{2.3}$$

where I_{PH} is the photocurrent and depends on the incident light intensity.

As the applied reverse bias increases, an increase in the PD current is usually observed. The negative voltage at which the current increases dramatically is called Breakdown. For organic devices it is usually an irreversible phenomenon (Fig. 2.4).

Finally, when the diode contacts are electrically isolated and the PD illuminated, an open circuit voltage (V_{OC}) is generated with the positive polarity at the anode. Voc can be derived from eq. 2.3:

$$V_{OC} = \frac{\eta KT}{q} \ln\left(\frac{I_{TOT} - I_{PH}}{I_S} + 1\right) \quad [V] \tag{2.4}$$

The quantity $I_{TOT} - I_{PH}$ is usually called short-circuit current (I_{SC}) and represent the current that flow in the device when anode and cathode are shorted (Fig. 2.4).

Dark Current

The dark current, sometimes called leakage current, is the current that flow through the photodiode in absence of light due to the material bulk resistivity. The dark current includes photocurrent generated by background radiation (noise) and the saturation current of the device. Usually, increasing reverse bias across the photodiode will

increase the dark current. Dark current is at a minimum in photovoltaic mode were no voltage is applied to the device.

The dark current for an ideal diode is given by eq. 2.2.

Equivalent Circuit

A PD can be represented by an equivalent electric circuit comprising a current source I_{PH} in parallel with an ideal diode and some parasitic components.

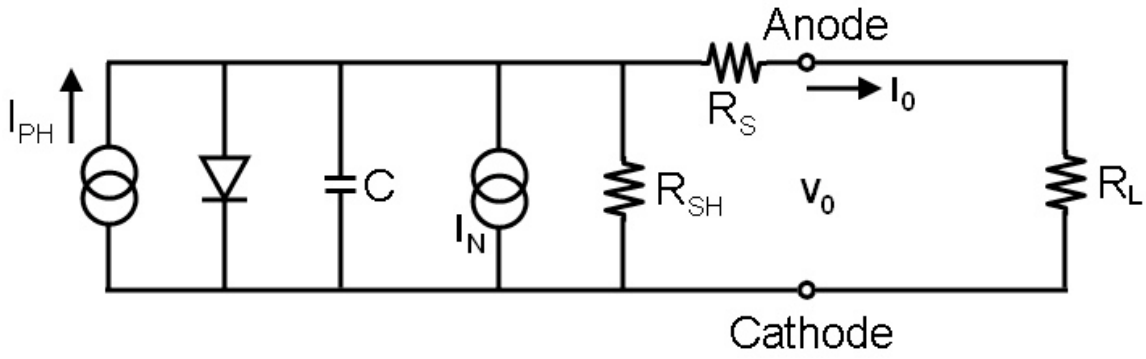

Figure 2.5: Photodiode equivalent circuit.

In Figure 2.5 the photodiode equivalent electric circuit is presented where:

- I_{PH} represent the current generated by the incident light (proportional to the amount of light)
- C is the diode capacitance
- R_{SH} is the shunt resistance (also called parallel resistance)
- R_S is the series resistance
- I_N is the noise current generator
- V_0 is the voltage across the diode
- I_0 is the output current
- R_L is the load resistor.

Series resistance arises from the resistance of the contacts and the semiconductor. Although an ideal photodiode should have null series resistance, typical values ranging from 10 to 1000 ohm are usually measured.

Shunt resistance is the slope of the current-voltage curve of the photodiode at the origin. Despite an ideal photodiode should have an infinite shunt resistance, real values are in the Mega and Giga Ohm range.
The shunt resistance is normally determined by measuring the dark current under a small reverse bias (ex 10 mV)

$$R_{SH} = \frac{-0.01V}{I(-0.01V)} \ [\Omega] \tag{2.5}$$

Due to the usual planar structure, a PD has a capacitance given by:

$$C = \frac{\varepsilon_r \cdot \varepsilon_0 \cdot A}{d} \ \left[\frac{F}{m^2}\right] \tag{2.6}$$

where ε_r is the dielectric constant of the semiconducting material, ε_0 the permittivity of the free space, A the diode area and d the semiconductor thickness. Because PD capacitance affects the device bandwidth, an ideal device should have a capacitance value as low as possible.

The capacitance density is defined as the capacitance per unit area, and is a convenient area-independent measure of the device capacitance. Since the capacitance density is inversely proportional to both the electrode distance and the relative permittivity of the semiconductor, the obvious solution to reduce the value it is to increase either the thickness d or the relative permittivity ε_r of the active layer.

Finally, I_N represent the intrinsic diode noise. The main common sources of noise in PDs are Johnson noise (or thermal noise), shot noise and flicker noise (also known as 1/f or pink noise) [Tedde PhD].

Frequency Response

Photodiode response time is a critical parameter in applications were fast dynamic response is required. Photodiode response is usually characterized in terms of rise-fall times and cut-off frequency. Rise and fall time are defined as the time for the photocurrent to rise or fall from 10% to 90% or 90% to 10% of the final value respectively when a square light pulse is applied. The rise and fall times depend on the wavelength of the incident light. In general the voltage across the PD varies exponentially with time. The voltage profile vs. time is usually given by

$$V(t) = V_0(1 - e^{(-\frac{1}{RC}t)}) \quad [V] \tag{2.7}$$

where R is the diode resistance, C the capacitance and V_0 the final voltage. T = 1/RC is the device time constant.

The time constant measurement is performed by measuring the PD output signal to an input light pulse. A square wave signal is normally applied to the photodiode and the corresponding photocurrent monitored. Time constant is defined as the time that the photocurrent needs to raise form 0 to 63% of its terminal value as shown in Fig. 2.6.

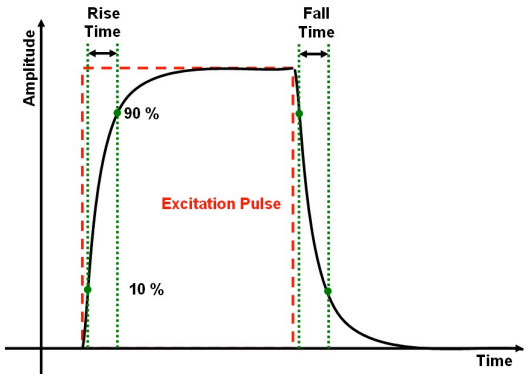

Figure 2.6: Rise and Fall time measurements.

The cut-off frequency (fc) is defined as the frequency at which the amplitude of the photodiode signal falls to $1/\sqrt{2}$ (~70 %) from the output at low frequency. This value can be easily determined by illuminating the photodiode with sinusoidal or square-shape pulse light of fixed amplitude with varying the frequency *f*.

The rise time tr is correlated to the cut-off frequency by:

$$tr = \frac{0.35}{fc} \ [s] \tag{2.8}$$

Cut-off frequency values in the GHz regime for silicon devices [Hamamatsu] and in the kHz regime for organic devices are reported.

For large active area PDs the cut-off frequency in mainly determined by the photodiode capacitance. When the device area become sufficiently small, the response time is no longer determined by the capacitance but by the carriers transit time in the semiconductor (time required for the photogenerated charge carriers to pass through the thickness of the device).

Quantum efficiency

Internal Quantum Efficiency (IQE) is defined as the ratio, in percentage, between the number of the electron-hole pair created by the light and the number of the absorbed photons. Due to different loss mechanisms not all generated carriers reach the electrodes.
Because it is difficult to calculate directly the IQE, the IQE of a photodiode is normally estimated from an external quantum efficiency (EQE) measurement by:

$$IQE(\lambda) = \frac{EQE(\lambda)}{1 - \rho(\lambda) - \tau(\lambda)} \ [\%] \tag{2.9}$$

where ρ(λ) is the spectral reflectance and the device transmittance τ(λ) is usually zero. IQE is 100 % on an ideal device.

EQE is defined as the number of electron-hole pairs that contribute to the photocurrent per incident photons. IQE and EQE are usually expressed in percent as a function of one parameter like wavelength, absorption coefficient or light frequency, as

$$EQE(\lambda) = \frac{I_{PH}}{P}\frac{hc}{\lambda e}\ [\%] \tag{2.10}$$

where I_{PH} is the photocurrent, P the incident light power, h the plank constant, c the light speed in the vacuum, λ the wavelength of the incident light and e the elementary charge.
Optical reflection loss mechanisms, carrier's recombination, material defects, passivating layer thickness and doping levels have been considered as the important parameters that cause the reduction of EQE below the unity (100 %). Operating under ideal conditions of reflectance, crystal structure and internal resistance, a high quality silicon photodiode is capable of approaching an EQE of ~80 %. An EQE of 100 % is not attainable. The quantum efficiency for photons with energy below the band gap is zero since when the energy of absorbed photons is lower than the band gap energy Eg, the photovoltaic effect does not occur. The limiting wavelength λh can be expressed in terms of Eg as follows:

$$\lambda h = \frac{1240}{Eg}\ [nm] \tag{2.11}$$

At room temperatures, Eg is ~1.12 eV for Si and ~1.8 eV for GaAsP, with limiting wavelength of ~1100 nm and ~700 nm, respectively.

The surface coatings usually used to protect the photodiode can affect the spectral response of the device. An anti-reflect coating layer is commonly used but this coating layer may reduce the efficiency at the wavelengths which it reflect. A glass encapsulation window for example absorbs wavelengths shorter than 300 nm.

Finally, it is important to note that in normal working conditions photodiodes generate at most one electron-hole pair for every absorbed photon, however they can be made to exhibit internal gain if they are operated at sufficiently high reverse biases. In this case the photogenerated electrons and holes collide with atoms in the semiconductor crystal, generating secondary carriers, which amplify the current. Such devices are known as avalanche photodiodes and are characterized by an EQE value higher than 100 %.

Responsivity

The responsivity (R) of a photodiode is a measure of its sensitivity to light, defined as the ratio of the diode photocurrent I_{PH} (in Ampere) to the incident light power P (in Watt) at a given wavelength (nm):

$$R(\lambda) = \frac{I_{PH}}{P} \quad \left[\frac{A}{W}\right] \tag{2.12}$$

It is a measure of the effectiveness of the conversion of light power into electrical current. Responsivity varies with the wavelength of the incident light, applied bias and temperature. Usually increases slightly with applied bias due to improved charge collection efficiency in the photodiode.

Responsivity is correlated with the photocurrent. When the photodiode is illuminated by a broadband excitation source, the resultant photocurrent I_{PH} is

$$I_{PH} = \int_{\lambda \min}^{\lambda \max} P(\lambda) \cdot R(\lambda) \cdot d\lambda \quad [A] \tag{2.13}$$

Responsivity is correlated also with the quantum efficiency by the relationship

$$R(\lambda) = \frac{\eta \cdot e}{h \cdot \nu} \tag{2.14}$$

where η is the quantum efficiency, e the electric charge, *h* planck's constant, and *v* the radiation frequency.

Usually high responsivity values are reached in photovoltaic mode (V = 0) due to the low dark current. Most photodiodes work quite good with no applied bias, even those originally designed for reverse-biased operation. Responsivity and quantum efficiency are usually determined by reference to a calibrated photodetector.

Noise Equivalent Power (NEP)

Noise, always presents in any real photodiode, is the parameter that determinates the lower limits of light detection. The PD noise is the limiting parameter of the dark current.
The Noise Equivalent Power (NEP) is defined as the minimum incident power required to generate a photocurrent equal to the noise current of the photodetector at a specified frequency, and within a specific bandwidth.
The NEP for a PD is calculated by the following formula:

$$NEP = \frac{I_N}{R(\lambda)} \left[\frac{W}{H^{1/2}} \right] \tag{2.15}$$

where I_N is the noise current in $A/Hz^{1/2}$ and R is the responsivity for a particular wavelength (λ) [A/W].

The NEP is dependents on the bandwidth of the measuring system; to remove this dependence the value is divided by the square root of the bandwidth. This gives the NEP the units of $Watts/Hz^{1/2}$. Since the photodiode light power to current conversion

depends on the radiation wavelength, the NEP power is calculated to a particular wavelength.

2.3 Bulk-Heterojunction photodiodes

Organic materials and polymers have been extensively studied in the last years to obtain opto-electronic devices. Such materials are attractive for fabrication of solution-processed photodiodes at low temperatures with large active areas even on flexible substrates with a variety of geometrical degrees of freedom. In addition, the spectral sensitivities of the devices can be tailored with the organic semiconductor absorber for the respective application [Rauch 2009]. Efficient organic photovoltaic devices and photodiodes have been demonstrated which involve photoinduced charge transfer across a donor/acceptor heterojunction. Despite photoinduced charge transfer may occur with a low probability in the pristine polymer, efficient charge generation requires the addition of an acceptor [Brabec book 2003]. The junctions are formed with materials with different characteristics, example p- and n- type which favourite exciton dissociation at the interface. Interface can be fabricate in bi-layer architecture or distributed in a blend. Both configurations can be formed by mixing different materials such as polymer/polymer, polymer/molecule or molecule/molecule. In these structures one material donates the electrons to the other material under light excitations. The photogenerated excitons dissociated and the generated free carriers, driven by the internal electric field of the device, are transported to the electrodes where are finally extracted.

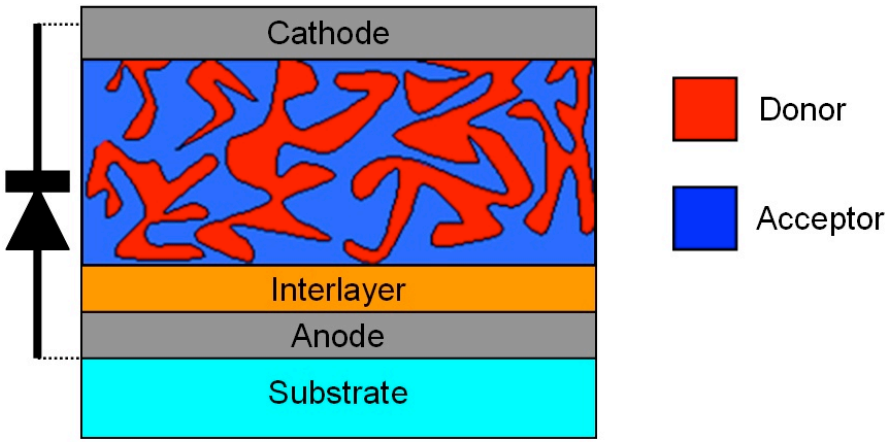

Figure 2.7: Layout scheme of a BHJ photodiode.

Bulk heterojunction (BHJ) photodiodes are usually based on a simple planar geometry, with the blend of donor and acceptor material, usually a BHJ with polymer/fullerene composites as donor/acceptor system to provide interfaces for exciton dissociation, sandwiched between electrodes with different work function for efficient charge extraction. At least one of the electrodes should be transparent or semitransparent to let the light in, while the other electrode is usually mirror reflective. In general, the light absorbing layer is part of the BHJ and the photo-generated carriers are collected at the electrodes. For a charge current to flow through the device, electrons and holes must move in different directions. By convention, for the forward current, holes and electrons must move from the external circuit through the contacts into the device, where they disappear by recombination. For the reverse current, electrons and holes must move out of the device were they were generated [Brabec book 2003]. In case of reverse biased electrodes, photogenerated electrons are collected at the lower work function electrode and photogenerated holes are transported to the higher work function electrode. Electrodes should be close to the place were electron/hole pairs are generated, so they can be reached within the lifetime of the carriers. A scheme of a BHJ based photodiode is shown in Fig. 2.7.

Light conversion into current needs six consecutive fundamental processes [Brabec book 2003] [Tedde PhD]:

1. Absorption of a light photon in the organic semiconductor
2. Formation of an excited states, an electron-hole pair
3. Exciton diffusion to the region where dissociation may occur
4. Dissociation of electron hole pair in free charges
5. Charge transport of holes and electrons to the respective electrodes.
6. Charge extraction at the electrodes

The conversion efficiency of the device is limited by the efficiency of each step.

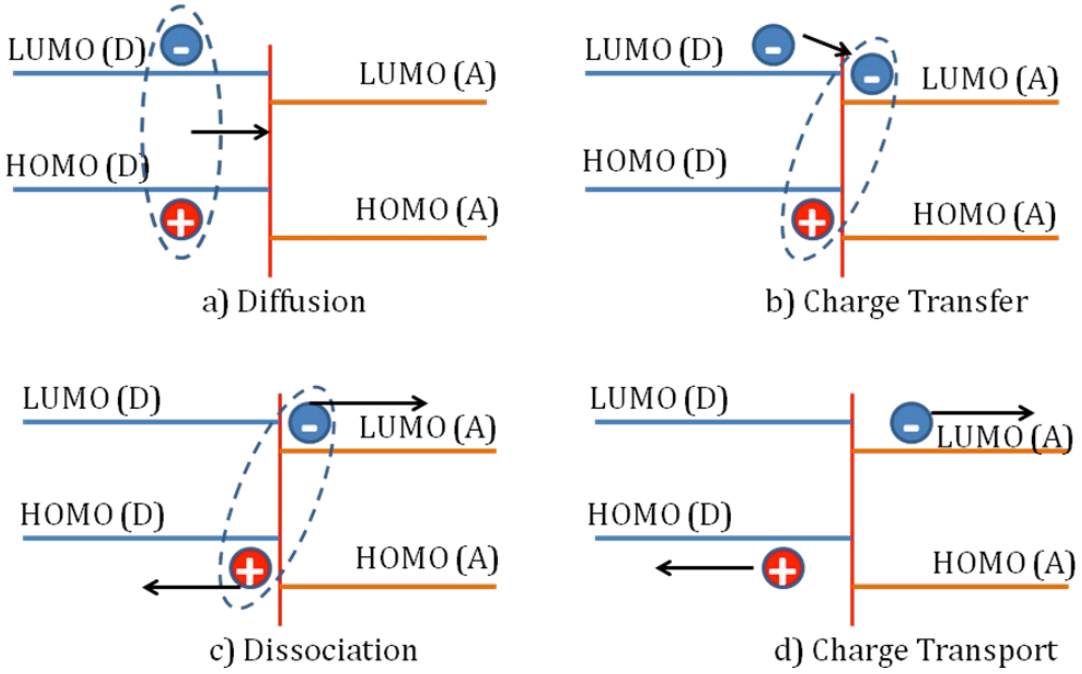

Figure 2.8: Schematic of the light conversion process into current in and organic photodiode with an acceptor (right, orange) and a donor (left, blue) material as semiconductor.

The full process of the conversion of the light into current is schematized in Fig. 2.8.
In details:

1. Absorption of a light photon in the organic semiconductor

The first step is the absorption of the photon and it is usually mostly done by the donor material. Due to the high absorption coefficient of the organic materials (>10^5 m^{-1}) [Schafferhans PhD] film layers of > 200 nm are usually capable to absorbs > 95 % of the incident visible light (my paper konarka). An incident photon is absorbed by the organic material only if it has energy equal or higher than the band gap of the organic semiconductor. Light absorption in organic materials follows the Lambert-Beer law:

$$I = I_0 e^{-\alpha d} \tag{2.16}$$

with d thickness and α absorption coefficient of the photoactive material. I and I_0 are the incident and transmitted light, respectively.

2. Formation of an excited states, an electron-hole pair.

The photon's absorption results in an excited state generation, know as exciton. In this state, electron and hole pairs are tightly bonded by columbic attraction forces. Since the dielectric constant in organic semiconductors is quite low (typically between 3 and 4) the exciton binding energy is quite high. For example, assuming a distance of the electron–hole pairs of 1 nm and a material dielectric constant of 3, the coulomb binding energy is 0.5 eV [Schafferhans PhD], higher than the thermal energy at room temperature that is so not enough to separate the electron and the hole. Life time of an exciton is supposed to be about 100 ps [Zaus 2008], after that electron and hole recombine radiatively resulting in a lost of the photogenerated carriers. For an efficient dissociation of the excitons a second organic semiconductor is used as electron acceptor, to create a PN junction.

3. Exciton diffusion to the region where dissociation may occur

The generated exciton have to diffuses to the PN junction where dissociation in free charges may occur. The exciton diffusion length in conjugated polymers is typically in

the order of a few nm. For example for the P3HT, an exciton diffusion length of about 8 nm is reported [Shaw 2008]. Optimized OPDs adopt usually the concept of Bulk Heterojunction, where the two material are mixed together to create an interpenetrating network that maximize the acceptor/donor interface area for maximum light absorption and at the same time minimize the exciton diffusion path to reach the interface.

4. Dissociation of electron hole pair in free charges

If the exciton reaches the donor/acceptor interface, electron transfer to the acceptor phase is energetically favored yielding a Coulombically bound electron-hole pair. The dissociation of the electron-hole pair produces free charge carriers. At the interface the electron is transferred to the acceptor material while the hole remains in the donor material. In order to dissociate the exciton at the acceptor/donor interface, the energy gain of the charge transfer has to be larger than the electron-hole binding energy.

Exciton decay is a possible charge loss mechanism, while geminate recombination of the bound electron-hole pair and bimolecular recombination of free charge carriers are two other possibilities.

5. Charge transport of holes and electrons to the respective electrodes.

Generated charges at the acceptor/donor interface need to reach the electrodes in order to be extracted. In particular, electrons are collected at the cathode (lower work function electrode) and holes at the anode (higher work function electrode). The charge transport in disordered organic semiconductors occurs via hopping from localized state to localized state. Transport is mainly influenced by the nanomorphology of the material, despite the full pictures is still not clear. It is usually believed that in order to have an efficient charge transport, a single material path to the electrode is needed: the electrons need to reach the cathode traveling only through the acceptor material while the hole need to reach the anode traveling only thought the donor material. Isolated material islands obstacle the charge movement. This is in contradiction with the definition of BHJ where, in order to maximize the interfaces, materials are mixed together and the presence of a single material path from every

interface to the respective electrodes seems not possible. To conclude, it is important to note that material morphology and so the carriers paths can be changed after processing, for example with a post annealing process, in order to optimize the charge transport and maximize the OPD photocurrent [Arca 2013].

6. Charge extraction at the electrodes

The last step is the successful extraction of the charges at their respective electrodes, so holes at the anode and electrons at the cathode. Charge carriers extracted at the wrong electrode are lost and do not contribute to the photocurrent. In order to prevent charge loose, different strategies are adopted. In particular, by judiciously choosing the electrode materials, the injection of one carrier type can be suppressed or enhanced, thereby enabling one to selectively assess either the hole or electron mobility. The way to do this is to make sure that the work function of one electrode is close to the energy level of the transport band, while there exists a large barrier for injection of the other carrier type into the material. For this reason for OPD fabrication electrodes with different work function are adopted. In particular, the cathode is usually choose as a material with a high work function to efficiently extract the hole from the HOMO of the donor material while as anode it is usually used a material with low work function to match the acceptor LUMO. The work function difference between electrodes as well as the electric field generated at the metal-semiconductor interfaces and the electrochemical potential created at the interfaces between materials with different electron affinities and ionization potentials sets up the internal electric field that drift the charges to the respective electrode. Furthermore, OPDs usually operate with external bias to increase the electric field and one or more blocking layers can be inserted in the stack, in order to block the flux on one charge carrier in one direction.

Finally in Fig. 2.9a the flat band energy diagram of an OPD with ITO as anode, P3HT:PCBM blend as semiconductor and Ca as cathode is shown. With varying the applied bias the semiconductor band structure bends.

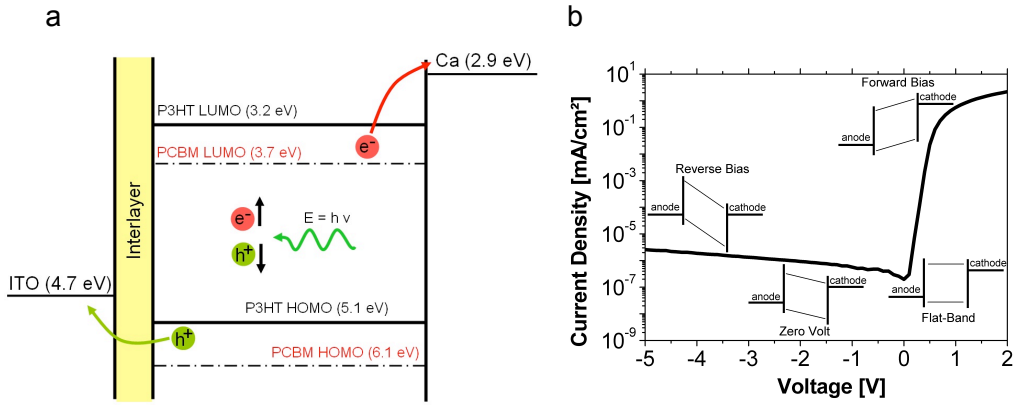

Figure 2.9: a) flat band diagram for an organic photodiode with ITO as anode and Ca as cathode. b) IV characteristic of an organic photodiode in dark. The schematic band diagrams for the different diode regimes are depicted in the figure according to the applied voltage.

In Fig. 2.9b an exemplary IV of a photodiode in the dark is presented. The schematic band diagrams with varying the applied bias are depicted in the figure [Brabec book 2003].

3. Organic materials and experimental methods

In this chapter key properties of the materials adopted to fabricate Organic Photo Detectors (OPD) are presented. Fabrication and characterization methods are also discussed.

Materials

Materials are classified, depending on their conductivity, in conductors, semiconductors and insulators. Conductors allows the passage of electric current, having high conductivity (between 10^4 Ω^{-1} cm and 10^6 Ω^{-1} cm) while the insulators block the charge carriers having a very low conductivity (between 10^{-18} Ω^{-1}cm and 10^{-8} Ω^{-1}cm). Semiconductors, which have conductivity in between of insulators and conductors, allow a flow of charges in them but must be verified special conditions such as temperature, lighting or doping (controlled impurity).

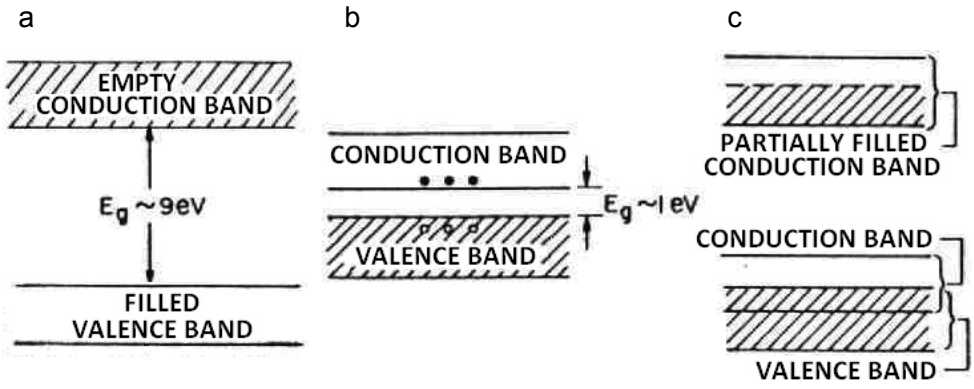

Figure 3.1: Schematic rappresentation of energy's bands in a) insulator, b) semiconductor and c) conductor [Sze book 1969].

In nature the best conductors are represented by the class of metals, which consist of a large number of atoms to create a structure where the conduction band is partially occupied (Fig. 3.1c). Valence's electrons are free to move and usually an applied external electric field, also small, is sufficient to generate a charge drift and thus

electric current. However, there are materials in which the valence's electrons are strongly bound to the lattice ions, and an electric field, although high, can't move them. These materials, which have a very large band gap (typically several eV), take the name of insulators or dielectrics (Fig. 3.1a).

There is also a third category of materials called semiconductors in which the electrons fill up completely the valence band leaving the conduction's band empty. The band gap is very small (few eV) and a small amount of energy (often is sufficient the only thermal energy at room temperature) is sufficient to excite the electrons in the conduction's band. Semiconductors (Fig. 3.1b) are thus able to conduct electric current, current that can be made by both electrons and holes charge carriers. Indeed, when an electron in a semiconductor breaks the bond that bind it to the atom, leaves a gap, a free slot in a lower energy level. A valence's electron from a near atom can then occupy the position, generating a new hole in the place previously occupied. The process is equivalent to the movement of the holes through the material in the opposite direction of electrons.
This model, valid for inorganic materials can be extended to organic materials, with the foresight to replace the E_C and E_V levels with the HOMO and LUMO. We can still call the conduction's band the highest energy one, and valence's band the lowest.

An organic photodiode is usually obtained with a multilayer structure of materials with different conductivity properties.

3.1 Indium tin oxide (ITO)

Indium tin oxide (ITO, or tin-doped indium oxide) is a solid solution of indium(III) oxide (In_2O_3) and tin(IV) oxide (SnO_2), typically 90% In_2O_3, 10% SnO_2 by weight with a reported work function of ~4.7 eV [Parker 1994] [Balasubramanian 1991].
ITO deposition is commonly done by sputtering, but thermal evaporation, spray-coating, pulsed magnetron sputtering and printing techniques are also used [Rauch PhD]. Because of its good transparency in the visible part of the spectrum, the possibility to deposit the material as a thin film with excellent substrate adherence, the high conductivity and efficiency as a hole injector into organic materials, ITO is widely used as electrode in OLEDs, organic solar cells and photodetectors. However ITO has

normally a spiked morphology that can result in non-uniform current flow though the device and premature aging of the device. It is therefore usual to coat the ITO with a layer of a conducting polymer such as poly(3,4 ethylene-dioxythiphene): polystryrene sulfonate (PEDOT:PSS) that acts as an ameliorating layer for the ITO, resulting in substantially improved operating lifetimes of the device. Furthermore, ITO is becoming increasingly expensive due to the limited availability of the element indium [Xu 2009]. In respond to these technical problems, an extensive search is being carried out for alternative materials which are environmentally friendly and stable, with high conductivity and good transparency as well as the ability to be processed in solution. PEDOT:PSS has received increasing attention as possible transparent and conductive material [Xu 2009].

Commercially available ITO coated substrates with ~120 nm film thickness, resistivity of ~10 Ω/□ and transmission of ~90 % in the visible and NIR range are used in this work.

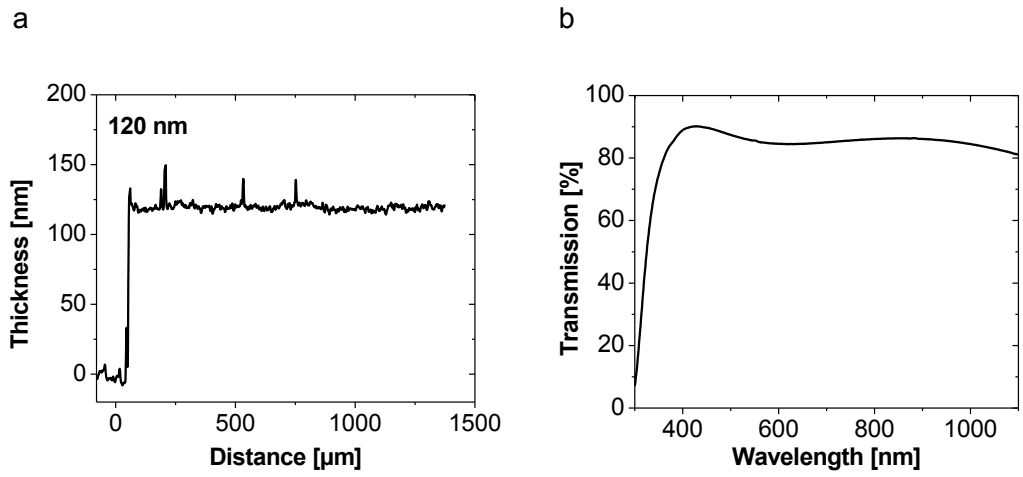

Figure 3.2: a) Profile measurements performed with a profilometer of the ITO layer. The film is ~120 nm thick and some spikes can be seen. b) Transmission measurement of the ITO layer. A transmission of ~90 % in the visible and NIR range is observed. Absorption for short wavelengths < 400 nm is due to the glass substrate.

3.2 Poly(3,4-ethylenedioxythiophene) poly(styrenesulfonate) (PEDOT:PSS)

Poly(3,4-ethylenedioxythiophene) poly(styrenesulfonate) or PEDOT:PSS is a polymer mixture of two ionomers. The poly(3,4-ethylenedioxythiophene), or PEDOT, is insoluble in many common solvents and unstable in its neutral state, as it oxidizes rapidly in air. To improve its processability, a polyelectrolyte solution (PSS) is normally added, resulting in an aqueous dispersion of PEDOT:PSS, where PEDOT is its oxidized state [Nardes 2007]. The resulting PEDOT:PSS is not truly water-soluble but forms a dispersion in water which is stable and processable [Nagarajan 2008].

PEDOT:PSS (wok function ~5.2 eV) [Chu 2006] [Kim 2007] [Li 2008] is widely used as a hole transport layer or electrode in organic electronic devices because of its good film forming properties and the high visible light transmittance. With this material, thin, highly transparent and conductive surface coatings can be prepared by spin-coating, dip-coating or spray-coating on a large variety of surfaces. After drying, the PEDOT:PSS film is uniform, highly conducting, transparent, mechanically durable, insoluble in most common solvent and exhibits conductivities between 10^{-3} and 10 S cm^{-1} [Nagarajan 2008] [Roman 1998] [Zhou 2007] [Admassie 2006].

The use of PEDOT:PSS invites numerous problems. It is know for example the PEDOT:PSS nature to absorbs water from the environment, weakening the layer. The water easily diffuses through the layer and breaks the hydrogen bonds formed between PEDOT:PSS grains resulting in an accelerated decohesion rate. In addition the low electron blocking capability of the material and its acidity that cause corrosion of the processing equipment and dissolution of the ITO layer of the glass substrate contribute to significant reduce the device performance.

Aqueous dispersions of PEDOT:PSS are commercialized by H. C. Starck under the trade mark of Baytron P.

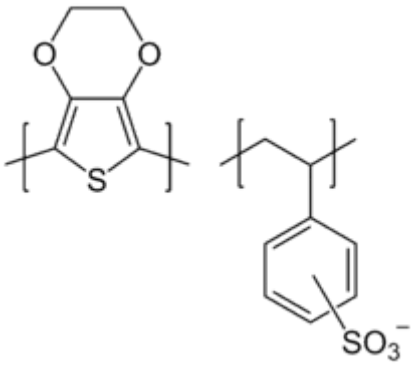

Figure 3.3: PEDOT:PSS chemistry formula.

The PEDOT used in this thesis is the Clevios HIL 3.3N from H.C. Starck with high resistivity of ~20600 Ω cm.

3.3 Self-assembled monolayer (SAM)

A self-assembled monolayer (SAM) is an organized layer of molecules with two terminals, a “tail” with a functional group at the end and a “head group” that shows a specific, reversible affinity for a substrate. In this work n-Octadecylphosphonic acid ($C_{18}H_{39}O_3P$) has been used.

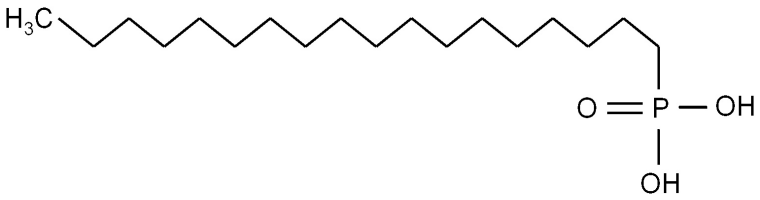

Figure 3.4: n-Octadecylphosphonic acid chemistry formula.

The SAM layer is formed by immersing the ITO substrate in a solution of n-Octadecylphosphonic acid in isopropanol (1% wt.) until a contact angle > 110 ° is measured.

Due to the SAM thin film of a few nm, profilometer can't be used to measure the layer thickness and presence of the material on the ITO surface is checked by contact angle measurements.

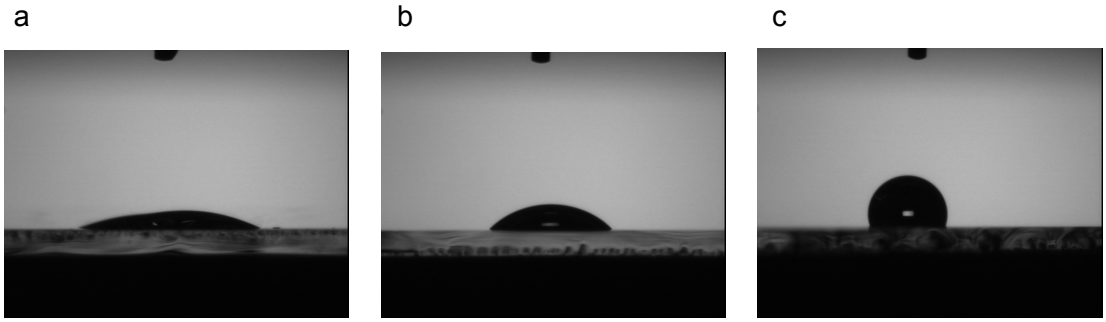

Figure 3.5: Water drop deposited on a) glass. b) ITO. c) SAM.

As an example in Fig. 3.5 water contact angle measurements on different surfaces are presented. A water drop generates a contact angle of ~24° on a glass substrate, ~44° on an ITO layer and ~110° onto a SAM layer.

3.4 Poly(3-hexyl-thiophene) (P3HT)

Poly(3-hexylthiophen-2,5-diyl), also Poly(3-hexylthiophen) or P3HT, chemical formula $C_{10}H_{14}S$ (Fig. 3.6), is a well studied hole transporting material showing a good solubility in many solvents such as chloroform, chlorobenzene, dichlorobenzene trichlorobenzene, toluene, and xylene at ambient conditions. Reported P3HT hole mobilities at room temperature are in the range of 10^{-5}-10^{-2} cm^2 $V^{-1}s^{-1}$ with neglectable electron mobility values [Nakamura 2005] [von Hauff 2006]. It is used prevalently as an electron donor in combination to acceptor materials such as C_{60} or PCBM. The polymer shows an absorption peak for visible wavelengths corresponding to the π-π* absorption band of the molecule. The P3HT can be used either as light absorber or as IL.

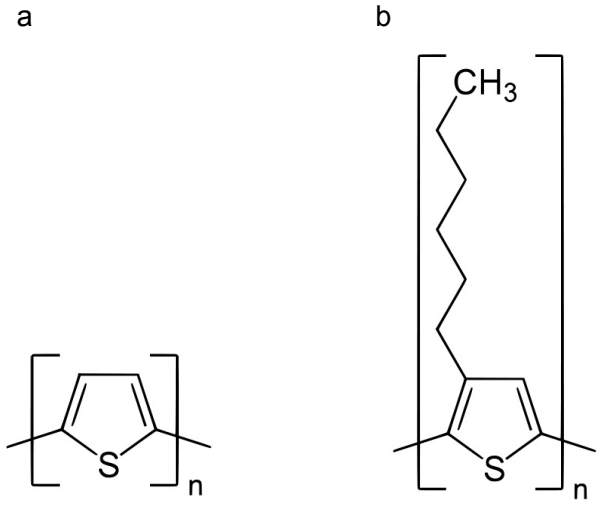

Figure 3.6: a) Thiophene monomer and b) poly(3-hexylthiophene) (P3HT) monomer.

Reported HOMO and LUMO levels are at ~3.2 eV and ~5.1 eV respectively resulting in a bandgap of ~1.9 eV [sigmaaldrich.com] [Kim 2007] [Li 2008] [Thompson 2008]. However, the energy levels depend on several properties, such as the film crystallinity [Savenije 2006].

In this work has been used commercially available P3HT from Rieke with molecular weight (MW) of ~41000 g mol^{-1} and regioregularity of ~93 %.

3.5 Poly[2,6-(4,4-bis-(2-ethylhexyl)-4H-cyclopenta[2,1-b;3,4-b']dithiophene)-alt-4,7-(2,1,3-benzothiadiazole)] (PCPDTBT)

Poly[2,6-(4,4-bis-(2-ethylhexyl)-4H-cyclopenta[2,1-b;3,4-b']dithiophene)-alt-4,7-(2,1,3-benzothiadiazole)] (PCPDTBT) is a low bandgap material with broad spectral absorption from the ultraviolet to ~900 nm wavelength. The material is soluble in many organic solvents as xylene, toluene and chlorobenzene. The absorption peak from a pristine PCPDTBT film is ~775 nm and shows a bathochromic shift when the polymer is in solution or after an annealing step [Hwang 2007]. Charge carrier transport in this material is dominated by holes with mobilities in the range of 10^{-3} $cm^2(Vs)^{-1}$ to 10^{-2} $cm^2(Vs)^{-1}$ with a very weak contribution by electrons with a mobility of 10^{-5} $cm^2(Vs)^{-1}$ [Morana 2008].

The PCPDTBT band gap is estimated to be ~1.4 eV [Hwang 2007] [Dennler 2009] [Zoombelt 2009] with reported energy levels of ~3.5 eV for the LUMO and ~4.9 eV for the HOMO [Kim 2007] [Muhlbacher 2006] [Soci 2007] [Morana 2008].

3.6 [6,6]-phenyl-C61-butyric-methyl-ester (PCBM)

A common used fullerene in photovoltaic applications is the C_{60}, a molecule consisting of 60 carbon atoms, arranged as 12 pentagons and 20 hexagons.

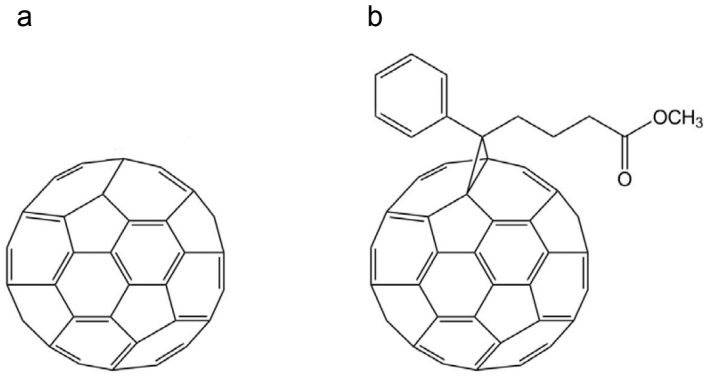

Figure 3.7: a) Buckminister-Fullerene C_{60} and b) PCBM

In this material the 60 electrons from the pz orbitals give rise to a delocalized π system similar to that in conjugated molecules and polymers. With an optical gap in the range of 1.5 to 1.8 eV is a poor light absorbed. However, what makes C_{60} particularly interesting for OPV applications is its excellent performance as an electron acceptor (which derives from its deep LUMO level at ~4.4 eV) [Rogero 2002], and its high electron mobility of 2.0 to 4.9 cm²/(Vs) [Itaka 2006]. In contrast to many organic materials, electron transport dominates the conduction process in C_{60}. C_{60} can be deposited only by vacuum sublimation.

To improve solubility the C_{60} has been functionalized with a methyl-ester group, resulting in a new molucele, [6,6]-phenyl-C61-butyric acid methyl ester (PCBM) soluble in many solvents. This allows for solution processable donor/acceptor mixes. Most common used PCBM solvents are toluene, xylene, chlorobenzene, chloroform and o-dichlorobenzene. Reported PCBM HOMO and LUMO levels are at ~3.7 eV and ~6.1

eV respectively resulting in a bandgap of ~2.4 eV [sigmaaldrich.com] [Yoo 2011] [Mihailetchi 2003] [Li 2008] [Cha 2010] [Meijer 2003].

3.7 Cathode materials

An organic photodiode is usually fabricated with a low work function material as cathode to generate the built-in potential needs to extract the photogenerated charge carriers. The most commonly used cathode material in this thesis is Aluminum (Al) with a reported work function of ~4.3 eV [Michaelson 1977]. Others cathode materials have been also tested like Calcium (Ca), Silver (Ag), Gold (Au), Zinc oxide (ZnO), Copper (Cu) with reported work functions from literature of Ca (~2.8 eV) [Chu 2006], Ag (~4.2 eV) [Tedde PhD], Au (~5.0 eV) [Chu 2006] [Michaelson 1977], ZnO (~4.45 eV) [Bulliard 2010] and Cu (~4.65 eV) [Anderson 1949].

The tested materials have a work function lower than the ITO anode (reported work function of ~4.7 eV [Parker 1994] [Balasubramanian 1991]) with the exception of the Au.

Processing techniques

Solution processed OPDs are usually fabricated by doctor-blading, spin-coating or spray-coating techniques to generate a thin semiconductor layer.

3.8 Doctor-blading

Doctor-blading is an easy way to deposit a uniform thin film on a flat substrate. A horizontal blade moves with a constant distance over the substrate spreading the material solution.

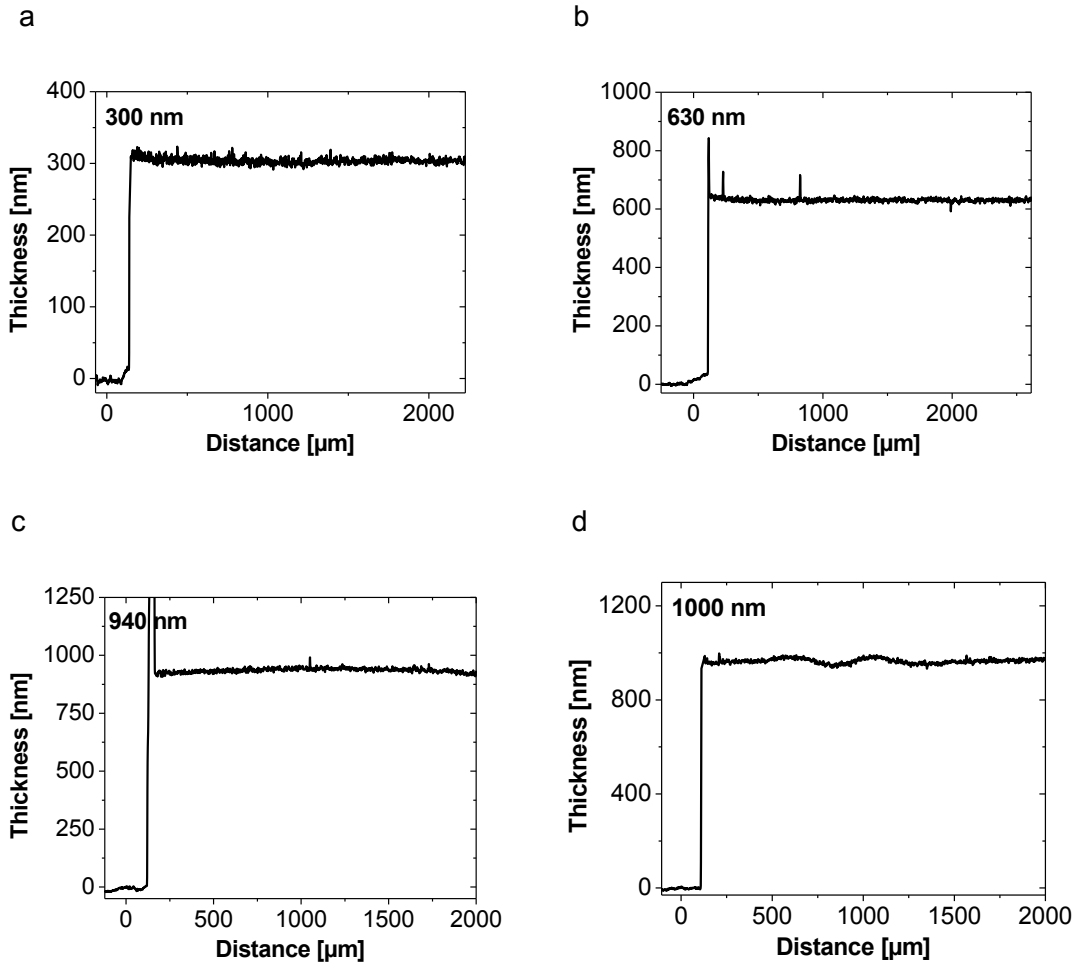

Figure 3.8: Profilometer measurement of a doctor-bladed BHJ (P3HT:PCBM 1:0.75 wt. in xylene) layer with mean thickness of a) ~300 nm. b) ~630 nm. c) ~940 nm. d) ~1000 nm.

Varying blade speed and blade/substrate distance can control film thickness. In general, doctor-blading can deal with larger areas and thick films.

In this thesis doctor-blading technique has been used to deposit the semiconductor onto the interlayer.

In Fig. 3.8 profilometer measurement of BHJ layers fabricated by doctor-blading are shown. The BHJ solution (P3HT:PCBM 1:0.75 wt. in xylene) has been doctor-bladed on a glass substrate 1, 2, 3 and 4 times resulting in a layer of ~300 nm, ~630 nm, ~940 nm and ~1000 nm respectively.

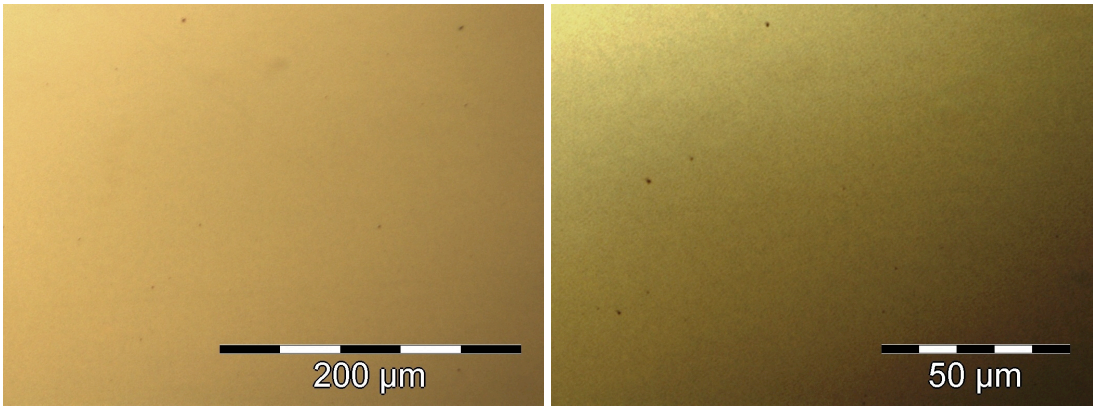

Figure 3.9: Optical microscopic pictures of a doctor-bladed BHJ (P3HT:PCBM 1:0.75 wt.) layer with ~300 nm thickness at different magnifications.

3.9 Spin-coating

Spin-coating is a common method used to apply uniform thin films on a flat substrate. A substrate is placed on a chuck and fixed to it normally by vacuum. An excess amount of a solution is placed on the substrate, which is then rotated at high speed in order to spread the fluid by centrifugal force. The acceleration, spin velocity and spin time set the layer characteristics.

For comparison with BHJ doctor-bladed films, in Fig. 3.10 profilometer measurement of BHJ layers fabricated by spin-coating are shown. The BHJ solution (P3HT:PCBM 1:0.75 wt.) has been spin-coated on a glass substrate at 300 rpm, 400 rpm, 600 rpm and 1000 rpm resulting in a layer of ~300 nm, ~230 nm, ~160 nm and ~110 nm respectively.

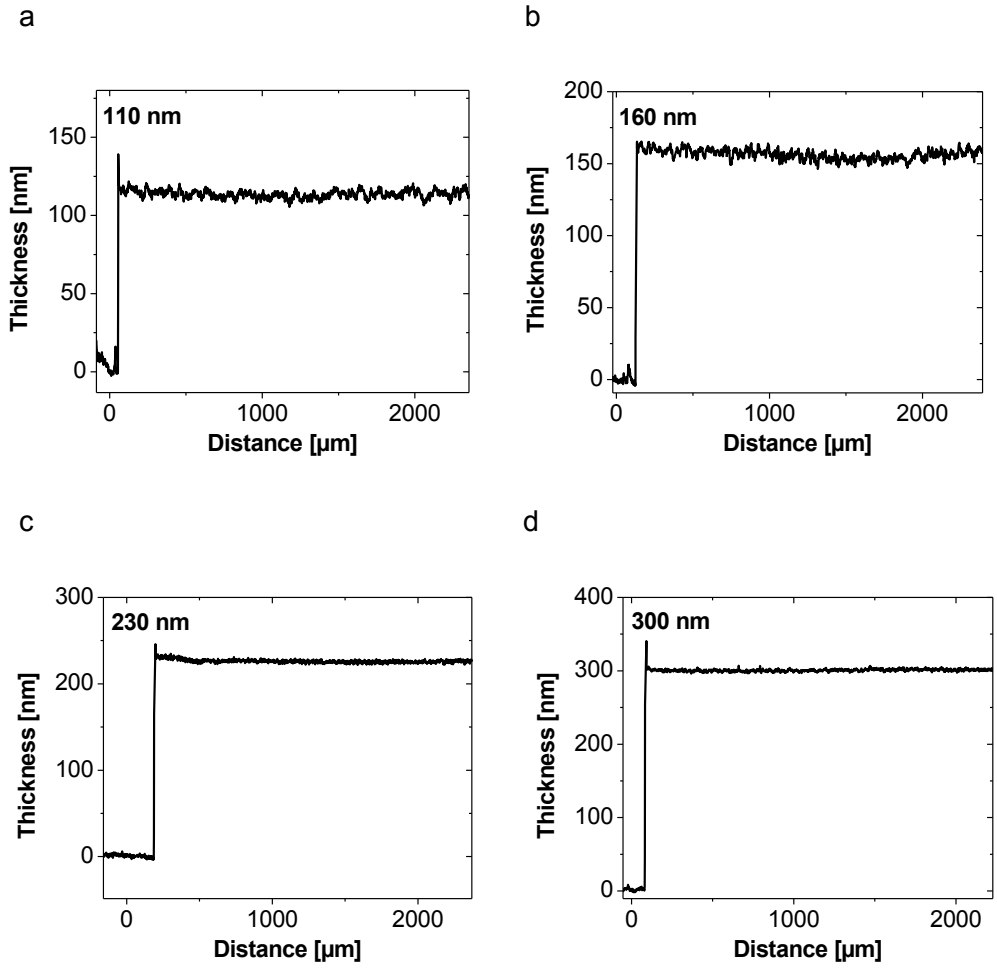

Figure 3.10: Profilometer measurement of a spin-coated BHJ (P3HT:PCBM 1:0.75 wt. in xylene) layer with mean thickness of a) ~110 nm. b) ~160 nm. c) ~230 nm. d) ~300 nm.

In this work spin-coating have been used to deposit the PEDOT:PSS onto the ITO. With ~2000 rpm rotation speed a PEDOT:PSS layer of ~150 nm is usually obtained.

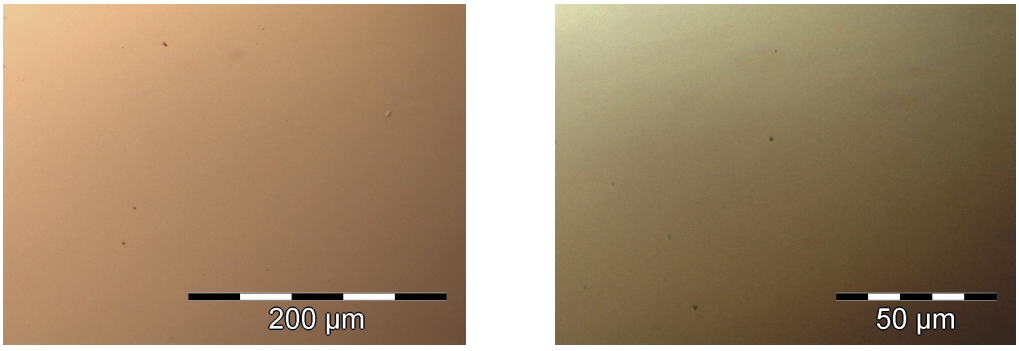

Figure 3.11: Optical microscopic pictures of a spin-coated BHJ (P3HT:PCBM 1:0.75 wt.) layer with ~230 nm thickness at different magnifications.

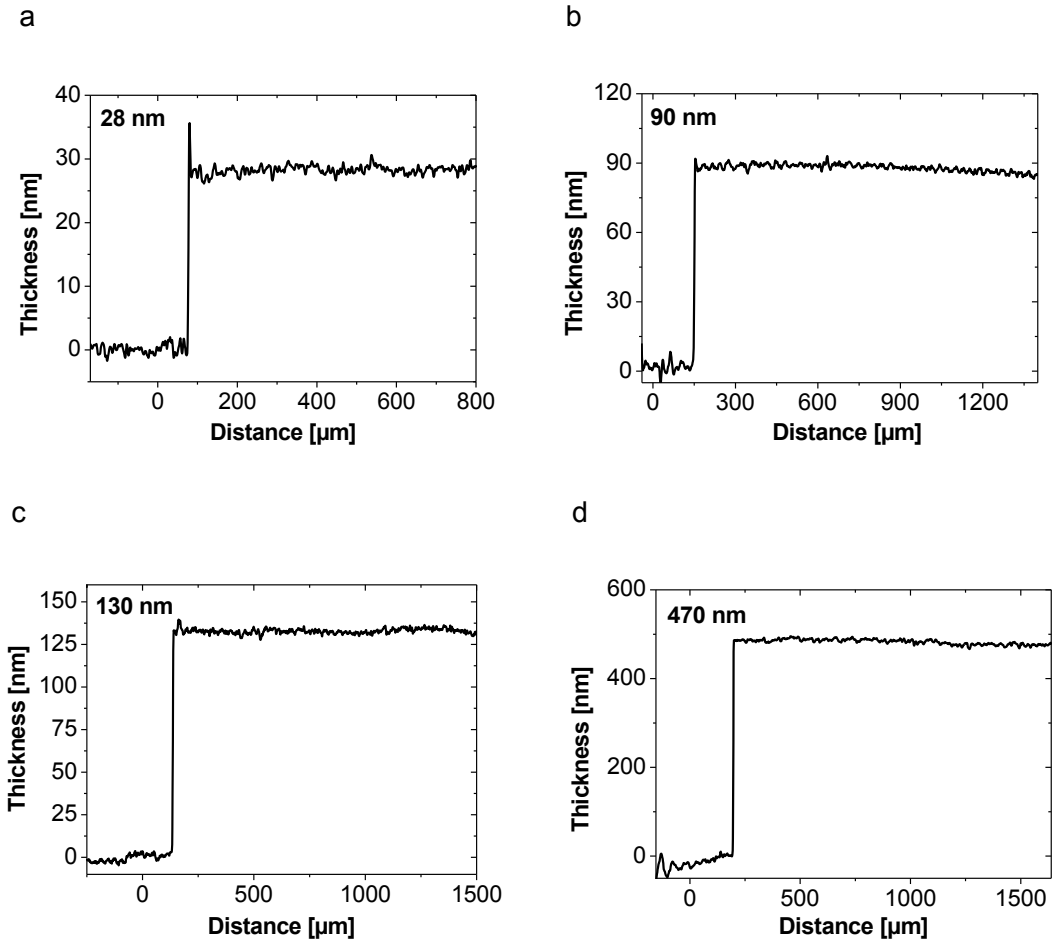

Figure 3.12: Profilometer measurement of a spin-coated PEDOT:PSS HIL 3.3N layer with mean thickness of a) ~28 nm. b) ~90 nm. c) ~130 nm. d) ~470 nm.

3.10 Spray-coating

Spray-coating is a cheap and fast deposition technique capable to deposit a material solution on, ideally, every substrate. Here, an air-brush gun, usually PC-controlled, sprays the material on a substrate. Spray-coating is largely used in industry for spraying, for example, a protective paint layer on the car metal surface. Advantages of this technique are the possibility to deposit the material almost on every substrate (not necessary only flat) on large areas and the possibility to be applied multiple times in order to increase the total layer thickness. Contrary to other deposition techniques such as doctor-blading or spin-coating, spray-coating makes possible to deposit

several layers of different materials one on top of the other with low intermix between the different layers also if the same solvent is used. Carefully setting the air-brush gun, it is possible to generate small air-droplets that dry before reach the substrate. If this condition is verified, the new material is not able to dissolve the previous layer, also if the same solvent is used. In Fig. 3.13 a spray-coated BHJ layer (P3HT:PCBM 1:0.75 wt. in xylene) with ~500 nm thickness is shown with aerosol particle size < 10 µm.

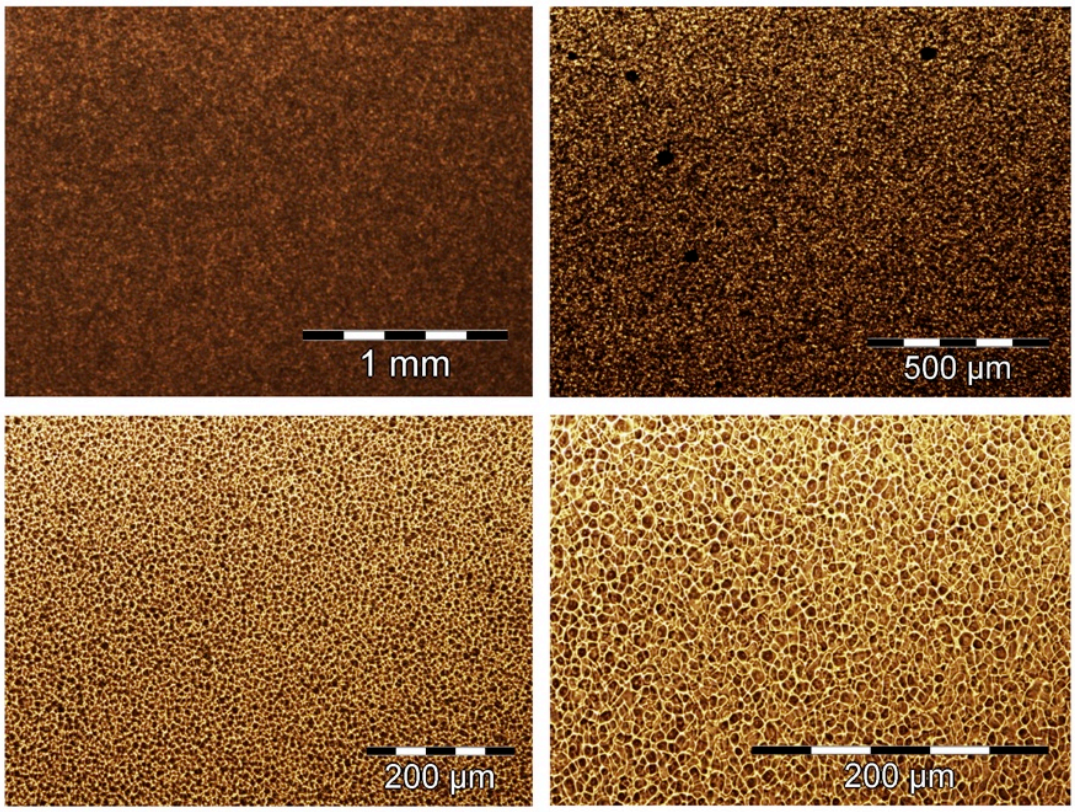

Figure 3.13: Optical microscopic pictures of spray-coated BHJ with ~500 nm thickness at different magnifications (aerosol particle size < 10 µm).

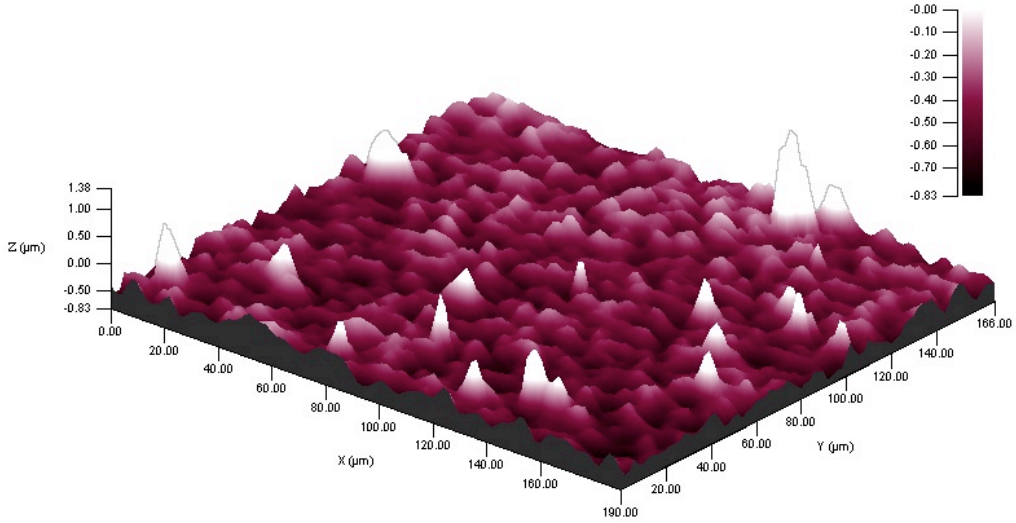

Figure 3.14: Exemplary surface analysis with a profilometer (3D plot) of a spray-coated BHJ layer (P3HT:PCBM 1:0.75 wt.) with mean thickness of ~500 nm.

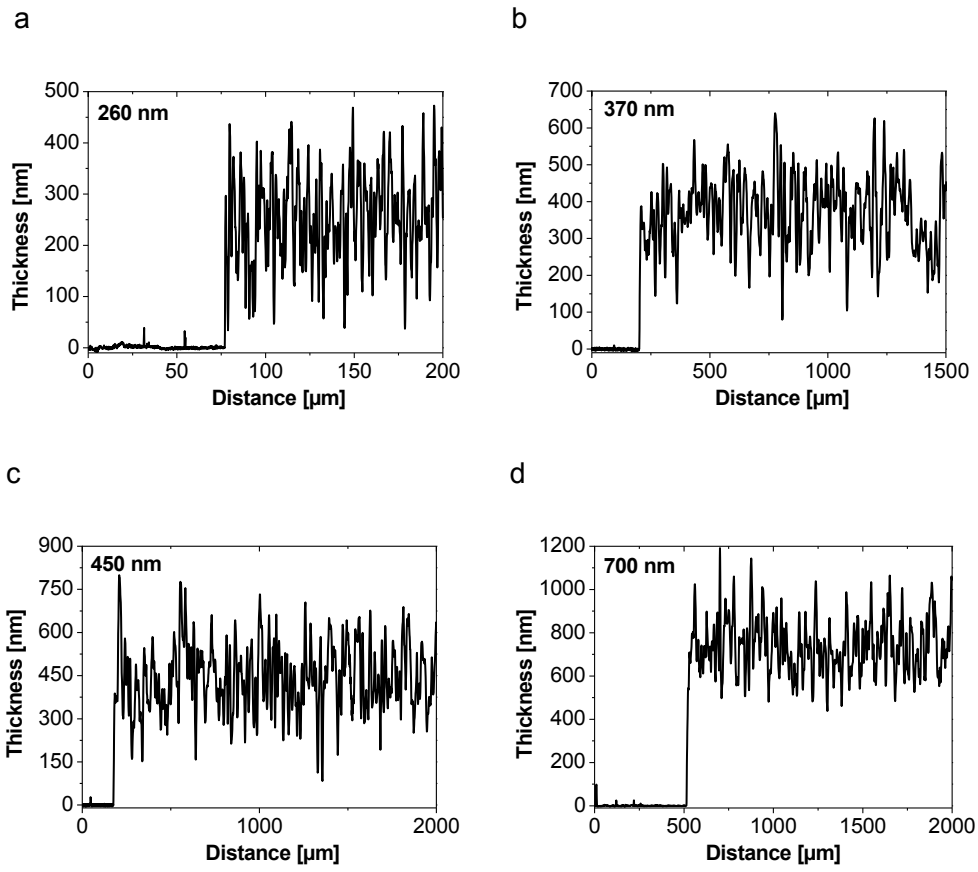

Figure 3.15: Profilometer measurement of a spray-coated BHJ (P3HT:PCBM 1:0.75 wt.) layer with mean thickness of a) ~260 nm. b) ~370 nm. c) ~450 nm. d) ~700 nm.

Exploiting this propriety, it has been possible to fabricate devices were both interlayer and semiconductor were spray-coated from the same solvent with low intermix.

In Fig. 3.14 a 3D exemplary surface analysis plot of a spray-coated BHJ (P3HT:PCBM 1:0.75 wt. in xylene) and in Fig. 3.15 a profilometer measurement of a spray-coated BHJ (P3HT:PCBM 1:0.75 wt. in xylene) layer with mean thickness from ~260 nm to ~700 nm are presented. Despite the high roughness of the layer as result of the spray-coating process, a continuous close layer can always been identified. For the ~700 nm thick film a continuous close layer thickness of ~450 nm can be seen. It prevent short between anode and cathode. The best compromise between OPD dark current and EQE value is achieved with mean BHJ thickness of ~500 nm to ~700 nm. Thin layers result in a device with high dark current due to low resistive paths between anode and cathode while thick layers result in a device with reduced EQE due to charge carrier's recombination.

3.11 Thermal evaporation

The thermal evaporation process is usually employed to deposition the cathode electrode. The thermal evaporator used in this work is located in a glovebox. In a chamber with a vacuum level of ~10^{-6} to 10^{-7} mbar a Tungsten filament is heated causing the contained material first to evaporate and than to condense on the substrate. Varying the heat source can control film thickness.

Others common material deposition techniques include drop-casting, inkjet-printing, transfer-printing, roll-to-roll, sputtering and screen-printing.

OPD fabrication

In this paragraph the protocol to fabricate a standard OPD is presented.

OPDs are fabricated on a 5x5 cm² structured ITO coated glass. In order to lower the dark currents ITO electrode rims are passivated by ~1 µm SU-8 transparent photoresist and a photoactive area of 1 cm^2 of the anode defined by photolithography.

Photoresist hard baking is performed at 200 °C for 15 min on a hotplate. If not otherwise wrote, all OPDs here presented are fabricated using the SU-8 passivating layer.

After cleaning the substrates in acetone, isopropanol and deionized water RIE plasma is applied to activate the ITO surface before the deposition of the electron blocking layer (IL).

Different materials have been used as IL in this work. PEDOT:PSS is usually spin-coated onto the ITO in layer thickness of ~150 nm and baked in a vacuum oven at 200 °C for 15 min. P3HT IL is spray-coated onto the ITO usually from a xylene solution (1 % wt.) resulting in a film layer with mean thickness ranging from 70 nm to 100 nm. The SAM thin layer is formed by immersing the ITO substrate in a solution of n-Octadecylphosphonic acid in isopropanol (1% wt.) until a contact angle > 110 ° is measured. With the only exclusion of the SAM layer, thicknesses are measured with a profilometer instrument.

After deposition of the ILs the semiconductor (BHJ) is deposited onto the IL normally by doctor-blade or spray-coating technique in ambient condition. The BHJ is usually a blend of P3HT:PCBM (1:0.75 wt.) or PCPDTBT:PCBM (1:2.5 wt.). According to surface profilometry measurements, the doctor-bladed films have a mean thickness ranging from ~200 nm to ~250 nm for all the BHJs while a single spray step result is a mean film ~500 nm.

After BHJ deposition all samples are annealed at 140 °C for 5 min in inert condition before thermal evaporation of 4 nm/100 nm of Ca/Ag or 100 nm of Al as top electrode through a shadow mask. Overlap between anode and cathode define an active area of usually 1 cm^2.

Diodes are encapsulated with solvent-free epoxy glue and a 100 μm thick transparent glass slide. OPDs are finally annealed at 80 °C for 30 min on a hotplate for glue curing.

Characterization methods

3.12 Current-Voltage (I-V) measurements

I-V characteristic of the diodes are recorded using a Keithley 6487 picoammeter in an electrically and optically shielded box. Photocurrents are measured with illumination through the transparent conductive electrode. For illumination of the photodiodes, a green light-emitting diode with a wavelength of 532 nm wavelength and irradiation intensity of 780 μW cm^{-2} is used. For NIR illumination of the photodiodes, a white beam of an AM 1.5 Oriel solar simulator with a power density of ~100 mW cm^{-2} and a GaAs filter with cut-on wavelength at 870 nm is used. Full description of the setup is reported in [Tedde PhD] [Rauch PhD].

3.13 External quantum efficiency (EQE) measurements

EQE spectra is recorded with a lock-in technique using a chopping frequency of 170 Hz and an Oriel Cornerstone 130 1/8 m monocromator. Si photodiode is used as a reference diode for calibration. Full description of the setup is reported in [Tedde PhD] [Rauch PhD].

3.14 Dynamic measurements

Dynamic measurements are made in an electrically and optically shielded box with a transimpedance amplifier (FEMTO DHPCA-100) connected to a digital oscilloscope (LeCroy Wavesurfer 424). A low pass filter from SRS (SIM965) is inserted to reduce the high frequency noise. Through the transparent OPD ITO electrode a green-pulsed light is applied by a high power LED controlled by a signal waveform generator (TGA 1242) to create a square wave with frequencies ranging from 10 mHz to 1 MHz. The incident light intensity is decreased from mW cm^{-2} to nW cm^{-2} with neutral densities filters ranging from 0.1 to 4.

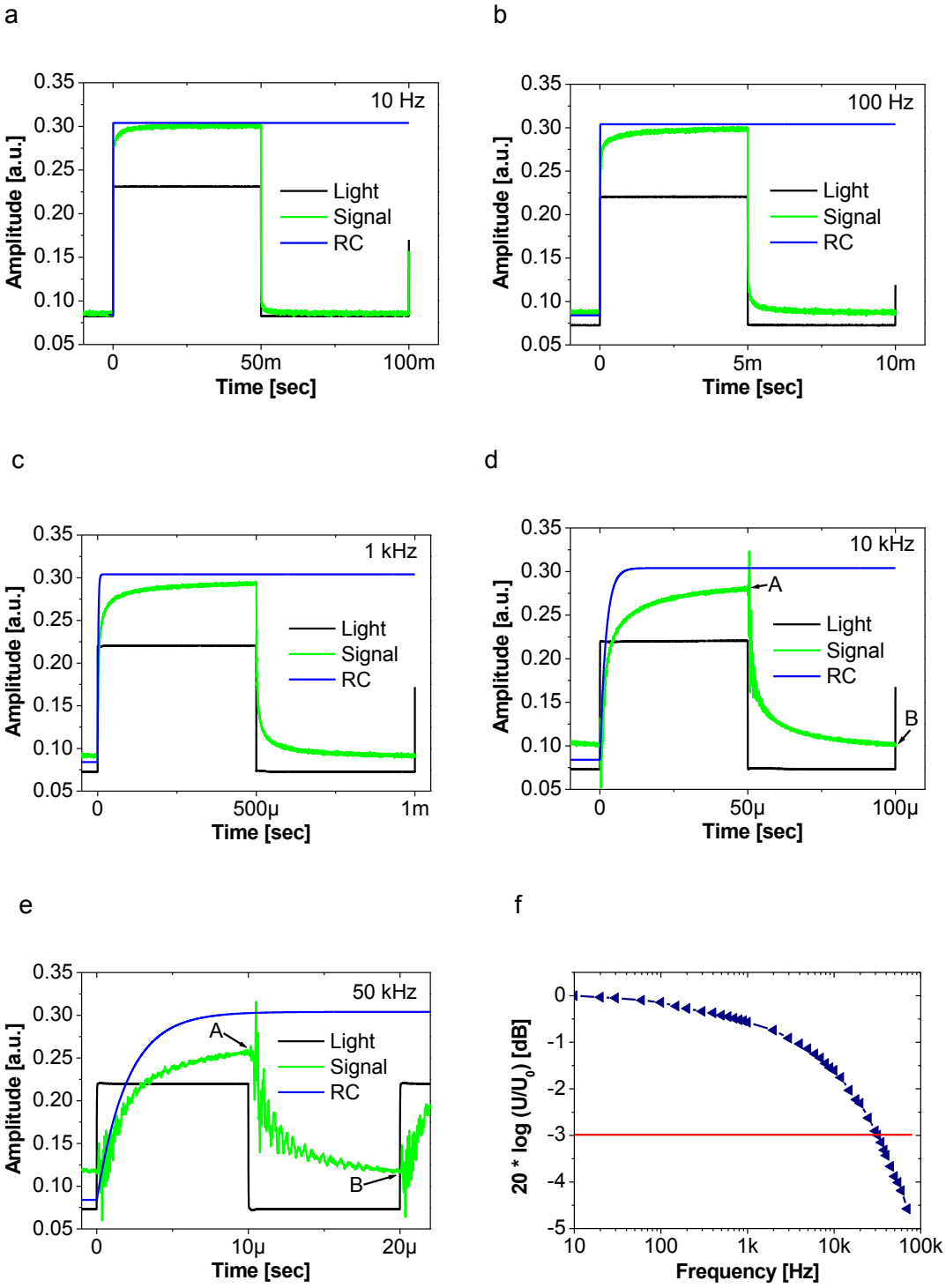

Figure 3.16: Transient measurements of an OPD with active area 1 cm² at -5 V reverse bias for a) 10 Hz. b) 100 Hz. c) 1 kHz. d) 10 kHz. e) 50 kHz. f) Amplitude Bode diagram.

Fig. 3.16 shows exemplary OPD signal response to a square shape light pulse (532 nm @ 60 µW/cm², 50 % duty cycle) with illumination frequency of a) 10Hz, b) 100 Hz,

c) 1 kHz, d) 10 kHz and e) 50 kHz. With the help of the digital oscilloscope the amplitude differences between the points were the light pulse change (A minus B in the Fig. 3.16) is derived. The square-shape light frequency is varied and for each frequency the A-B amplitude is measured. The measured difference amplitude (U, Fig. 3.16f) is then normalized for the difference amplitude at the lowest frequency (U_0). From the U/U_0 ratio the amplitude Bode plot is extracted (Fig. 3.16f). Cut-off frequency corresponds to the cross point between the amplitude Bode plot and the -3dB. For low light intensity a low pass filter (SIM965 Analog filter from SRS, Butterworth filter with 12 dB/oct. slope) is used. Filter cut-off frequency, which is varied according to the measurement range, is always kept at least one decade higher than the light pulse frequency to ensure no amplitude cut-off due to the filter characteristics. The transimpedance amplifier is set with gain of 10^4 V/A for high and medium light intensities. For low light intensities the amplification gain is increased (up to 10^6 V/A for 20 nW/cm^2 low light intensities).

Since OPD photocurrent rises and falls exponentially, a single order model (one pole) can be implemented to model the system. The blue line in Fig. 3.16 (marked RC) represents the ideal photodiode output with the rise time as result of the diode resistance R and capacitance C only. This line represents the faster current rise. The real OPD is usually slower than the ideal OPD, as can be seen in Fig. 3.16, due to extra loss contributions as low charge carrier mobility, charge trap phenomena, series resistance and capacitance of wire connections.

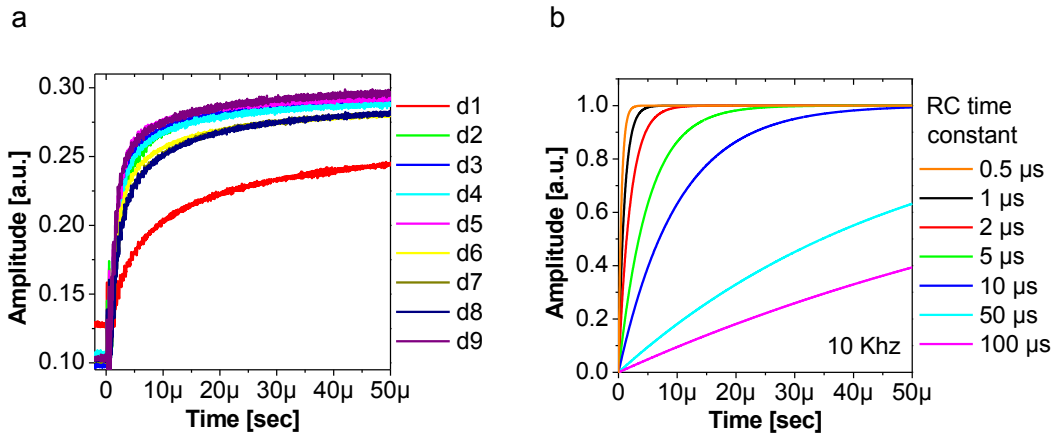

Figure 3.17 a) Dynamic response measured on nine 1 cm^2 OPDs. b) Ideal first order model OPD response by varying the RC time constant.

Finally, in Fig. 3.17 exemplary dynamic measurements of 1 cm^2 OPDs to a 50 µs light pulse are presented with different rise times as function of the implemented stacks. On the right ideal photocurrent rise for a first order system with decreasing the RC time constant is shown.

3.15 X-ray measurements

X-rays photons with energy of 70 keV are generated with a commercial X-ray source (generator Polydoros A100). Schematic and specs of the generator are presented in Fig. 3.18a.

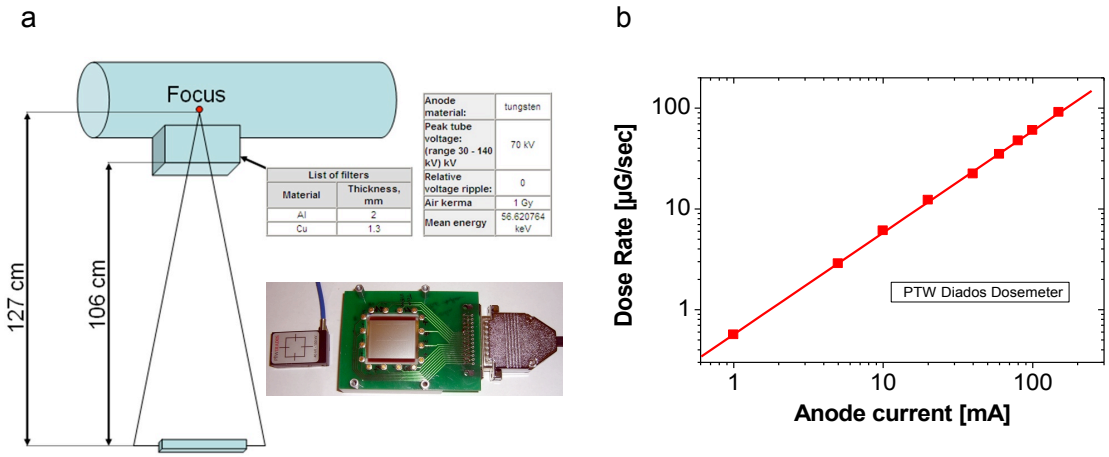

Figure 3.18: X-ray source generator schematic. Inset shows the OPD mounted in the holder next to a calibrated X-ray dosimeter. b) X-ray dose rate vs. tube anode current.

Distance between OPD and X-ray source focus is ~130 cm. X-ray doses are measured with a calibrated dosimeter and to reduce X-ray doses up to µGy range Cu and Al filters are used.

The Gray (Gy) is the common used unit measure of the absorbed dose and is defined as the absorption of one joule of energy by one kilogram of matter.

$$1\ Gy = 1\ \frac{J}{kg} \tag{3.1}$$

The X-Ray tube is controlled by a LabView program to generate X-ray pulses at 70 kV with different dose rates by varying the anode current from 150 mA to 1 mA. A linear correlation between anode current and dose rate is observed for several decades (Fig. 3.18b). Setup is limited to minimum 70 kV 1 mA. For lower dose extra shields are needed.

Reducing distance between sample and X-ray generator focus correspond to a X-ray dose increase (X-ray attenuate whit $1/r^2$ law, with r radiation propagation length).

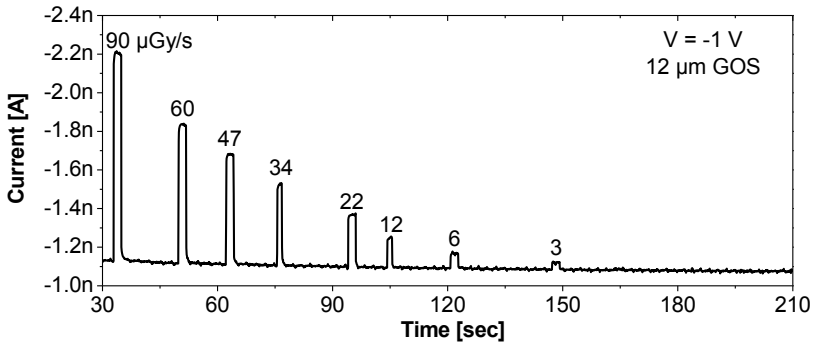

Figure 3.19: Exemplary OPD response to X-ray pulses at 70 kV with dose rates from 90 µGy/s to 3 µGy/s of a 1 cm^2 OPD with stack ITO/P3HT/BHJ/Al reverse biased at -1 V and coupled with 12 µm sedimented GOS scintillator.

For sensitivity X-ray measurements, OPD is DC reverse biased and current vs. time acquired by a Keithley SMU. X-ray pulses with different dose rates are applied to the OPD and photocurrent (signal under X-ray illumination minus dark signal) recorded, Fig. 3.19.

4. Analysis of OPD performances

In this chapter experimental results are presented. In particular here is discussed how each layer of the organic photodiode (OPD) stack such as the interlayer (IL), the solvent, the semiconductor or cathode material influences the diode characteristics.

4.1 IVs with varying light intensity

The OPD photocurrent (eq. 2.3) depends on many parameters such as the incident light intensity and the wavelength. In general, for a constant wavelength, higher is the light intensity higher is the measured photocurrent because more charge carriers are generated in the semiconductor layer. As an example Fig. 4.1a shows IV measurements performed on a spray-coated 1 cm^2 OPD in dark and with green light illumination at 532 nm wavelength with varying the incident light intensity from ~780 μW cm^{-2} to ~23 nW cm^{-2}. The analyzed OPD stack is ITO/PEDOT:PSS/BHJ/Al. The interlayer PEDOT:PSS is spin-coated onto the ITO layer at ~2000 rpm resulting in a layer thickness of ~150 nm while the semiconductor is a P3HT:PCBM (1:0.75 wt.) blend in xylene spray-coated onto the PEDOT:PSS layer (mean active layer thickness of ~470 nm). 100 nm of Al are then thermally evaporated onto the semiconductor layer and the device is sealed with epoxy glue and a thin glass slide. The green light is applied to the OPD through the transparent ITO electrode.

As can be seen in Fig. 4.1a the photocurrent for negative biases decreases reducing the light intensity while for positive biases no variation in the IV can be see, indicating that the serial resistance of the diode at +2 V is not influenced by the light-doping of the semiconductor. Photocurrent shows a saturation plateau at negative biases for all light intensities. With reducing the light intensity a left-shift of the V_{OC} is also observed. For an OPD with active area of 1 cm^2 and dark current densities of ~10^{-5} mA cm^2 at -5 V reverse bias the minimum detectable light intensity is a few nW cm^2. To detect lower light intensity, dark current densities < 10^{-5} mA cm^2 at -5 V reverse bias are needed.

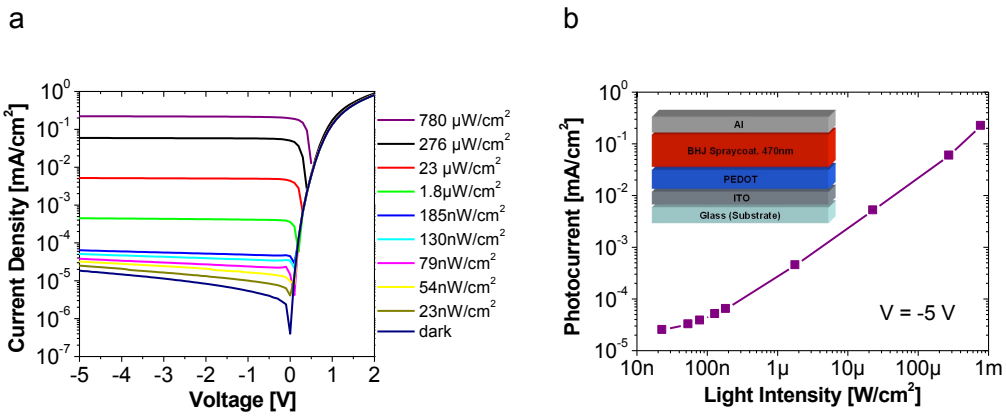

Figure 4.1. a) IVs of a 1 cm^2 OPD with varying light illumination from ~780 µW/cm^2 to ~23 nw/cm^2. The green light (λ = 530 nm) is applied to the OPD through the transparent ITO electrode. b) Photocurrent vs. light illumination measured at -5 V reverse bias. Inset shows the OPD layers stack.

Despite a linear correlation between photocurrent and incident light intensity is expected, an almost exponential correlation is observed, Fig. 4.1b.

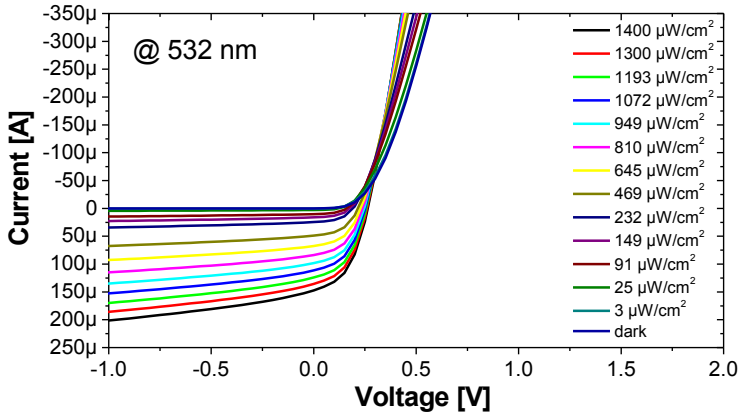

Figure 4.2. IV in linear scale measured on a 1 cm^2 with varying green light illumination from ~1400 µW cm^{-2} to ~3 µw cm^{-2}.

Finally, in Fig. 4.2 IV measurements between 1 V and -1 V reverse bias in linear scale with 532 nm light wavelength by varying the intensity are shown.

4.2 Interlayer analysis

In many organic optoelectronic devices, including organic light-emitting diodes, photovoltaic cells and photodiodes, a hole injection layer (interlayer, IL) is usually inserted between the transparent anode and the active layer as electron blocker. In this paragraph influence of the IL on the organic photodiode performance is investigated.

In literature several strategies have been reported to improve the hole extraction (and the electron blocking) from the photoactive layer. The most commons include incorporation of several different types of hole extraction layers in the device stack such as conductive polymeric materials, self-assembled molecules and metal oxides, as well as surface treatment of the positive electrodes and the conductive polymeric layers [Park 2010]. The IL at the negative electrode can improve the OPD performance transferring electrons more efficiently and blocking the movement of holes from the active layer to the cathode. Furthermore, although the local vacuum reference energy level is assumed constant at each interface in the organic electronic device, it seems that the use of an IL can results in a device with interface dipoles at the organic/metal and organic/organic interfaces resulting often in a shift of the vacuum level [Park 2010]. It follows that the IL plays an important role in the charge injection/extraction control, since it can set the work function of the electrode. For example seems that the introduction of molecular dipole layers such as self-assembled monolayers (SAMs) at the organic/electrode interfaces can effectively tune the work function of the transparent conducting oxides and metals [Armstrong 2009]. Since most ILs can potentially set the effective work function of the electrode, the charge extraction from the organic photoactive layers to the electrodes can be effectively controlled during fabrication process with the IL [Braun 2009] [Armstrong 2009].
The most common used IL for organic photodetectors and organic solar cells is the PEDOT:PSS with work function from 5.0 to 5.2 eV [Chu 2006] [Kim 2007] [Li 2008]. Since the PEDOT:PSS work function lies between the work function of ITO (~4.8 eV) and the ionization potentials of the donor polymers (~5.2–5.5 eV), the PEDOT:PSS film can facilitate the hole extraction from the photoactive layer. Despite many theories have been formulated to explain the importance of the PEDOT:PSS electron blocking layer to set the OPD behaviour, the real influence of the IL in the OPD characteristic

remains up today unclear. In 2008 Ramuz et al. [Ramuz 2008] reported a comparison between 2 photodiodes, one with PEDOT:PSS IL and one without IL. Experimental measurements show for the device without IL an almost 2 two orders of magnitude lower dark current compared to a device with PEDOT:PSS IL. Experimental results show an extraordinary and unexpected result: omitting the standard PEDOT:PSS layer does not adversely affect the device characteristic that still present a rectification behaviour (Fig. 4.3a). Result indicates that the semiconductor/electrode interface is itself capable to determine the rectification behaviour due to Shottky contact without the extra need of the IL to block one charge carrier. Diode rectification behaviour is even better than with the use of an electron blocking layer.

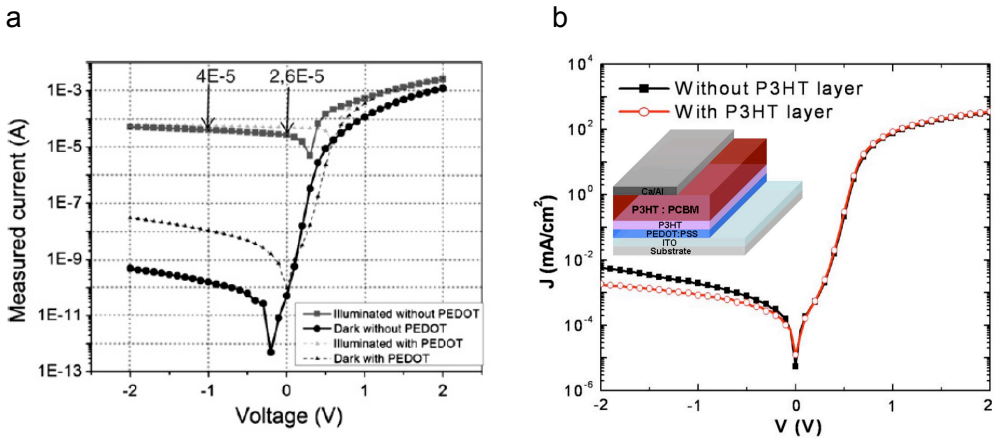

Figure 4.3: a) IV measurements of two OPDs with PEDOT:PSS IL and without IL [Ramuz 2008]. b) IV characteristic of P3HT:PCBM-based device with and without P3HT IL [Liang 2009]

The unfavourable quality and/or the weak stability of the PEDOT:PSS/ITO interface is a possible explanation for the reduction of the dark current when no PEDOT:PSS is used [de Jong 2000].

Others materials has been recently adopted as PEDOT:PSS IL replacement, like for example the P3HT, that chemically similar to the PEDOT molecule, is prevalently a hole conductive material and so a good electron blocking layer candidate. In 2009 Liang et al. [Liang 2009] reported that the insertion of a P3HT layer between the P3HT:PCBM composite and the PEDOT:PSS IL results in a device with lower dark current and higher quantum efficiency compared to a device with only PEDOT:PSS IL (Fig. 4.3b). Experimental result is explained with the assumption that, with the insertion

of the P3HT layer an additional p-n junction is formed at the bottom of the active layer that increases the donor-acceptor interfacial area and then the photoinduced electron transfer energy. For the device fabrication, a P3HT solution in chlorobenzene is spin-coated onto the PEDOT:PSS and, subsequently, a mixed solution of P3HT and PCBM in the same solvent is spin-coated on top of the P3HT layer. When the blend solution is dropped onto the substrate, the pre-coated P3HT film is partially dissolved resulting in a polymer-dominated mixture in the lower regions of the coating solution. To prevent the entire dissolution of the pristine polymer layer during coating author adopted for the BHJ a P3HT with different molecular weight. The multi-spin coating method to fabricate the P3HT/photoactive layers adopted by Liang et al, although very simple, seems to be a non-quantitative coating method because the precoated P3HT film can be dissolved by the co-solvent of the photoactive solution. Very recently Oh et al. [Oh 2011] reported an improvement of the stack with P3HT IL.

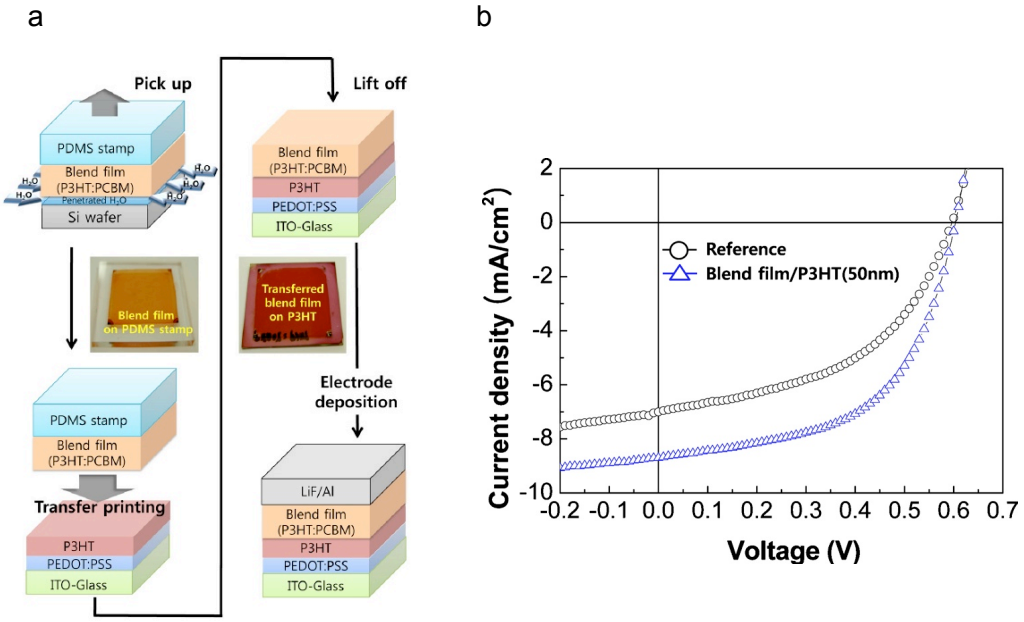

Figure 4.4. a) Schematic diagram of the improved device with P3HT IL fabricated by a transfer printing method [Oh 2011]. b) IV characteristic of the resulting device.

A P3HT solution in chlorobenzene is first spin-coated onto the PEDOT:PSS coated substrate. To prevent the dissolution of the pre-coated P3HT layer by the co-solvent, the BHJ film is deposited onto the P3HT layer by a tricky transfer printing method,

illustrated in Fig. 4.4a. The resulting device shows a higher photocurrent compared to a reference diode without P3HT IL (Fig. 4.4b), explained by the authors by a vertical distribution of the photoactive materials in the blend film by inserting a P3HT layer between the photoactive layer and the PEDOT:PSS. Furthermore seems that the additional P3HT layer contributes to the photocurrent with additional photogenerated carriers. Both effects contributed to the enhancement of photon conversion efficiency [Oh 2011]. Oh assumes also that the inserted P3HT layer induces the diffusion of the PCBM toward the top surface rather than the bottom layer during thermal annealing in the blend film [Oh 2011].

Another possible IL material applies the SAM. The creation of a SAM layer onto the ITO is for example a well-known approach to control the effective work function in organic light-emitting (OLED) diodes by shifting the anode vacuum level [de Boer 2005]. Despite Kim et al. [Kim 2007] reported that by using SAMs with terminal groups of $-NH_2$, $-CH_3$ and $-CF_3$, the hole extraction barrier from the P3HT:PCBM blend to the ITO can be controlled and [Quiles 2008] that a self-assembled monolayer deposited on the substrate surface can control the vertical composition distribution of the BHJ segregating the P3HT towards the bottom, the role played by the SAM IL on the OPD performance remains still unclear.

In this thesis OPDs with PEDOT:PSS, P3HT and SAM as IL are reported. Diodes with P3HT IL here presented are an improvement of the devices by [Oh 2011]. Here, OPDs are fabricated with spray-coating technique that, contrary to the multi-spin technique of [Liang 2009], prevents dissolution of the previous layer also if the same solvent is used.

In order to investigate the IL influence on the OPD performances, four different OPDs with different ILs are fabricated on ITO coated glasses: first a diode with PEDOT:PSS as common IL applied in solar cells and photosensors, second with P3HT IL, third with a SAM IL and last a diode without IL as reference. The diodes are fabricated on a 5x5 cm² structured ITO coated glasses. In order to lower the dark currents ITO electrode rims are passivated by ~1 µm SU-8 transparent photoresist and a photoactive area of 1 cm^2 of the anode defined by photolithography. Photoresist hard baking is performed at 200 °C for 15 min on a hotplate. After cleaning the substrates in acetone,

isopropanol and deionized water RIE plasma is applied to activate the ITO before the deposition of the electron blocking ILs.

PEDOT:PSS HIL 3.3N IL from HC Starck is spin-coated in ambient condition at ~2000 rpm on the ITO in a layer thickness of ~150 nm and than baked in a vacuum oven at 200 °C for 15 min. P3HT IL is spray-coated on the ITO from a solution of 1% wt. in xylene resulting in a film thickness of ~70 nm. SAM IL is formed by immersing the ITO in a 1% wt. octadecylphosphonic acid solution in isopropanol until a contact angle > 110° is measured. Last, a substrate without IL is applied as reference. Due to the SAM thin film of a few nm, profilometer can´t be used to measure the layer thickness and presence of the material on the ITO surface is checked by contact angle measurements. After deposition of the ILs a BHJ layer is spray-coated in ambient conditions from a solution of P3HT and PCBM in xylene (P3HT:PCBM 1:0.75 wt.).

According to surface profilometry measurements, the BHJ mean thickness is ~470 nm for the sample with PEDOT:PSS IL, ~700 nm for the SAM IL, ~550 nm for the P3HT IL and ~700 nm for the OPD without IL.

BHJ thickness is selected in such way that equal internal electric fields of all OPDs and thus comparable electrical characteristics are ensured. In addition, with BHJ thicknesses > 400 nm diodes have comparable internal quantum efficiencies. The spray-coating process allows fabricating layers with a batch to batch thickness variation of ~10 %. The mean layer thicknesses for the reported OPDs (IL + BHJ) are: PEDOT:PSS IL (150 nm PEDOT:PSS + 470 nm BHJ = 620 nm); P3HT IL (70 nm P3HT + 550 nm BHJ = 620 nm); SAM IL (~2 nm SAM + 700 nm BHJ = ~700 nm); No IL (0 nm IL + 700 nm BHJ = 700 nm). Considering the high roughness of the spray-coated BHJ (rms roughness of ~200 nm) and the limits of the fabrication process, it can reasonably assume that the OPDs here compared have about the same electrical properties.

After BHJ deposition all samples are annealed at 140 °C for 5 min in inert conditions before thermal evaporation of 100 nm of Al as top electrode through a shadow mask. Diodes are encapsulated with solvent-free epoxy glue and a 100 mm thick transparent glass slide. Finally, OPDs are annealed at 80 °C for 30 min on a hotplate.

Current-voltage measurements of the four OPD stacks are shown in Fig. 4.5a. Independently of the IL the diodes exhibit comparable low dark currents of ~2 10^{-5} mA cm^{-2} at -5 V reverse bias and EQEs higher than 70 % in the visible range, Fig. 4.5b. Series resistance for all ILs measured at 1 V forward bias range from 250 Ω to

1 kΩ. The rectification ratio at +/-1 V is the highest for the OPD with P3HT IL with 1.27 10^6 due to the lowest series resistance. All other devices have comparable rectification ratios of 2.9 10^5 (SAM IL), 1.6 10^5 (PEDOT:PSS IL), and 4 10^5 (without IL) respectively. A note should be done about the diodes behaviour in solar cell mode, when no bias is applied. On the OPD without IL, the built-in electric field is too weak to fully extract photogenerated charges if low bias is applied and a negative bias is required to maintain a large photocurrent collection efficiency which results in a high EQE at -5 V reverse bias. It should also be noted that the diode with SAM IL and without IL are not favourable for solar cell applications, since the low current at 0 V and the fill factor are resulting in poor power efficiency. On the other hand, photodiodes are normally operating under reverse bias, which ensures good quantum efficiency (~70 % at -5 V) while still keeping the dark current low. Note that for biases < -0.5 V the OPD with P3HT IL shows a higher photocurrent compared to the device with PEDOT:PSS IL, in agreement with [Oh 2011].

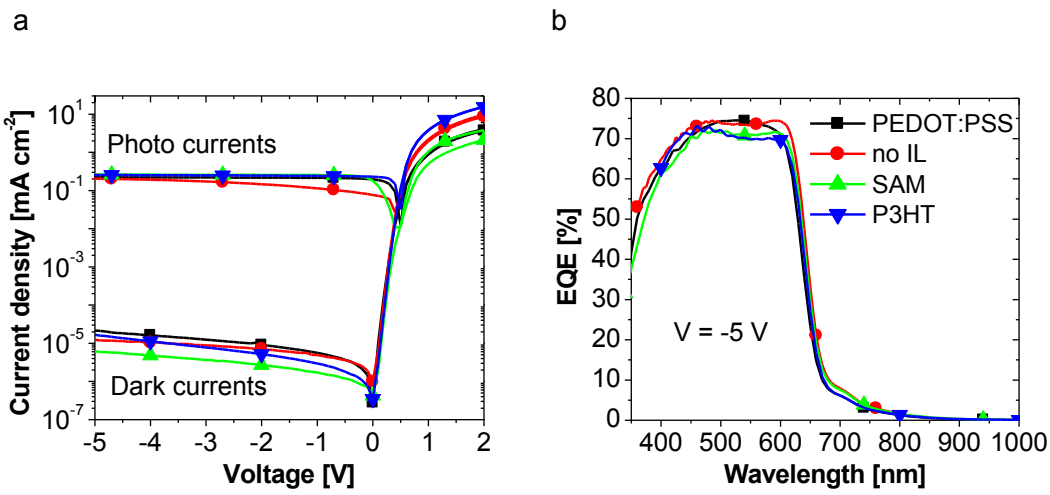

Figure 4.5: a) Dark and photocurrent characteristics of OPDs with PEDOT:PSS, P3HT, SAM, and without IL (light illumination at 532 nm and 780 µW cm^{-2}). b) EQE plot of OPDs with PEDOT:PSS, P3HT and SAM as IL and without IL. Measurements performed at V = -5 V.

Fig. 4.6a shows dynamic measurements of the OPD with PEDOT:PSS IL for various green light intensities, which is the reference diode since PEDOT:PSS is the most commonly used IL for organic diodes. For high-light intensities of ~276 µW cm^{-2} at 532 nm wavelength the diode shows a cut-off frequency of about 71 kHz, comparable to reported values [Baierl 2011]. The cut-off frequency degrades to a few Hz when

reducing the light intensity down to 20 nW cm^{-2}, i.e. a response time roll-off of five decades while varying the light intensity over four orders of magnitudes. Similar dependencies of the cut-off frequency on the light intensity are observed with all other ILs yet the low-light level response time differs significantly between diodes with different ILs which is not related to the serial resistance of the devices. In Fig. 4.6b the amplitude Bode diagram for the OPD without IL is shown for comparison.

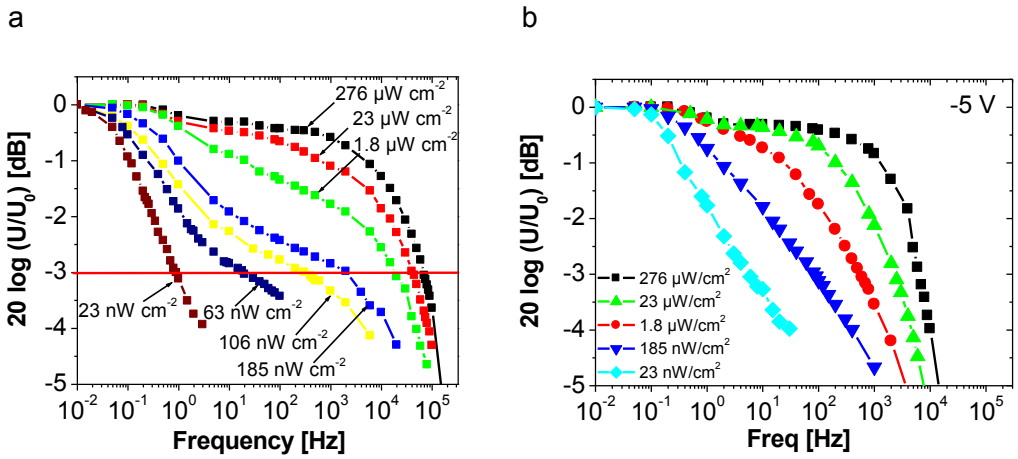

Figure 4.6 Amplitude Bode plots of a -5 V reverse biased OPD with a) PEDOT:PSS IL and b) without IL with varying pulsed green light illumination ranging from 276 µW cm^{-2} to 23 nW cm^{-2}.

The cut-off frequency dependency on the light intensity for all OPDs polarized at -5 V is summarized in Fig. 4.7a. PEDOT:PSS as well as P3HT are favourable as IL for high response time at light intensities > 200 nW cm^{-2}, with cut-off frequencies in the kHz regime. However, below 200 nW cm^{-2} the cut-off frequency of the device with PEDOT:PSS IL drops almost exponentially to a few Hz while the temporal response of the OPD with P3HT IL remains relatively stable in the nW cm^{-2} regime.

OPDs with SAM IL have always a slightly lower cut-off frequency than OPDs with P3HT IL with a relatively stable response time at illuminations < 200 nW cm^{-2}. Devices without IL have the lowest response time throughout the observed light levels but show an even better characteristic than the reference OPD at intensities < 50 nW cm^{-2}. Bode plot characteristics Fig. 4.6a exemplary shown for a device with PEDOT:PSS IL and without IL (Fig. 4.6b) as well as crossing points of the cut-off frequencies of sensors with different ILs (Fig. 4.7a) are significant and show a dramatic influence of the IL. No

such pronounced effects on the diode speed are observed by varying cathode materials such as Ca/Ag or Al, Fig. 4.7b.

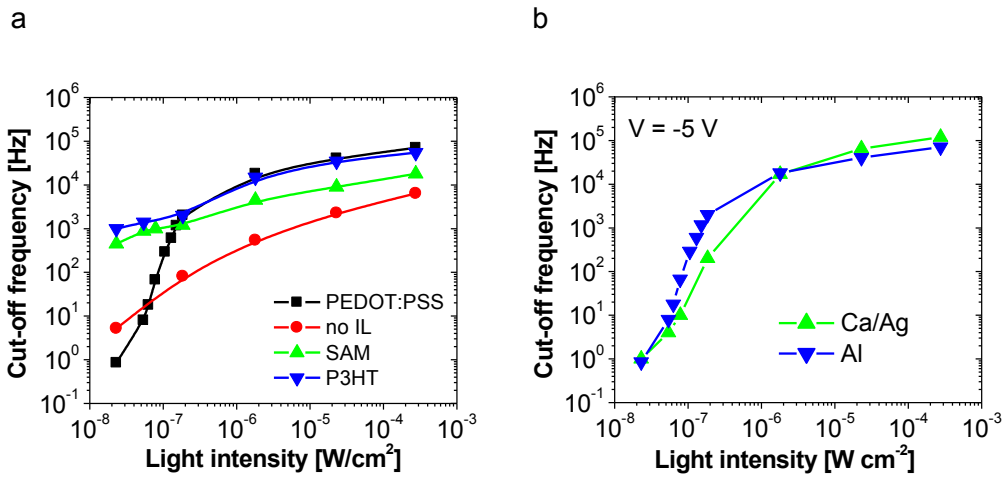

Figure 4.7: a) Response time dependence on light intensities of OPDs with PEDOT:PSS, P3HT, SAM, and without IL. b) Cut-off frequency vs. light intensity of two diodes both with PEDOT:PSS IL, one with Ca/Ag and the second with Al as top electrode. Measurements performed at V = -5 V.

It is also observed that OPD cut-off frequency varies with the bias. Cut-off frequency increases with increasing reverse bias due to the higher internal electric field that improves charge extraction. Furthermore, cut-off frequency varies also with the semiconductor thickness. In particular, the cut-off frequency decreases with increasing semiconductor thickness due to recombination (Fig. 4.8a-d).

On Fig. 4.8a-b amplitude Bode diagram measurements on 2 OPDs with spin-coated PEDOT:PSS IL (~150 nm), thermally evaporated Al (~100 nm) as cathode and spray-coated P3HT:PCBM BHJ (P3HT:PCBM 1:0.75 wt. in xylene) with thickness of ~500 nm and ~700 nm are presented. The applied bias is varied from 0 V to -5 V. The -3dB cut-off frequencies as function of the applied voltage are summarized in Fig. 4.8c. Increasing the applied bias the cut-off frequency increases due to the higher internal electric field. High values for the cut-off frequency are measured on thin diodes (Fig. 4.8c).

On a device with PEDOT:PSS as IL, varying the BHJ thickness by 30 % has an insignificant effect on temporal characteristics of the diodes (Fig. 4.8d).

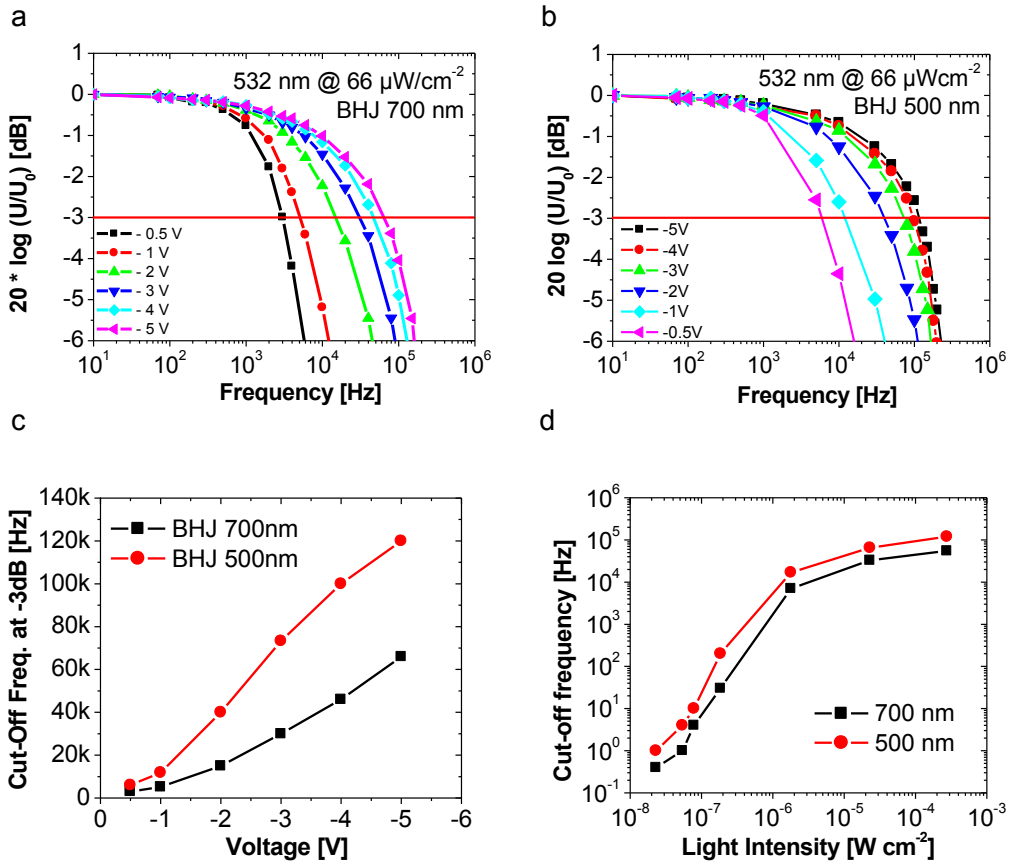

Figure 4.8 Amplitude Bode diagram for 2 OPDs with PEDOT:PSS IL with a) 500 nm BHJ thickness and b) 700 nm. Cut-off frequency for the same diodes with varying c) the reverse bias and d) the light intensity. Measurements performed at V = -5 V.

Semiconductor thickness is related to the amount of time required by the carriers to reach the electrodes. The thicker the detector, the longer the transit time will be.

$$t_{tr} = \frac{d}{v_{dr}} = \frac{d}{\mu F} = \frac{d^2}{\mu V} \qquad (4.1)$$

Finally in Fig. 4.9 variation of the cut-off frequency with the light intensity as function of the applied reverse voltage for an OPD with PEDOT:PSS IL is presented. For high light intensity a variation of the cut-off frequency by about one order of magnitude is observed, while for low light intensity cut-off frequency values are comparable.

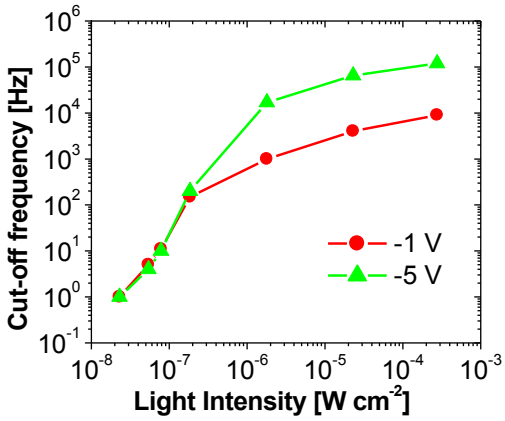

Figure 4.9 Cut-off frequency vs. light intensity on the OPD with PEDOT:PSS IL by varying the reverse bias.

In general any change in the photodiode stack to optimize the transit time affects also the dynamic response, the dark current, and the quantum efficiency. A fast transit time requires a thin film detector, while low OPD capacitance requires a thick active layer.

Figure 4.10 shows statistics on OPDs with different ILs. Dynamic response measurements are reproducible on a variety of OPDs. From these measurements and observations seems that the predominant factor in the variation of the cut-off frequency is given by the IL/semiconductor interface, which indicates a strong influence of IL/BHJ interface traps on the OPD dynamic response and can only be observed at low-light levels. Table 4.1 summarizes experimental observations and suggests the following charge transport phenomenon in the OPDs. At high light levels such as 780 μW cm^{-2} the density of the photons hitting the surface is ~2 10^{15} photons cm^{-2} s. A large number of charge carriers are generated in excess of the trap states at the interface. Hence, interface traps can be filled without any visible degradation of the photocurrent. The device response time is therefore dominated by a capture and emission process and by the time constant of the volume traps. In strong contrast, at very low-light levels such as 20 nW cm^{-2}, corresponding to an incident photon density of ~5 10^{10} photons cm^{-2} s only few charge carriers are generated and the time constant of the interface traps determines the cut-off frequency of the device. Introducing a new IL to replace the PEDOT:PSS apparently changes the trap emission and capture rate at the interface.

In brief, at low-light levels traps are not fully filled and their occupation change over time.

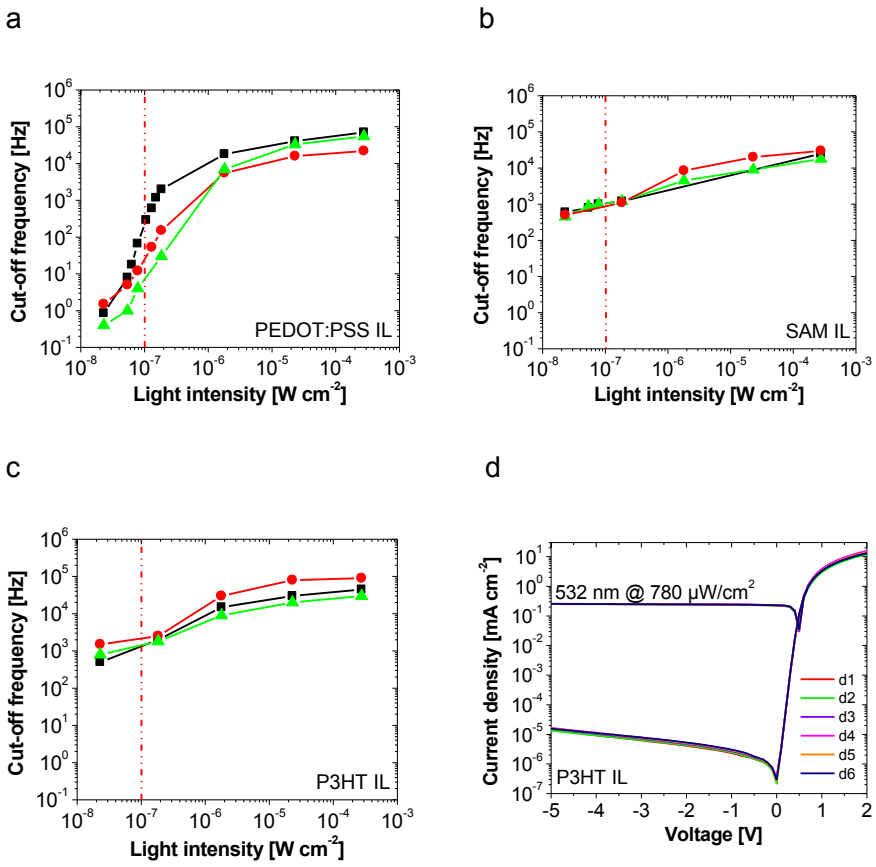

Figure 4.10. Cut-off frequency measurements statistic on three OPDs with a) PEDOT:PSS IL, b) SAM IL and c) P3HT IL. The vertical line at 10^{-7} W cm^2 is a guide for the eyes to easily identify the low light intensity regime. d) IV overlap of six 1 cm^2 active area OPDs with P3HT IL processed from different batches.

Due to the IL properties the hole extraction efficiency will result in a modified dynamic response of the OPD over three orders of magnitudes. The nature of this trapping and de-trapping mechanism is not clear and difficult to assess experimentally but the influence of the IL on the dynamic response seems obvious.

To conclude the paragraph, experimentally it is observed that devices without IL present always a rectification behaviour and an extremely low dark current densities of ~10^{-5} mA cm^2 at -5 V reverse bias in agreement with [Ramuz 2008].

	Low power (nW cm^{-2})	High power (µW cm^{-2})
Low frequency (Hz)	- Few charge carriers generated - Majority of charge carriers trapped at the interface - Trapped carriers considerably affect the measured diode current	- Large number of charge carriers generated - Carriers exceed the number of trap states at the interface (the upper limit depends on trap parameters and carrier concentrations) - Interface traps are filled without any visible degradation of the photocurrent
High frequency (kHz)	- Time constant of the interface traps determines the cut-off frequency of the device	- Effect of the surface traps is still negligible like at low frequencies - Cut-off frequency is given by the time constant of the volume traps, which are present in a high concentration

Table 4.1: Trap influence on the dynamic response of the OPD.

According with the literature [Ramuz 2008] [Liang 2009] the lowest dark current density of ~ 2 10^{-6} mA cm^{-2} at -5 V reverse bias is measured on an OPD with P3HT IL (Fig. 4.11). The diode has 5.3 cm^2 active area and stack ITO/P3HT/BHJ/Al. P3HT is spray-coated from a xylene solution (1% wt.) in a layer of ~70 nm while the semiconductor (P3HT:PCBM blend 1:0.75 wt. in xylene) is spray-coated onto the IL in a layer thickness of ~700 nm. Finally, ~100 nm of Al are thermally evaporated.

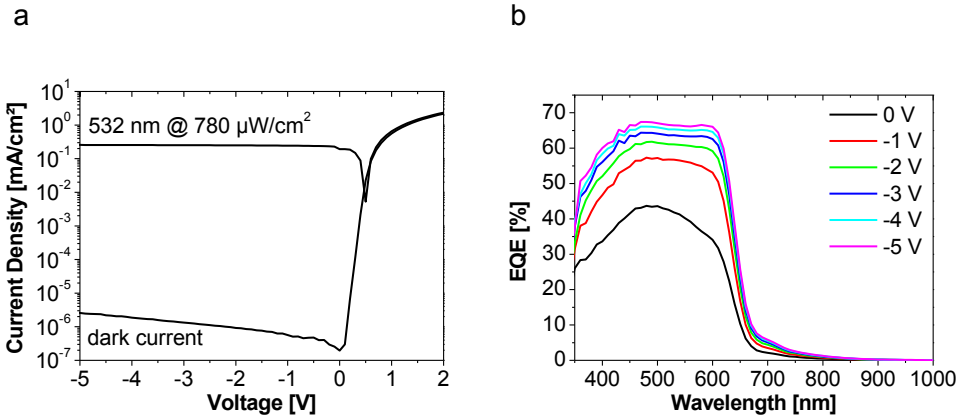

Figure 4.11. a) IV measured on a 5.3 cm^2 OPD with stack ITO/P3HT/BHJ/Al. b) EQE measured on the same diode from 0 to -5 V reverse bias.

4.3 OPDs with two interlayers

In this paragraph OPDs fabricated with 2 ILs are presented.

OPD dynamic characteristics are strongly influenced by the anode/semiconductor interface. In particular OPD cut-off frequency at low light intensity of nW/cm^2 can be varied several orders of magnitude by tuning the interface, for example by varying the used IL. It is of interest to check the behaviour of an organic photodiode fabricated with two different IL materials. Despite organic sensors with two ILs have been already presented [Oh 2011], no dynamic response is reported.

In Fig. 4.12 static and dynamic measurements performed on a 1 cm^2 OPD with PEDOT:PSS and P3HT ILs are presented (stack: ITO/PEDOT:PSS/P3HT/BHJ/Al), similarly as [Oh 2011]. After cleaning a structured and passivated ITO substrate, ITO surface is activated by RIE and ~150 nm of PEDOT:PSS HIL 3.3N are deposited on the ITO surface by spin-coating as first IL. Layer is backed at 200 °C for 15 min in a vacuum oven. Onto the PEDOT:PSS layer a ~80 nm P3HT layer is created by spray-coating a P3HT solution (1% wt.) in xylene as second IL. The BHJ (~700 nm thick) is spray-coated onto the P3HT layer from a solution of P3HT:PCBM 1:0.75 wt. in xylene. Device is annealed at 140 °C for 5 min before deposition of ~100 nm of Al by thermal evaporation. OPD is finally sealed with epoxy glue and a thin glass slide.

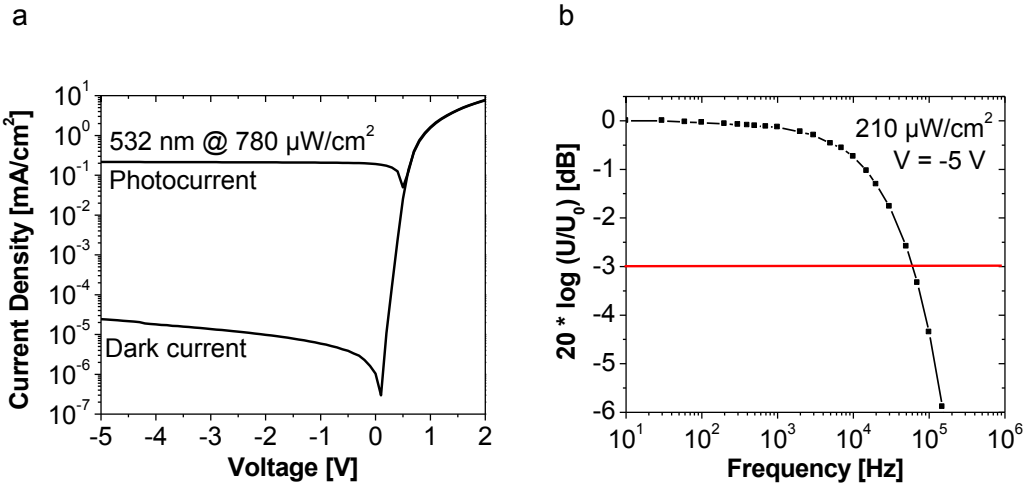

Figure 4.12: 1 cm^2 OPD with PEDOT:PSS and P3HT as ILs. a) IV in dark and under green light illumination (532 nm @ 780 µW cm^{-2}). b) Bode amplitude diagram.

The fabricated OPD with PEDOT:PSS and P3HT as ILs shows dark current densities of ~2.4 10^{-5} mA/cm^2 at -5 V reverse bias and a series resistance at +2 V of ~260 Ω, comparable with the IV measured on diodes with single IL. An EQE > 70 % in the visible range (data not shown) is observed and a cut-off frequency of ~60 kHz at -5 V reverse bias with light intensity of ~210 µW cm^{-2} is measured, Fig. 4.12b.

Due to the fast dynamic response under low light illumination observed on organic diodes with SAM and P3HT as ILs, an OPD with both ILs is created with the aim to improve the device performance.

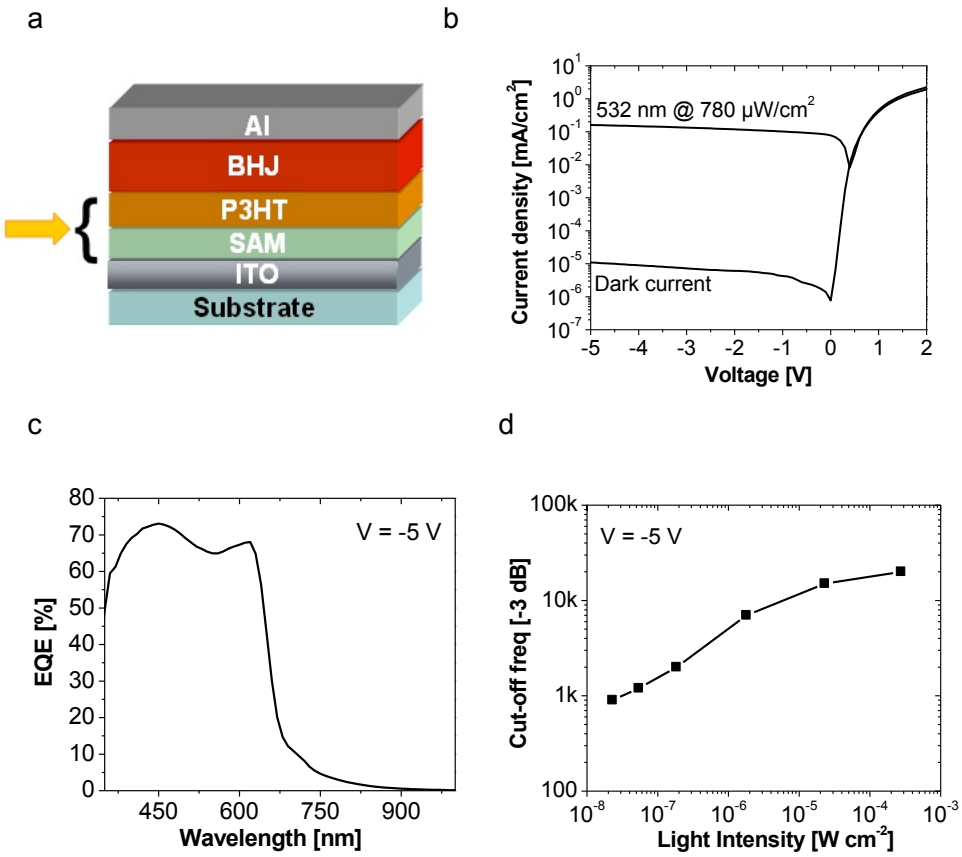

Figure 4.13 a) Layer stack of a 1 cm^2 OPD with SAM and P3HT as ILs. b) IV of the OPD in the dark and with green light illumination (780 µW/cm^2). c) EQE of the OPD measured at -5 V reverse bias. d) Dynamic measurements with varying light intensity.

In Fig. 4.13a the stack of the fabricated OPD is shown. A structured and passivated ITO substrate is cleaned and the ITO surface activated by RIE. A SAM layer as first IL for the OPD is than fabricated onto the ITO film by immersing the ITO substrate on an isopropanol solution of Octadecylphosphonicacid until a contact angle > 110° is observed. Onto the SAM film a ~70 nm P3HT layer is created by spray-coating a P3HT solution (1% wt.) in xylene as second IL. The BHJ (~700 nm thick) is spray-coated onto the P3HT layer from a solution of P3HT:PCBM 1:0.75 wt. in xylene. Device is annealed at 140 °C for 5 min before deposition of ~100 nm of Al by thermal evaporation. OPD is finally sealed with epoxy glue and a thin glass slide.
Diode IV (Fig. 4.13b) shows a dark current density of ~1 10^{-5} mA/cm^2 at -5 V reverse bias and a series resistance measured at +2 V of ~1 kΩ. Rectification ratio at +/- 2 V is ~3 10^5 and an EQE of ~70 % in the visible range is observed, Fig. 4.13c. Reduction of the EQE for green wavelength is probably due to the light absorption by both ILs. Finally, Fig. 4.13d shows dynamic measurements on the diode at -5 V reverse bias with cut-off frequency at low light levels of ~1 kHz, comparable with measured values on OPD with single IL.

In conclusion, with two ILs no further dark current reduction is observed and measured EQEs are comparable with EQE of devices with only P3HT or SAM. Dynamic response with varying light intensity appears also not affected.

4.4 Photodiode Area-upscale

In this paragraph influence of the active area on OPD characteristics such as IV, EQE and dynamic response is presented.

Three OPDs with active area of 4 mm^2, 1 cm^2 and 5 cm^2 are fabricated on different substrates. After cleaning the ITO substrates, RIE plasma is applied before the spray-coating of ~80 nm of P3HT as IL from a 1% wt. solution in xylene. Onto the P3HT IL a BHJ from a xylene solution of P3HT and PCBM (P3HT:PCBM 1:0.75 wt.) is spray-coated resulting in a layer thickness of ~550 nm. Finally ~100 nm of Al are thermally evaporated as cathode and each device is sealed with epoxy glue and a thin glass slide.

Figure 4.14 shows a bottom view photo of the processed OPDs.

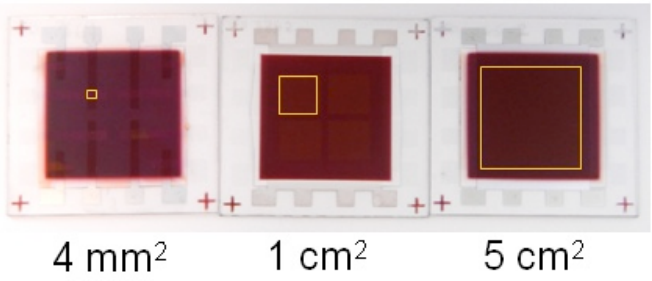

Figure 4.14. Optical pictures of 3 processed photodiodes with active area of 4 mm^2, 1 cm^2 and 5 cm^2. OPD active area is marked in yellow.

IV measurements from +2 V to -5 V reverse bias in dark and with green light illumination (532 nm @ 780 $\mu W/cm^2$) show no significant difference between the diodes (Fig. 4.15a). The light is applied through the transparent ITO electrode. All OPDs present comparable dark current densities at -5 V reverse bias of ~10^{-5} mA cm^{-2} and EQEs of ~70 % in the visible range (Fig. 4.15b). Similar low dark current values up to µm range pixel scale have been reported [Tedde PhD] indicating that OPD active area can be scaled several orders of magnitude with no effect on the diode characteristics.

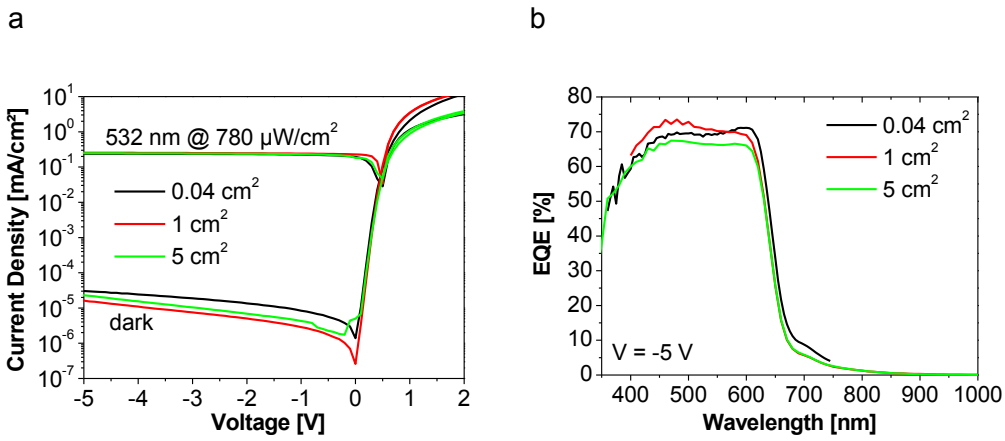

Figure 4.15 a) IV and b) EQE of three OPDs with active area of 4 mm^2, 1 cm^2 and 5 cm^2.

In Fig. 4.16 the amplitude Bode diagram measured on the same diodes is presented. No variation of the cut-off frequency with the diode area can be seen, in agreement with [Tedde PhD].

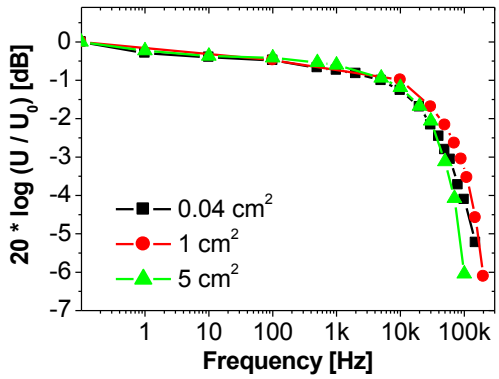

Figure 4.16 Amplitude Bode plot measured on OPDs with active area of 4 mm^2, 1 cm^2 and 5 cm^2 [532 nm @ 60 $\mu W/cm^2$]. Measurements performed at -5 V reverse bias.

Invariance of the cut-off frequency with the OPD active area can be explained by the invariance of the RC time constant. Due to the thin film planar architecture, OPD can be modelled as a capacitor with capacitance (C) and resistance (R) given by

$$C = \varepsilon_r \varepsilon_0 \frac{A}{d} \qquad R = \rho \frac{d}{A} \tag{4.2}$$

with A diode active area, ε_0 dielectric constant of vacuum, ε_r relative dielectric constant of the active layer (IL + semiconductor), d anode/cathode distance and ρ material resistivity. The OPD time constant is the RC product. In general large active areas correspond to slow photodiodes and vice versa. In particular organic photodiodes are usually characterized by high capacitance values due to the thin film active layer that limits the device dynamic response. As an example OPDs with a mean BHJ thickness of ~1 µm and 5 cm² active area have capacitances C and shunt resistances R_{SH} of ~23 nF and ~100 MΩ, respectively. The maximum cut-off frequency [Fukuda 1999] for the OPD only

$$f = \frac{1}{2\pi C R_{SHL}} \tag{4.3}$$

with $R_{SHL} = R_{SH}//R_L$ corresponding to a decrease of the voltage amplitude by $2^{-1/2}$ is calculated to be ~140 kHz. Despite this value seems low compared to c-Si devices, the actual bandwidth is usually further lower due to the low charge carrier mobility, charge trap phenomena, series resistance and capacitances of wire connections. Independence of the OPD cut-off frequency from the diode active area can be explained by a geometrical consideration: C and R are both functions of the diode area. With reducing the OPD active area the capacitance decreases but at the same time the bulk resistance proportionally rises, resulting in an invariant RC time constant [Tedde PhD].

OPD area up-scale is challenging, especially in the cm^2 range. To fabricate large active area devices substrate cleaning and spray-coating control are crucial since any impurity between anode and cathode can potentially result in a short. Next figure shows IVs overlap of 12 diodes in dark and under green light illumination (532 nm wavelength at 780 µW/cm^2). Diodes have been processed on independent substrates and each diode has an active area of 5 cm^2. In Fig. 4.17c dark current density statistics at -2 V and -5 V reverse bias are presented demonstrating that organic technology can show a good reproducibility, also on large active areas of several cm^2.

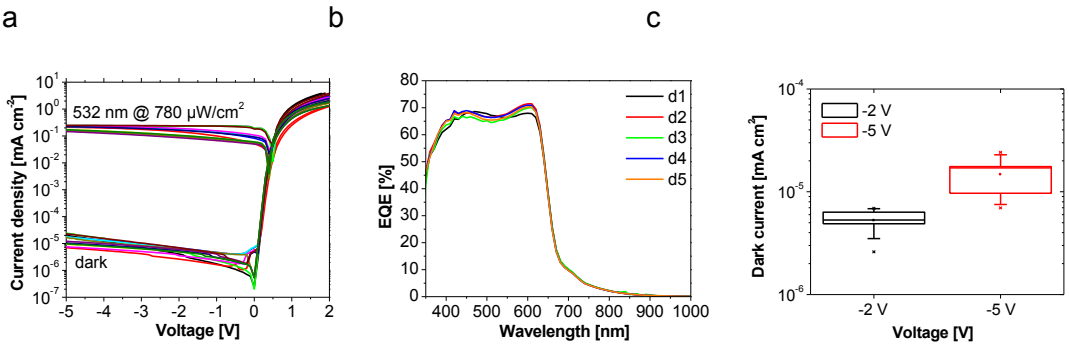

Figure 4.17: a) IV measurements in dark and under green light illumination of 12 OPDs with 5 cm^2 each active area. b) EQEs at -5 V reverse bias of five 5 cm^2 OPDs. c) Dark current statistics at -2 V and -5 V reverse bias.

4.5 Semiconductor solvent

In this paragraph effect of the solvent used for OPD fabrication is presented.

The solvent used to fabricate the OPDs can affect the diode characteristics. As an example, in 2008 Ramuz et al. [Ramuz 2008] compared two OPDs processed with chlorobenzene and 1,2-dichlorobenzene as BHJ solvents reporting about 10 % larger EQE for the OPD processed from 1,2-dichlorobenzene compared to the device processed with chlorobenzene. Seems that 1,2-dichlorobenzene spin-coated at low speed can favourites the self organization of the BHJ molecules, resulting in an improved device [Huang 2005]. Recently [Zoombelt 2008] reports that the morphology of the active layer in an organic photodiode or solar cell is important for the overall diode performance and that spray-coating from different solvents and thermal or solvent annealing affect charge separation efficiency and charge carrier mobility.

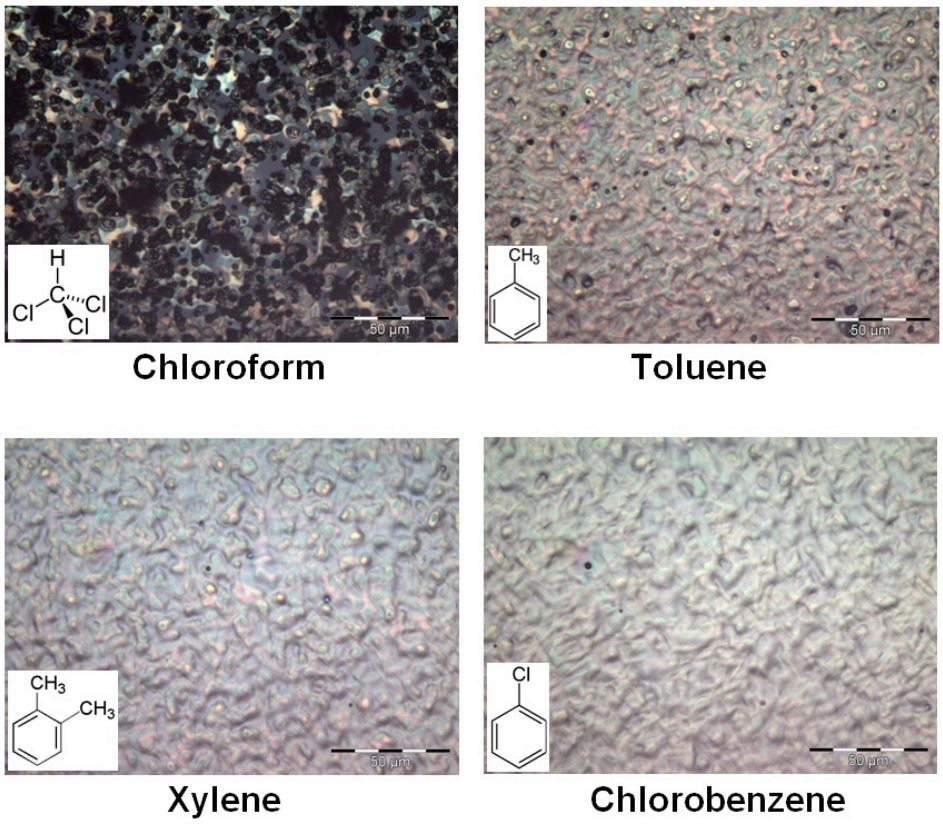

Figure 4.18. Optical microscope pictures of the BHJ (P3HT:PCBM 1:0.75 wt.) fabricated with different solvents. Inset shows the chemistry formula of each solvent.

Here, OPDs fabricated with different solvents are reported. P3HT and PCBM (1:0.75 wt.) are dissolved in chloroform, toluene, xylene and chlorobenzene and spray-coated on glass substrates resulting in a layer thickness of ~700 nm for all solvents. Fig. 4.18 shows optical pictures of the resulting layers. Similar layer morphology is observed for xylene, chlorobenzene and toluene which have similar chemical structure' while the use of chloroform results in a layer with completely different morphology.

In Fig. 4.19 profilometer analysis of the films is presented. BHJs fabricated with chlorobenzene, toluene and xylene show comparable film morphologies and the same surface roughness of ~200 nm. Chloroform film shows a completely different morphology with spikes of several micrometers. Blends fabricated by toluene, xylene and chlorobenzene formed smooth and uniform layers which suggest that a relative intimate mixing of the 2 components (P3HT:PCBM) exists. Measured spray-coated BHJ roughness values of ~200 nm are in agreement with literature [Tedde 2009].

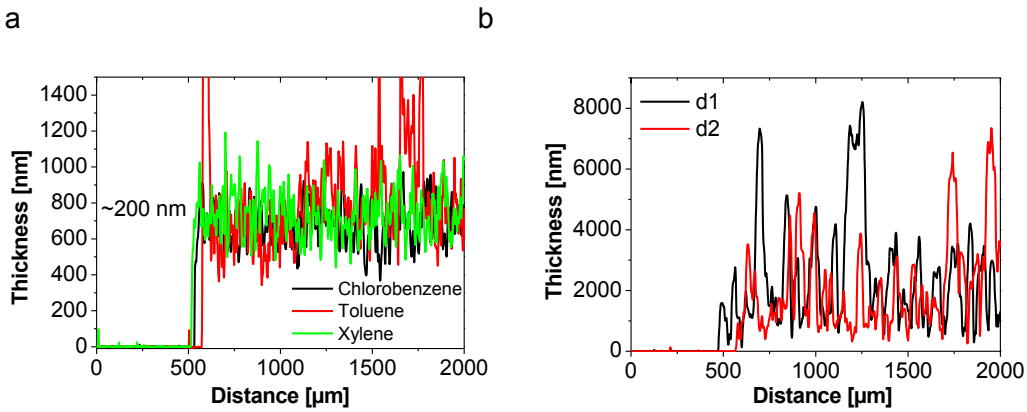

Figure 4.19. Profilometer measurements of spray-coated BHJs by varying the solvent. Two chloroform samples are shown for statistic.

Four different OPDs are fabricated by dissolving the BHJ in chloroform, toluene, xylene and chlorobenzene. The stack of the devices is ITO/P3HT/BHJ/Al. First, an ITO coated transparent glass is structured and passivated by ~1µm SU-8 layer. An active area of 1 cm^2 is fabricated by photolithography. After cleaning the substrates is acetone, isopropanol and deionized water, RIE is applied to activate the ITO surface. A P3HT IL ~70 nm is spray-coated onto the ITO from a xylene solution (1 % wt.) for all devices.

As solvent for the P3HT IL it has been used xylene for all OPDs, so the only difference between the stacks is the solvent of the BHJs and the devices are comparable. Four different BHJs (P3HT:PCBM 1:0.75 wt.) in chloroform, toluene, xylene and chlorobenzene have been sprayed onto the P3HT IL resulting in a layer thickness of ~600 nm. After an annealing step of 140 °C for 5 min, ~100 nm of Al are thermally evaporated and each diode is sealed with epoxy glue and a thin glass slide.
In Fig. 4.20 the measured IVs, EQEs and dynamic response of the resulting diodes are presented. OPDs fabricated using chloroform as solvent are all in short due do the bad semiconductor film morphology. Other OPDs show comparable performances with low dark currents densities of < 10^{-4} mA cm^2 at -5 V reverse bias and EQEs of ~65 % in the visible range. A cut-off frequency of ~1 kHz at low light intensities is observed for all devices (inset Fig. 4.20b).

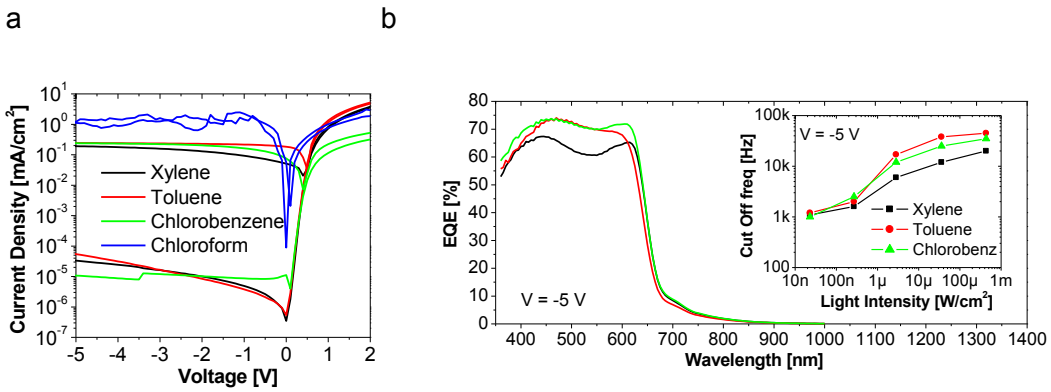

Figure 4.20. a) IVs and b) EQEs measured on OPDs with different solvents. Inset shows dynamic measurements with varying light intensity on OPDs fabricated with xylene, toluene and chlorobenzene.

4.6 Cathode material

In this paragraph influence of the cathode material on the diode performance is presented.

It is usually believed that OPD rectification behaviour and charge extraction depend by the work function difference between the anode and the cathode material. In this context, the cathode plays an important role to determine the final OPD characteristic. In brief, cathode materials strongly affect the diode behaviour by influencing the charge

collection efficiency. Here, OPDs fabricated with cathodes with different work functions ranging from ~2.8 eV to ~5.0 eV such as Ca (~2.8 eV) [Chu 2006], Al (~4.3 eV) [Michaelson 1977], ZnO (~4.45 eV) [Bulliard 2010], Cu (~4.7 eV) [Anderson 1949] and Au (~5.0 eV) [Chu 2006] [Michaelson 1977], are presented (Fig. 4.21). Work function values are take from the literature. The common ITO anode has a reported work function of ~4.7 eV [Parker 1994] [Balasubramanian 1991].

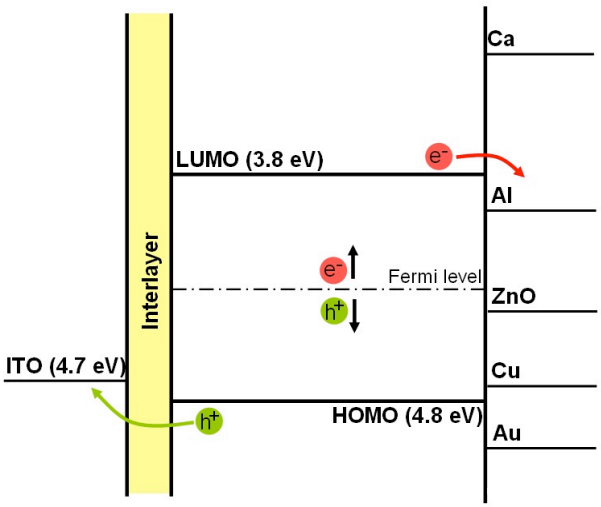

Figure 4.21. Flat band energy diagram of an OPD with P3HT and PCBM as active material and ITO as anode by varying cathode material.

In Fig. 4.21a the flat band diagram for an OPD with ITO as anode and P3HT:PCBM as semiconductor with varying cathode material is shown.

In Fig. 4.22 measured IVs in dark and with green illumination (532 nm @ 780 µW/cm^2) and EQEs on 1 cm^2 OPDs with Ca, Al, ZnO, Cu and Au as cathodes are shown. The layer stack of the OPDs is PEDOT:PSS/P3HT/BHJ/cathode. In brief, after cleaning a structured and passivated ITO substrate, RIE plasma is applied to activate the ITO surface. First 150 nm PEDOT:PSS are spin-coated onto the ITO and than ~80 nm of P3HT are sprayed onto PEDOT:PSS layer from a 1 % wt. solution in xylene. Than, ~700 nm of P3HT:PCBM (1:0.75 wt. in xylene) are spray-coated onto the IL, the devices are annealed at 140 °C for 5 min in ambient conditions and ~100 nm of Ca, Al, Cu or Au thermally evaporated as cathode. The ZnO cathode is deposited in ambient

conditions by spin-coating (~2000 rpm) onto the spray-coated BHJ layer from a dispersion of ZnO nanoparticles synthesized as described by Pacholski et al. [Pacholski 2002]. The device is than backed at 150 °C for 5 minutes on a hotplate resulting in a ZnO cathode layer of ~10 nm thickness. Because of the BHJ surface roughness of ~200 nm, the spin-coating process is repeated 6 times until a continuous layer of ~60 nm is obtained.
Finally, all OPDs are sealed with epoxy glue and a transparent glass slide.

The lowest dark current density of ~1 10^{-5} mA/cm^2 is achieved with Al or ZnO as cathodes. Cathodes with high work function such as Au or Cu result in inverted devices under green light illumination. Independently of the used cathode material, all OPDs show an EQE higher than 60 % at -5 V for green wavelength (550 nm). The device fabricated with Cu shows a gain phenomena with EQE > 100 % at low reverse bias of -1 V. The gain of a detector is defined by the ratio of the number of carriers extracted from the device to the external circuit and the number of the incident photons. The gain is > 100 % in photomultiplication devices. This effect has been observed in inorganic PD and is generally explained by impact ionization of the semiconductor under high reverse bias. Recently, the photogain effect has been observed also in organic semiconductors, despite in this case the originating mechanism is still not clear. For organic devices the impact ionization mechanism is not usually considered the main cause of the observed photogain effect. The impact ionization mechanism requires high reverse bias (high internal electric field) while photogain in organic devices is usually observed at low bias, like in this case (-3 V). In literature many examples of organic devices showing photogain effect are reported for different semiconductors such as for the n-type perylene pigment (N-methyl-3,4,9,10-perylenetetracarboxyl-diimide (Me-PTC) [Hiramoto 1993], naphthalene tetracarboxylic anhydride (NTCDA) [Katsume 1996] [Hiramoto 2002], a double-layered device consisting of NTCDA and phenethyl perylene pigment [N,N´-bis(phenylethyl)-perylene-3,4:9,10-bis(dicarboximide)] (PhEt-PTC) [Nakayama 2000]. In particular in 2007 Huang et al. [Huang 2007] reported a photogain mechanism measured on an organic device with ITO as anode, BCP (bathocuproine) and Al as cathode, PEDOT:PSS as IL, pentacene and C_{60} as active material. They explain the results by assuming that both the disordered structure of the C_{60} and the charge trapping effect at the C_{60}/PEDOT:PSS interface contribute to the photogain effect.

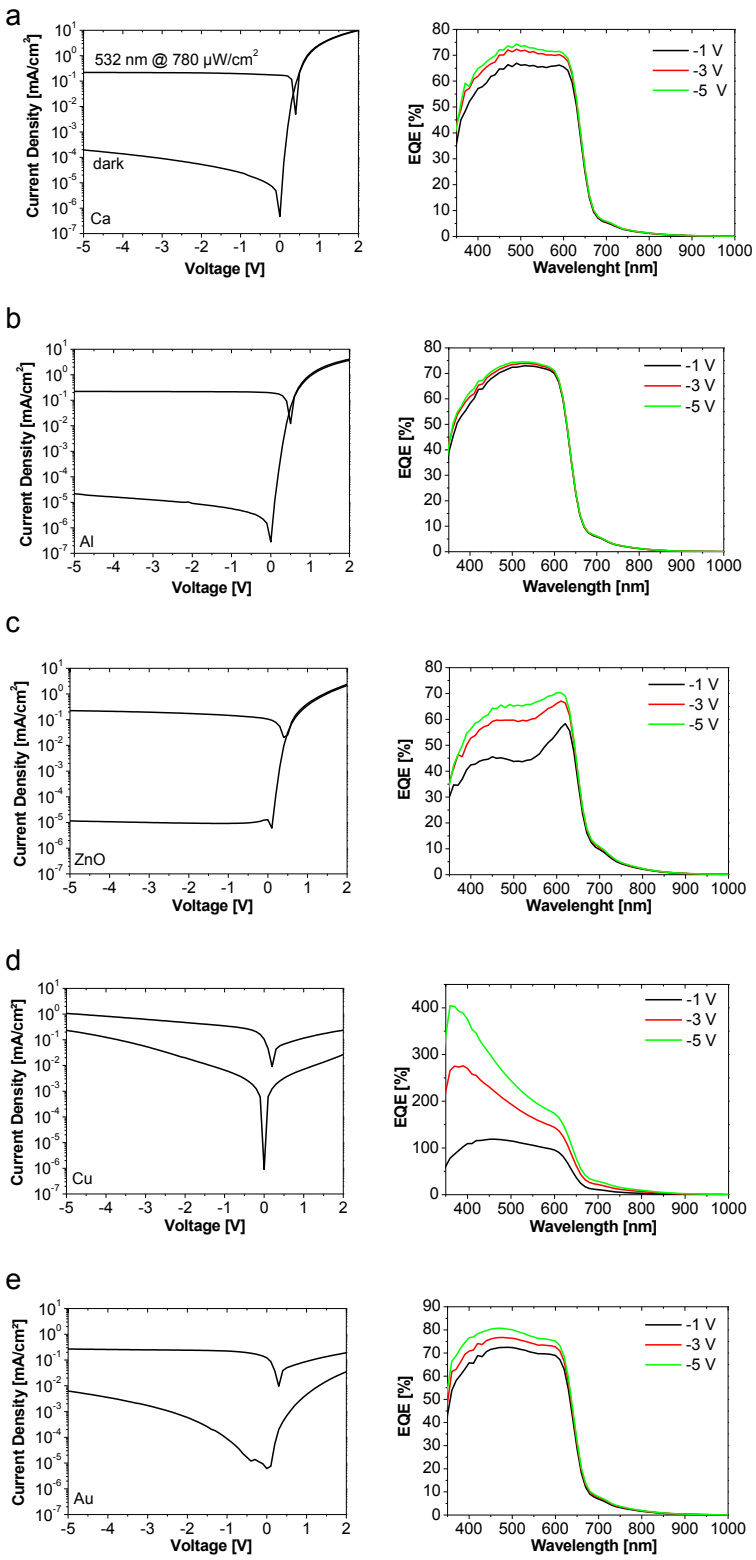

Figure 4.22. IV and EQE measurements of 1 cm^2 OPDs with different cathode materials.

They assume that the interfacial traps behave as an electronic valve that enables a significant increase in electron injection, which causes the photogain effect [Huang 2007].
Since photogain has been observed by many groups on devices with different stacks and materials, seems reasonable to conclude that the photocurrent multiplication arises from photoinduced electron injection occurring at the semiconductor/metal interface and not by the material itself. The conclusion is consistent with the data presented in Fig. 4.22, were the photomultiplication is observed with the BHJ/Cu interface only.

Correlation between the dark current density at -5 V reverse bias and rectification ratio at +/- 2V as function of the cathode material work function are summarized in Fig. 4.23.

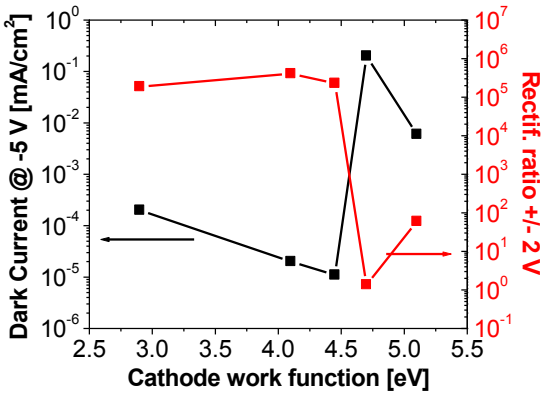

Figure 4.23 Dark current density at -5 V reverse bias and rectification ratio at +/- 2V measured on 1 cm^2 OPDs as function of the cathode material work function.

In conclusion there is no a clear trend between the OPD characteristics and the cathode work function. Despite Ca is considered the ideal cathode material (it maximize the work function difference between anode and cathode), best rectification ratios are achieved in this work with Al and ZnO. The use of Cu with work function similar to the ITO results in a OPD with EQE > 100 % while with a cathode with work function < ITO work function (Au) an EQE of ~75 % at -5 V is still observed. Contrary to what is expected, the use of Au as electrode results in a not reversed diode. In brief,

the flat band model presented in Fig. 4.21, developed and usually adopted for inorganic devices seems not suitable for organic device analysis.

4.7 Semiconductor thickness

In this paragraph effect of the BHJ thickness on the OPD characteristics is presented.

With the used spray-coating setup, semiconductor droplets size increase when increasing the spray-gun nozzle opening. When the generated droplets are big, do not dry on-fly and reach the substrate in a liquid state. The final film morphology is in this case not optimal. Usually best OPD characteristics are observed on spray-coated devices where spray-coated semiconductor droplets reach the substrate surface already dried. With the used setup and with one single spray-coating step a maximum of ~500 nm thick P3HT:PCBM BHJ layer can be fabricated due to the solubility limitations of the BHJ materials. To fabricate thick BHJ layers a concentrated BHJ solution or multiple spray steps are required, but P3HT solubility is ~1 % in common used organic solvents.

Fig. 4.24 shows microscopy images of a spray-coated P3HT:PCBM (1:0.75 wt.) blend with different mean thicknesses ranging from ~500 nm to ~70 µm, the last requiring ~150 spray-coating steps.

The BHJ roughness increases significantly with increasing layer thickness. Due to the absorption the BHJ colour gradually changes from pink to dark-brown, as shown in Fig. 4.25 for thicknesses up to ~2 µm.

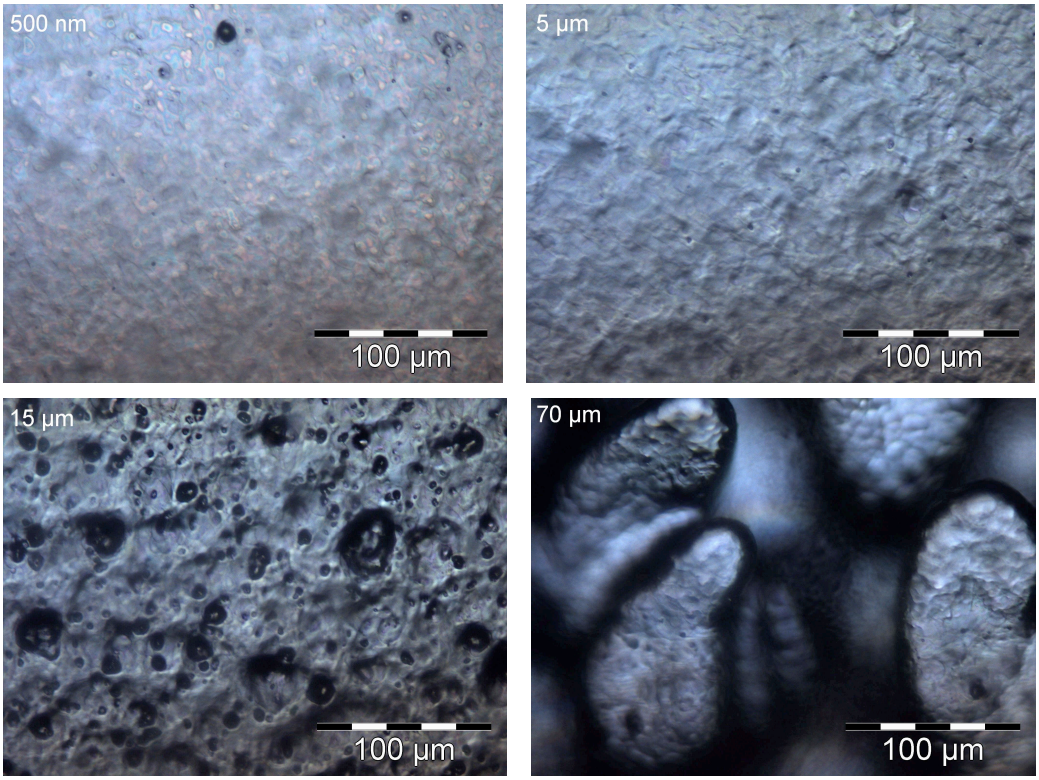

Fig. 4.24 Optical microscope pictures of spray-coated BHJ with mean thickness layers of 500 nm, 5 µm, 15 µm and 70 µm. Surface roughness increases with increasing spray-coating steps.

A moderate roughness until a film thickness of ~5 µm is observed (Fig. 4.26a). Thick films show a very pronounced increase of the film roughness due to agglomeration of the BHJ although if after each spray-coating step the deposited material is dried.

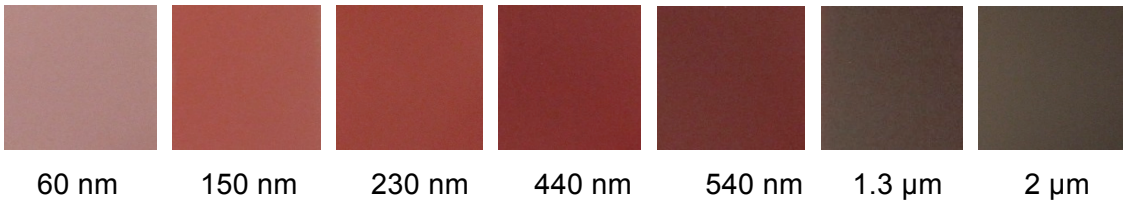

Figure 4.25: Film colours with varying spray-coated BHJ mean layer thickness from ~60 nm to ~2 µm. The colour varies from red for the thin film to black for the thick films.

In Fig. 4.26b the BHJ transmittance (T %) vs. BHJ layer thickness is presented. The spectra exhibit the characteristic π–π* band due to the electronic transitions in P3HT (maximum at λ = ~500 nm) [Sirringhaus 1999]. The shoulder near 2.1 eV is due to interchain excitons, resulting from π-stacking of the polymer chains in lamellar

aggregates [Brown 2003] [Piris 2009]. The peak at ~710 nm and the absorption of the blend at higher photon energy (λ < 400 nm) is due to the PCBM as is evident comparing the spectra in Fig. 4.26b (P3HT:PCBM blend) with the spectra in Fig. 4.26d (pristine P3HT).

With ~500 nm BHJ thickness the P3HT:PCBM blend absorbs > 95 % of the incident visible light. Note the pronounced absorption in the NIR with layer thicknesses beyond ~1 µm.

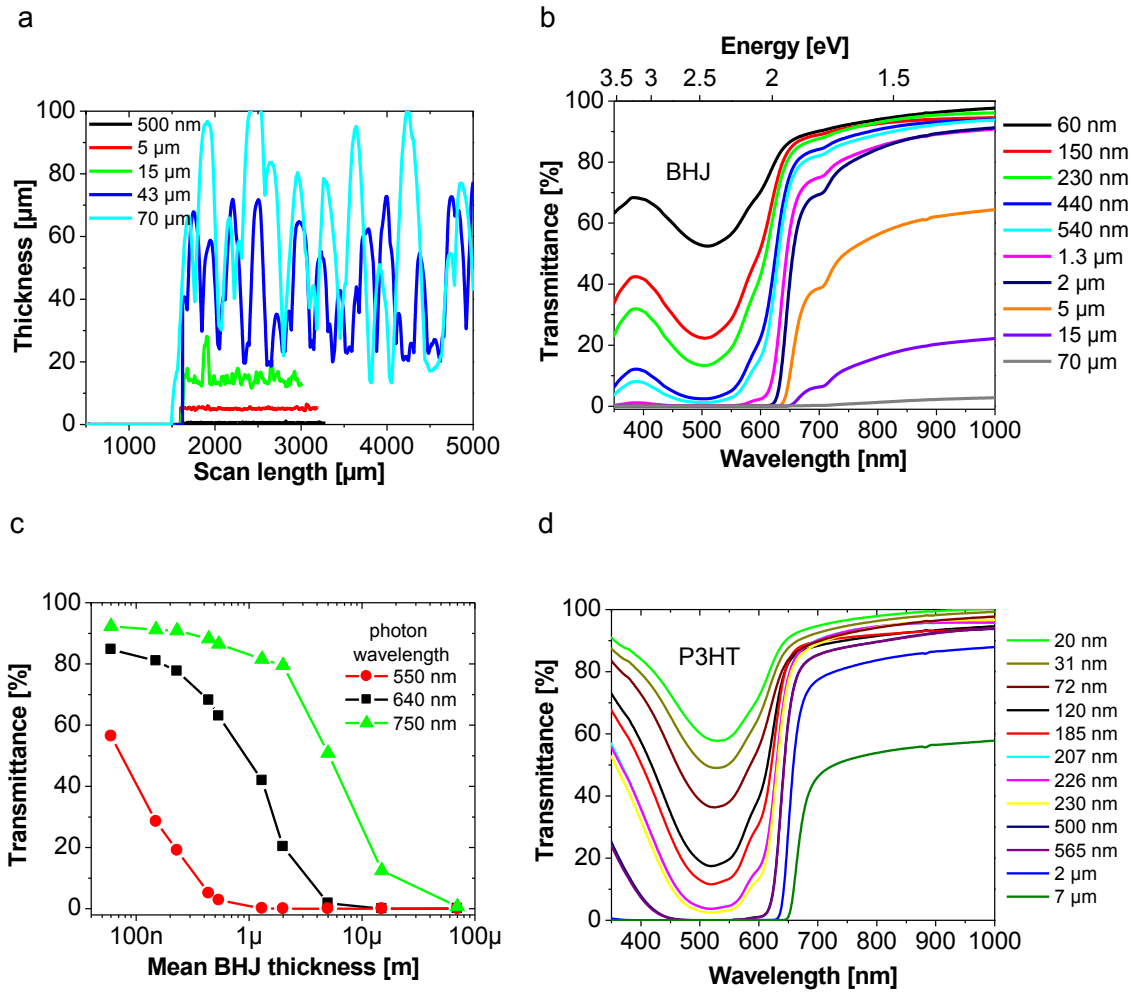

Figure 4.26: Thick P3HT:PCBM BHJ properties. a) Film roughness with varying the layer thickness (note: scan length up to ~4 mm). b) BHJ transmittance for layers varying from 60 nm to 70 µm. c) BHJ transmittance as function of the layer thickness for three different photon energies. d) P3HT transmittance with varying the layer thickness;

Photons with a wavelength of ~550 nm are absorbed in the first ~500 nm of the film while with increasing wavelength the penetration depth increases to several tens of µm for excitation at 750 nm. Photons with an energy < 2 eV penetrate the BHJ layer > 10 µm (Fig. 4.26c). This observation fits to the Lambert-Beer law.

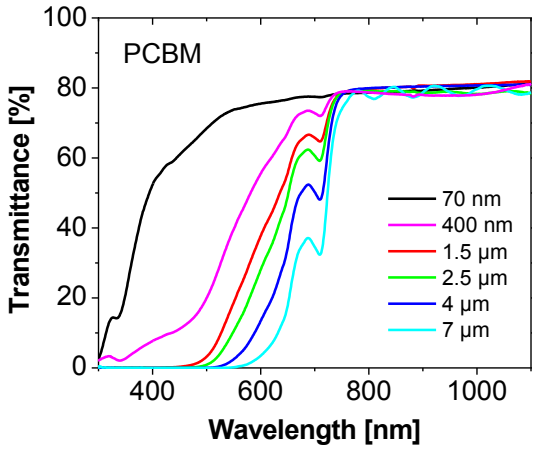

Figure 4.27: Transmittance measurements of spray-coated PCBM with varying the layer thickness from ~70 nm to ~7 µm.

Figure 4.27 shows transmission measurements on pristine PCBM films with varying thickness from ~70 nm to ~7 µm to confirm the nature of the stable peak at ~710 nm. As already reported by [Chen 2010] the PCBM absorption shows a red-shift with increasing thickness.

Here, the P3HT:PCBM absorption property of the thick film are applied to fabricate devices for NIR sensing. For thick OPD fabrication it is used PEDOT:PSS as IL and P3HT:PCBM (1:0.75 wt.) as active material. The BHJ is prepared from a xylene solution and spray-coated onto the IL with a mean thickness ranging from ~500 nm to ~36 µm. Al is thermally evaporated as cathode. Independent of the film roughness as result of the spray-coating process the diode characteristics show comparable dark current densities of ~10^{-5} mA cm^{-2} at -5 V reverse bias (Fig. 4.28a).

Photocurrents are measured with illumination through the bottom electrode at 532 nm with an irradiation intensity of ~780 µW cm^{-2}. The series resistance measured in the

dark at +2 V gradually increases from ~1.1 kΩ for the 500 nm thin diode to ~8.4 MΩ for the 36 µm thick OPD. At the same time with increasing the BHJ thickness the rectification ratio decreases due to the increasing series resistance (Fig. 4.28b).

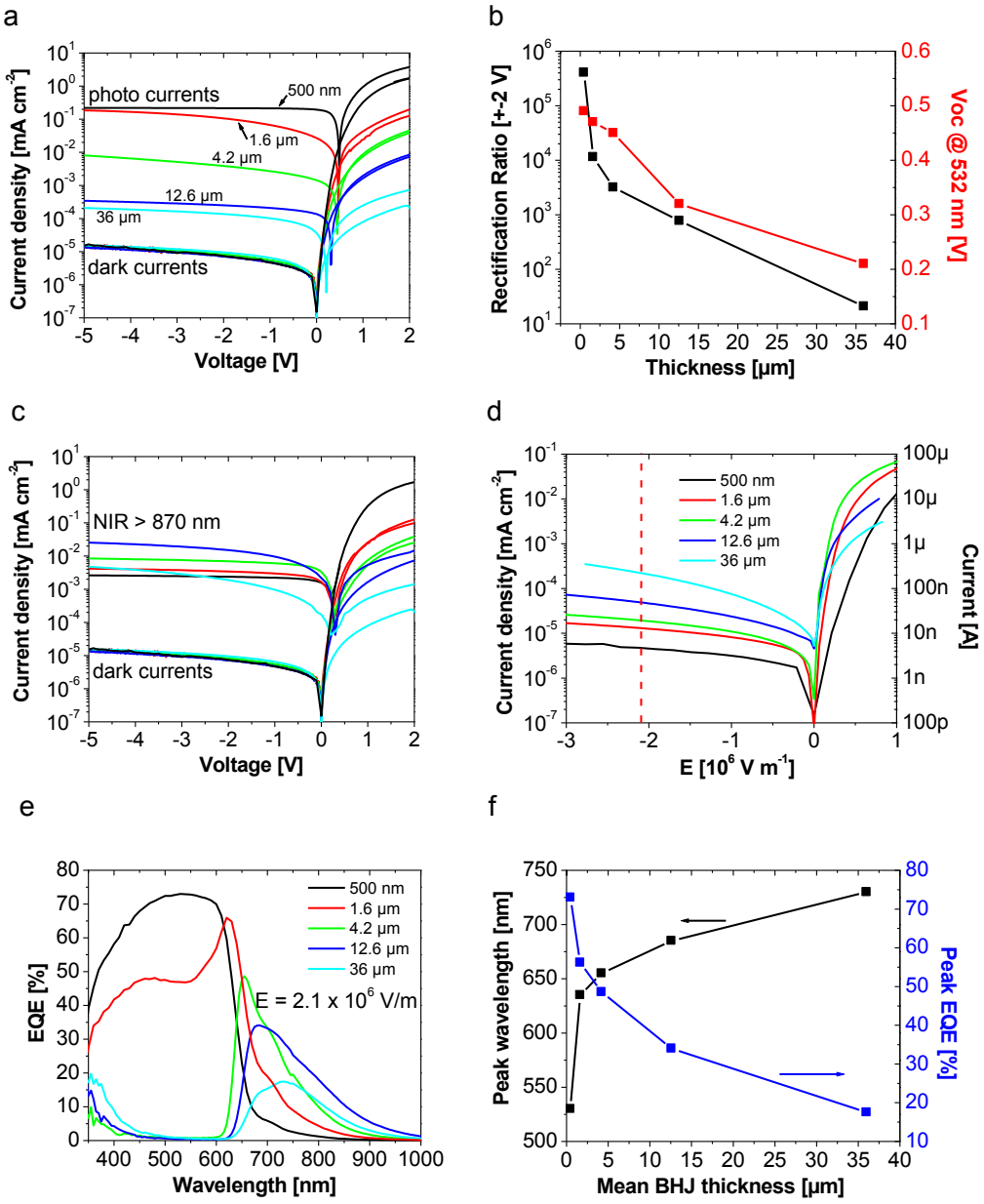

Figure 4.28: 1 cm^2 OPDs with P3HT:PCBM. a) IVs measurements on diodes with different BHJ mean thickness from 500 nm to 36 µm and b) Rectification ratio at +-2 V. c) NIR measurements on the same diodes. d) Dark measurements on the diodes as function of the internal electric field. e) EQEs measurements for a constant internal electric field of ~2.1 10^6 V m^{-1}. f) Peak wavelength and amplitude with varying the BHJ thickness.

With increasing active layer thickness the device characteristic is dominated by photoconductance. The photodoping effect at forward bias is relatively low for all diodes thicknesses.

The open circuit voltage decreases with increasing BHJ layer thickness in agreement with literature where a Voc decreasing with increasing device thickness for solid state dye-sensitized solar cells is reported [Snaith 2006].

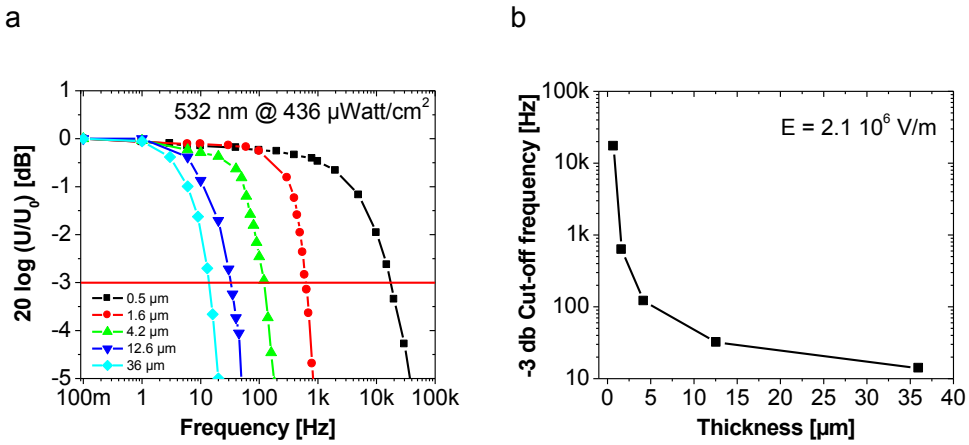

Figure 4.29: Thick OPDs dynamic response measurements. a) Amplitude Bode diagram measured on spray-coated OPDs with P3HT:PCBM (1:0.75) active layer with mean thickness from ~0.5 µm to ~36 µm using a green light illumination with ~436 µW cm2 intensity. b) -3db cut-off frequency vs. OPD BHJ mean thickness.

In Fig. 4.29 one can observe that due to the mobility the diode cut-off frequency decreases exponentially with the film thickness.

Figure 4.28c shows photocurrents measurements on the same diodes with a polychromatic NIR light > 870 nm. The photocurrent with < 1.9 eV photons (below the P3HT bandgap) gradually increases with increasing BHJ thickness which is consistent to the BHJ absorbance measurements (Fig. 4.26b). In Fig. 4.28d diode current densities vs. the internal OPD electric fields as a function of the bias $E = V\ d^{-1}$ (were V is the applied reverse voltage and d the mean active layer thickness) are presented. In strong contrast to an expected decrease of the dark current density with increasing layer thickness (for the same electrical field) the opposite phenomena is observed. The reason is not clear but appears to be not related to the electrical contacts and the

interfaces since are the same in all OPDs. EQEs (Fig. 4.28e) measured for a constant electric field of |E| = ~2.1 10^6 V m^{-1} show that with increasing blend thickness a red shift of the diode spectra from the visible to the NIR occurs. The increase of the infrared absorption with the film thickness indicates that the absorption is a bulk effect not related to interfaces [Yang 2008]. A red shift normally means increased packing of the P3HT domains. The spectral change of the P3HT film is thought to represent a different chain ordering of P3HT domains, the development of bigger aggregates or, more condensed moieties, which are composed of multiple interchain species of P3HT [Kim 2006].

It is interesting to note that thin diodes show sensitivities in the visible only. Increasing the BHJ thickness to ~1.6 µm produces an extension of the diode bandwidth and an EQE in both visible and NIR region. An EQE peak at ~640 nm can be identified. Diodes with BHJ thicknesses > 4 µm show NIR sensitivity only. The results are in good agreement with reported spectral sensitivities [Chen 2010] [Yang 2008]. In 2010 Chen et al. [Chen 2010] reported a similar spectral red shift on drop-casted diodes indicating that the spectral shift is a material property not related to the OPD fabrication process. Yang at al. [Yang 2008] observed such an NIR absorption which exists only in the blend and discussed this as a charge transfer exciton phenomena. Similar results were reported by [Osikowicz 2007] [Parkinson 2008]. EQE peak at λ = ~640 nm suggest that in thin OPDs charge transport is related to both PCBM and P3HT [Sariciftci 1992] while with thick diodes the P3HT transport dominates. The transition indicates that recombination losses lead to an in-built filtering of the visible spectra.

BHJ thickness	EQE max	λ (EQE max)	T (%)	Loss (%) (100 –T – EQE)
0.5 µm	73 %	530 nm	~ 3.3 (λ = 530 nm)	~24
1.6 µm	66 %	620 nm	~ 10 (λ = 620 nm)	~24
4.2 µm	48 %	655 nm	~ 17 (λ = 655 nm)	~35
12.6 µm	34 %	685 nm	~ 5.7 (λ = 685 nm)	~60
36 µm	17 %	730 nm	~ 3 (λ = 730 nm)	~80

Table 4.2: Thick OPDs parameters. Maximum of the EQE and corresponding wavelength, film transmittance and percentage loss as function of the BHJ mean thickness.

Table 4.2 correlates the OPD BHJ mean thickness with the wavelength corresponding to the maximum EQE and the transmittance at the same wavelength.

Increasing the BHJ thickness the maximum EQE amplitude decreases while the corresponding wavelength shows a right shift from ~530 nm to ~730 nm. At the same time the BHJ transmittance for the same wavelengths decreases with increasing BHJ thickness. Assuming negligible reflection losses at the anode interface, we can derive the losses by recombination mechanism subtracting the transmittance and the EQE from the total amount of light applied to the device, so 100 (%) – T (%) – EQE (%). The calculated losses are shown in Table 4.2. A trend can be identified, with the losses increasing with increasing the BHJ thickness. It is important to note that charge carrier recombination increases with the BHJ thickness or distance that the charges need to travel to their respective electrodes. When the BHJ thickness is higher than the photon penetration deep, which is true for > 2 eV photons, excitons are generated in the first layers of the film while the remaining BHJ behaves as a pure resistor were recombination reduces the diode current. Low energy photons (< 2 eV) penetrate deeper into the material. Hence, the equivalent resistive BHJ is smaller than in the case for > 2 eV photons, with lower recombination probability resulting in an increased photocurrent.

Last, Fig. 4.28f shows the correlation between peak wavelength and peak EQE vs. BHJ thickness. The EQE peak rolls off from 73 % for a ~500 nm thin diode to 17.5 % for a ~36 µm thick BHJ OPD. At the same time the EQE peak shifts from λ = ~520 nm to the NIR with λ = ~730 nm (Fig. 4.28f, black line). Similar EQE shift can be observed on the diode EQEs measured from 0 V to – 5 V reverse bias (Fig. 4.30).

In Fig. 4.30 can be observed that the spectral sensitivity is not influenced by the internal electric field but the charge extraction efficiency is increasing, except for the diode with a thickness of 1.6 µm. With an OPD in Fig. 4.30b having a mean BHJ thickness of 1.6 µm the transition between a broadband sensitivity (visible and NIR) to an only NIR-sensitive device is a function of the applied reverse voltage. The charge extraction of charge carriers generated by visible light is strongly influenced by the applied electric field.

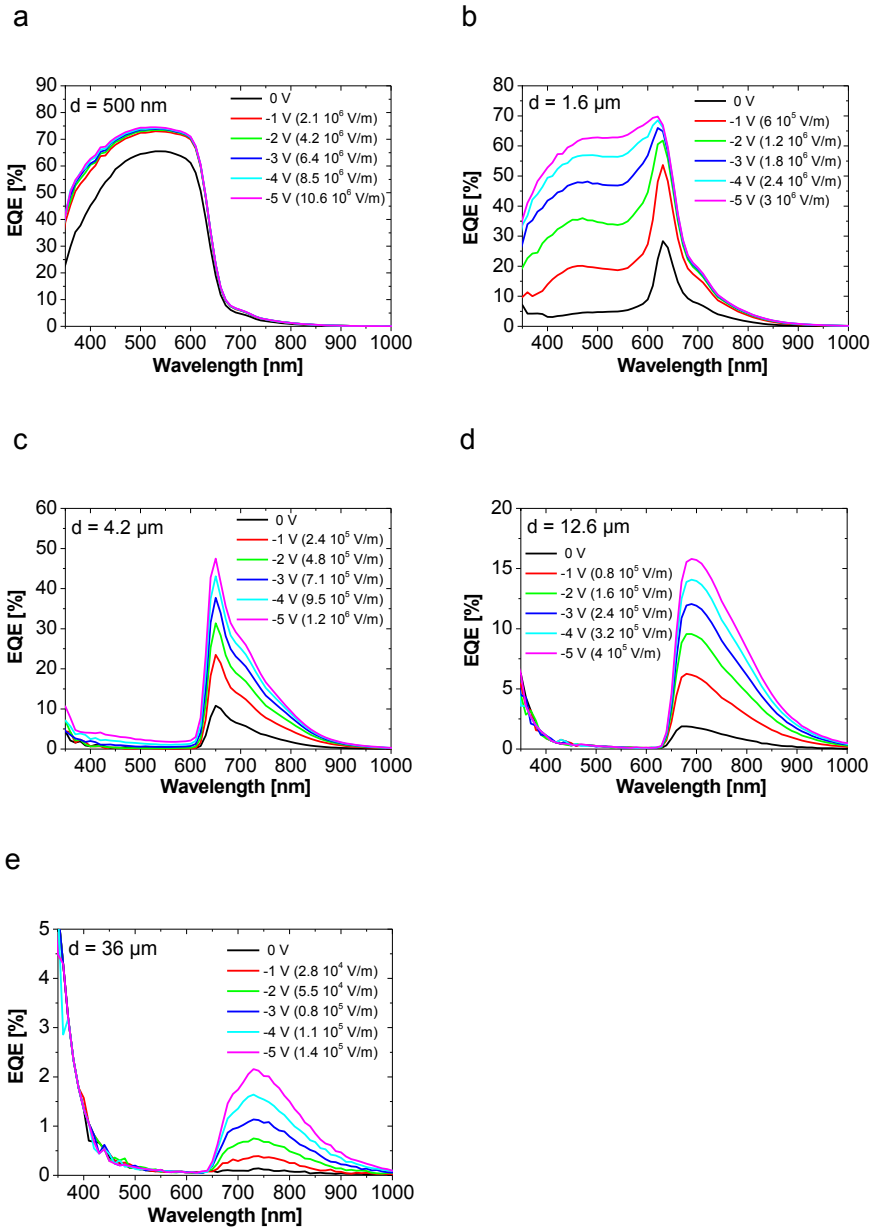

Figure 4.30: OPD EQEs measurement from 0 V to -5 V reverse bias on P3HT:PCBM devices with mean BHJ thickness of a) ~500 nm. b) ~1.6 µm. c) ~4.2 µm. d) ~12.6 µm. e) ~36 µm. OPD internal electric field is also shown.

Contrary to the optical penetration length where the average film thickness is relevant, to compare dark current characteristics of diodes with different thickness, values need to be referred to the minimum spray-coated film thickness (minimum electrodes

distance). In Fig. 4.31 a correlation between the minimum continuous layer thickness vs. mean BHJ thickness is presented with two different linear interpolations.

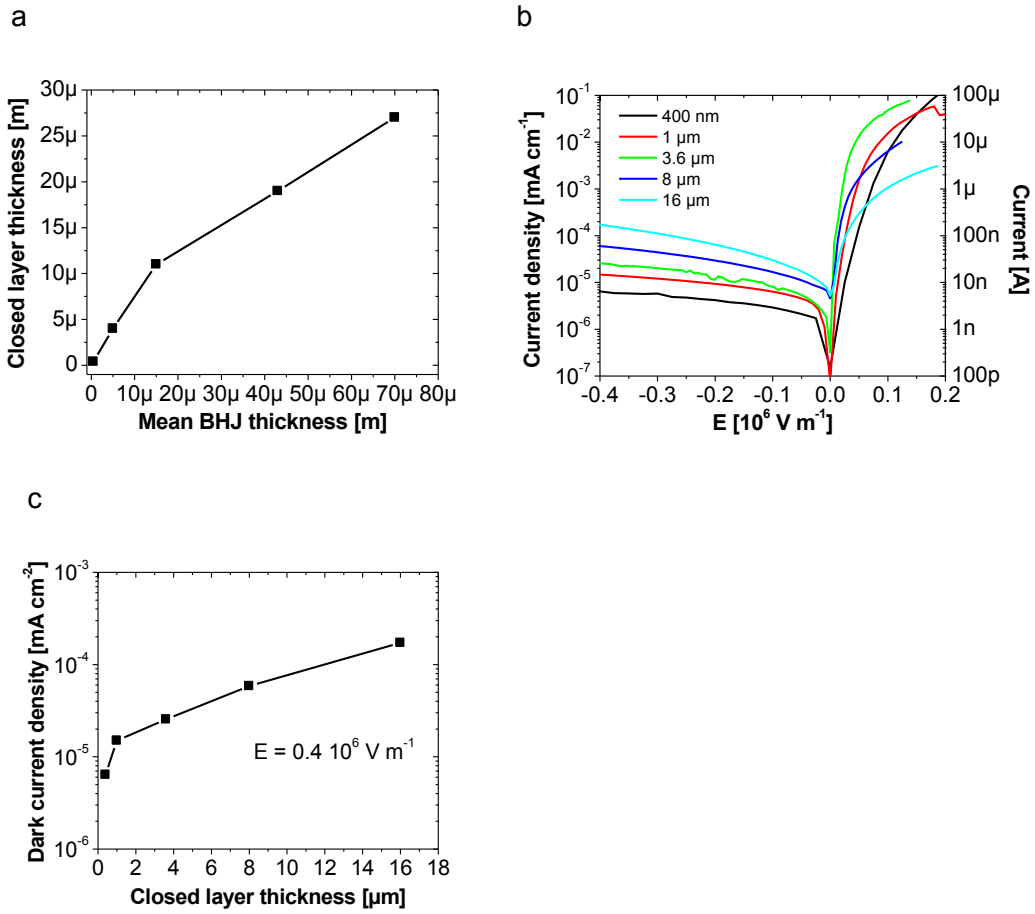

Figure 4.31: P3HT:PCBM closed layer thickness. a) Correlation between close BHJ layer thickness and mean BHJ layer thickness. b) Dark measurements on the diodes as function of the internal electric field with varying closed layer thickness from ~400 nm to ~16 µm. c) Dark current density as function of the closed layer thickness for E = ~0.4 10^6 V m^{-1}.

Difference between mean and closed layer thickness increases increasing BHJ thickness. Result shows that with increasing thickness the average thickness is relevant for dark currents. In Fig. 4.31b the IVs as function of E are plotted for the minimum continuous BHJ layer. The same trend for the dark current densities with the BHJ thickness is observed as discussed for Fig. 4.28d but now the values correspond to the true dark current densities. Finally, it is investigated with post annealing of the thicker OPD (36 µm) how the diode NIR sensitivity is influenced by the BHJ

morphology. Annealing steps of 10 minutes each between 80 °C to 180 °C has been performed (Fig. 4.32a).

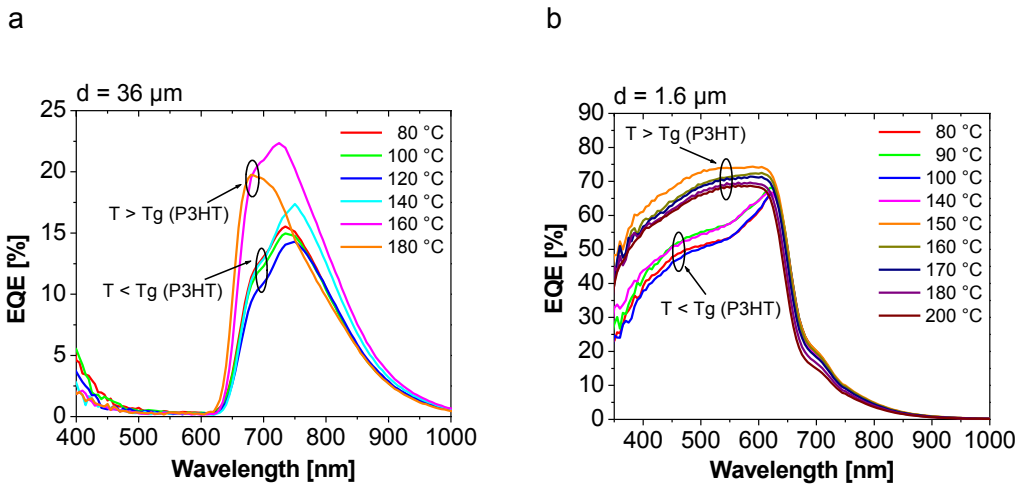

Figure 4.32: Post processing annealing for temperatures ranging from 80 °C to 200 °C on a) 36µm and b) 1.6 µm thick P3HT:PCBM OPDs. Each annealing steps was 10 min.

The temperature dependence shows a weak EQE reduction trend and a small red shift of the EQE peak with increasing temperature up to 120 °C. For temperature higher than the P3HT glass transition temperature (Tg of ~140 °C) [Ngo 2010] the EQE rises. Measurements are in agreement with literature were stability for the PEDOT:PSS up to ~260 °C [Friedel 2009] and for the P3HT and PCBM up to ~200 °C [Ngo 2009] have been reported. Melting point of the P3HT is ~210 °C [Kim 2006] [Klimov 2006]. Note, that within a stack of PEDOT:PSS and BHJ the lowest glass transition temperature is with P3HT [Ngo 2010] [Friedel 2009] [Kim 2006] [Klimov 2006].

It has been already shown that OPD photoresponse can turn better after a post processing thermal annealing. As an example in [Ray 2011] it is reported an organic device with P3HT as absorbing material that after < 40 min annealing step shows an improvement in the current whereas at higher temperatures the current decreases again. Similar result are reported in [Marsh 2010] with the EQE increasing after an annealing step.

Thermal annealing effects has been linked to P3HT reordering and improvement of nanoscale morphology despite the precise mechanism by which it improves charge photogeneration remains unclear [Marsh 2010].

While lateral morphology, such as the grain size and the crystallinity of the donor and acceptor, has been widely focused on, the vertical composition distribution is also an important issue because charges have to be transported vertically to their respective electrodes after they are generated at the donor–acceptor interface of BHJ.
The vertical phase separation in the BHJ is believed to be related to the differences in the surface energy of each component. Since P3HT has a lower surface energy than PCBM, it tends to accumulate at the air surface in order to reduce the overall energy [Bjorstrom 2005] [Heriot 2005] [Xu 2009].
In particular, it has been reported that heating of P3HT:PCBM films to temperatures above the P3HT glass transition temperature facilitates phase separation which then allows the enlarged P3HT domains to crystallize [Beal 2010]. Fig. 4.32b shows the results of the same annealing process performed on the 1.6 µm thin diode. Similarly to the thick diode with 36 µm an increase of the EQE is observed beyond the P3HT glass transition temperature (> 140 °C). The results indicate that the spectral sensitivities of the OPD (visible or NIR bandwidth) is not depending on the morphology of the BHJ. This result is consistent with reported values for drop-casted devices [Chen 2010], which have a different morphology compared to the spray-coated BHJ but show the same spectral properties. Interesting for industrial application is the high stability of the BHJ diodes up to ~200 °C.

4.8 OPDs with PCPDTBT

In this paragraph OPD with PCPDTBT as active material for NIR sensitivity are presented.

To fabricate an OPD with sensitivity in the NIR a small band gap material as absorber can be applied for the BHJ replacing the common visible absorber P3HT (band gap of 1.9–2.0 eV). The rich chemistry of semiconducting polymers offers powerful methods to tune the HOMO and LUMO levels and modify the band gap of the material. A proven strategy to reduce the band gap of an organic π-conjugated material consists of incorporating electron-rich and electron-deficient units in an alternating fashion in a polymer chain. This approach allows synthesizing absorbers with band gaps in the 1.2-1.6 eV range [Roncali 1997] [Zoombelt 2009] [van Mullekom 2001]. Recent progress in

the field of organic photovoltaics report a variety of potential polymers suitable for NIR detections such as poly[2,6-(4,4-bis-(2-ethylhexyl)-4H- cyclopenta[2,1-b;3,4-b']dithiophene)-alt-4,7-(2,1,3-benzothiadiazole)] (PCPDTBT) [Hwang 2007] [Soci 2007] [Mühlbacher 2006], polythieno[3,4-b]thiophene (PTT) [Yao 2007], poly{5,7-bis[3,4-di(2-ethylhexyloxy)2-thienyl]-2,3-diphenyl-thieno[3,4-b]pyrazine} (PBEHTT) [Wienk 2006], poly{5,7-di-2-thienyl-2,3-bis(3,5di(2-ethylhexyloxy)phenyl)-thieno[3,4-b]pyrazine} (PTBEHT) [Wienk 2006] and LBPP-1 [Perzon 2007]. Encouraging results for long wavelength absorption (λ = 800-1000 nm) are obtained with PTBEHT and by LBPP-1 as absorbers in BHJ with diodes showing EQEs of ~18 % [Wienk 2006] and ~10 %, respectively [Perzon 2007]. Furthermore, PCPDTBT and PTT exhibit competitive EQEs of ~35 % [Hwang 2007] [Soci 2007] [Mühlbacher 2006] and ~44 %, respectively [Yao 2007].

Reports have shown that a BHJ composite concept can be equally applied with a low-bandgap semiconducting polymer such as PCPDTBT, since it is generally assumed that a small offset between the LUMO levels of the electron and acceptor materials is required for efficient photoinduced charge transfer [Zoombelt 2008] [Hwang 2007].
With PCPDTBT:PCBM composites electron acceptors seem to be necessary to provide a balanced and efficient charge transport in the films [Morana 2008]. In particular it has been demonstrated that the photocurrent increases by about two orders of magnitude when PCBM is added to PCPDTBT [Soci 2007]. According to [Hwang 2007], the optimum lifetime of photogenerated carriers is observed at the weight ratio of ~1:3. This result is confirmed by solar power conversion efficiency measurements [Mühlbacher 2006].

In Fig. 4.33 normalized transmittance and absorption measurements on PCPDTBT:PCBM films with ratio from 1:1 to 1:3 are presented. Pristine PCPDTBT and PCBM are added as references. PCPDTBT shows two NIR absorption peaks at ~710 nm and ~750 nm and a visible peak at ~415 nm wavelengths in agreement with literature [Hwang 2007] while PCBM has a low absorption in the NIR range. In the PCPDTBT:PCBM blend one dominating peak in the NIR is observed. A small red shift of the peak is also observed with increasing PCBM content [Hwang 2007].

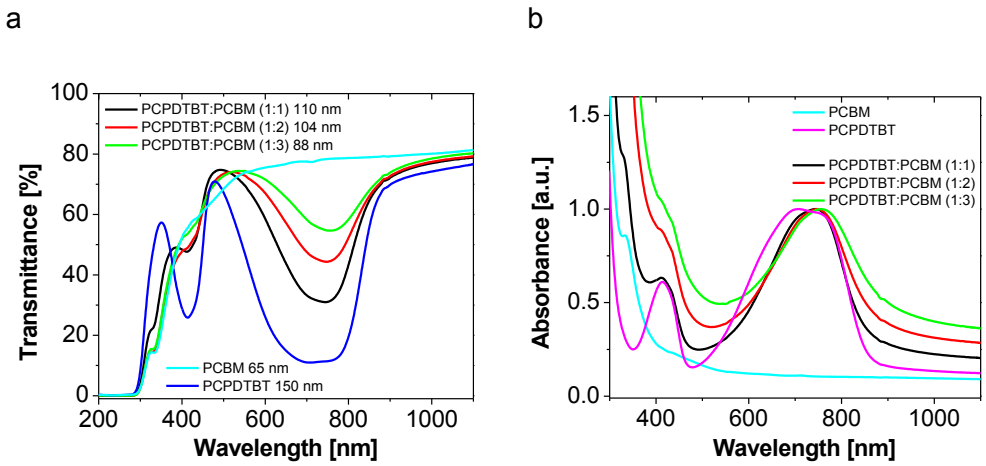

Figure 4.33 a) Transmittance measurements and b) absorbance measurements of spray-coated PCPDTBT:PCBM films with ratios of 1:1, 1:2 and 1:3. P3HT and PCBM are added as reference.

EQE measurements on OPDs with PCPDTBT:PCBM as active material show spectral sensitivity up to ~1000 nm. However, the broad spectral sensitivity covers a broad portion of the visible spectrum, which is not ideal for NIR sensor application. To obtain an OPD with NIR sensitivity only, visible filtering is necessary. Visible wavelength filtering can be achieved with an external low-pass filter in series with the photodiode. However, more intriguing is to integrate the visible wavelength filter as an intrinsic element of the OPD layer stack.

In Fig. 4.34 the influence of the interlayer material on the OPD spectral and the IV characteristic is shown. As a reference Fig. 4.34a shows the IV of an OPD with spin-coated PEDOT:PSS IL (black line) and spray-coated PCPDTBT:PCBM BHJ (weight ratio 1:2.5) in the dark and under polychromatic illumination (> 870 nm). The diode shows favourable properties such as dark current densities of ~10^{-4} mA cm^{-2} at -5 V reverse bias with a rectification ratio at +/- 2 V of ~4 10^5 and a series resistance of ~1 kΩ measured at +2 V. Compared to the reference diode with PEDOT:PSS IL the OPDs with spray-coated P3HT IL match the dark and photocurrent properties though shows a increased serial resistance. A sufficiently thick P3HT IL reduces the dark current as being reported for the P3HT:PCBM blend [Liang 2009] [Oh 2011] which allow to achieve dark current densities of ~10^{-5} mA cm^{-2} at -5 V reverse bias.

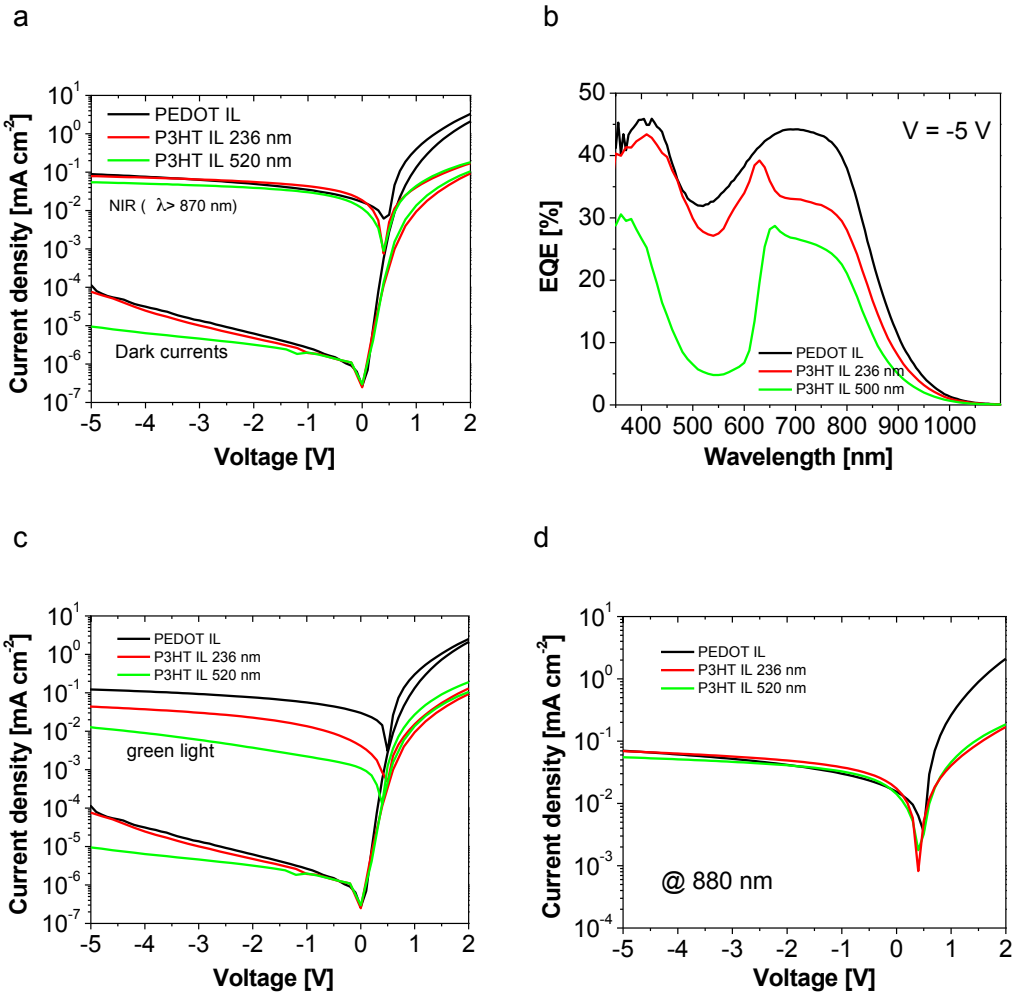

Figure 4.34: Interlayer influence on 1 cm^2 active area spray-coated PCPDTBT:PCBM OPDs. a) IVs in the dark and with NIR light. b) EQEs at -5 V reverse bias. c) IVs in the dark and with green visible light. d) IVs for 880 nm wavelength.

In Fig. 4.34b the spectral characteristic of the diodes are compared. The P3HT IL filters the visible part of the spectra. For the reference diode an EQE maximum at -5 V reverse bias (Fig. 4.34b, black line) of ~44 % is observed at λ = 700 nm while the EQE minimum is for the green wavelength λ=520 nm of ~32 %. The EQE at 520 nm reduces from 32 % (PEDOT:PSS IL) to 28 % (240 nm P3HT IL) and to 5.3 % (520 nm P3HT IL). The EQE minimum shows a red shift from λ=520 nm (PEDOT IL) to λ=540 nm (240 nm P3HT IL) to λ=550 nm wavelength (520 nm P3HT IL). Reduction of the EQE amplitude in the NIR is expected to be related to the total absorber thickness of both BHJ + IL which leads to an increased carrier's recombination. NIR EQE at λ=750

nm drops from ~43 % (PEDOT:PSS IL) to ~32 % (240 nm P3HT IL) to ~25.3 % (520 nm P3HT IL). In Fig. 4.34c diode response for green light (532 nm) is shown while in Fig. 4.34d for a laser with 880 nm wavelength at ~440 µWatt/cm^2 intensity. With P3HT IL good NIR sensitivity is achieved despite some residual sensitivity for wavelengths < 400 nm remains which cannot be filtered by the glass substrate or encapsulation. It is observed a blue-shifting peak at the range from 600 to 700 nm which correlates with the P3HT IL thickness (Fig. 4.28). To understand the reason for the EQE peak of the NIR diodes between 600 to 700 nm PCBM is removed from the BHJ creating a diode with P3HT only. The diode stack is the following: ITO/PEDOT:PSS/P3HT/Al. P3HT is spray-coated from a xylene solution with a weight ratio of 1 % resulting in a mean film thickness of ~1 µm.

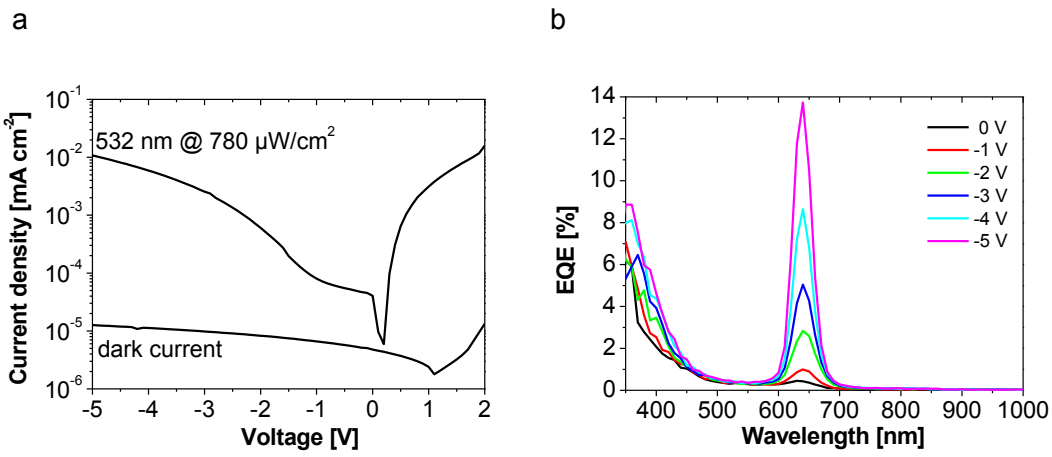

Figure 4.35 Spray-coated P3HT only as OPD. a) IV and b) EQE shown for a 1 cm^2 device.

Fig. 4.35a shows the measured IV characteristic. In the dark the device behaves as an open circuit with a dark current density of ~10^{-5} mA cm^{-2} for both direct and reverse polarizations which is expected for a photoconductor. Under illumination at λ=530 nm the OPD is a weakly rectifying diode because of the photodoping at the Schottky contacts. Most interesting Fig. 4.35b shows the EQE of the diode with only P3HT measured for different voltages ranging from 0 V to -5 V reverse bias. The device shows a sharp EQE peak centered at ~640 nm (photon energy of ~1.93 eV). This peak wavelength corresponds to the maximum of the photoluminescence (PL) spectrum of a pure P3HT film [Piris 2009] [He 2012]. The EQE of the OPD with P3HT IL is therefore

a superposition of the absorption of the independent layers. This result indicates that only a low intermixing occurs in between the IL and the BHJ as a result of the spray-coating process. The EQE in Fig. 4.34b can be interpreted as a superposition of the EQE of both the BHJ and the P3HT IL. The red shift of the EQE peak has been discussed in Figure 4.28.

4.9 OPDs current drift

In this paragraph OPD dark current drift vs. time is presented.

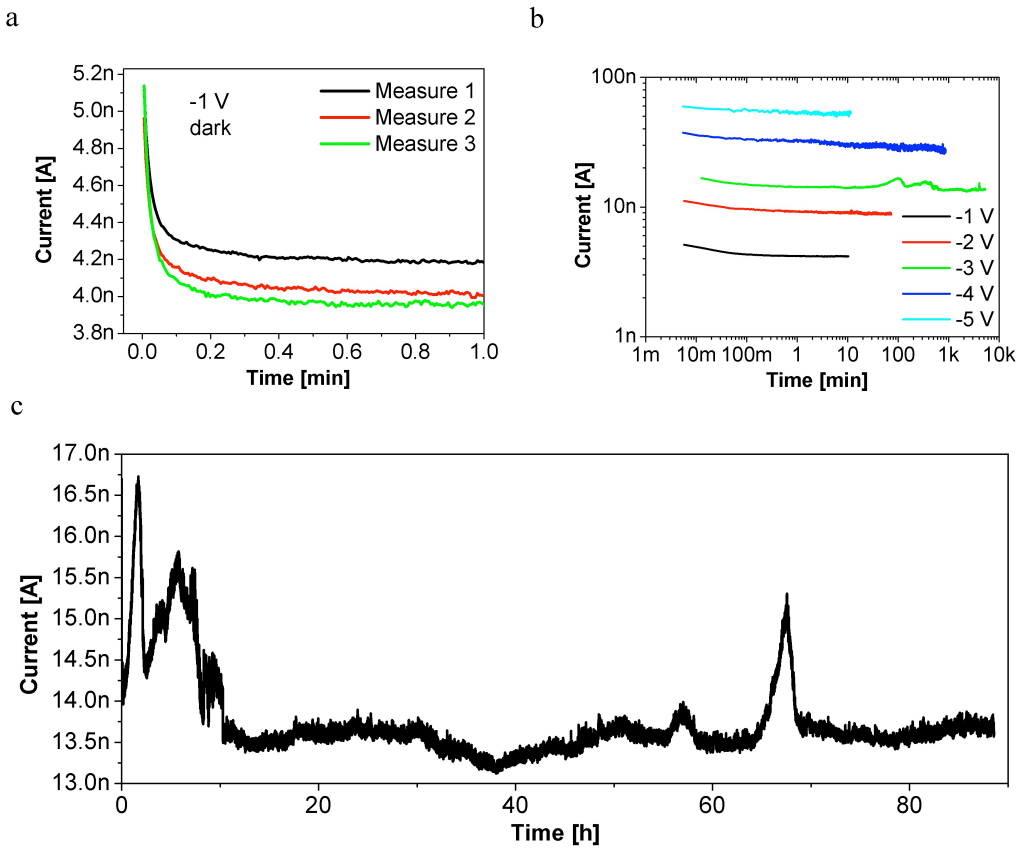

Figure 4.36. a) Current-drift reproducibility. b) Dark current vs. time with varying DC reverse biases. c) Long time stabilization.

In general when the OPD is DC reverse biased an exponential dark current reduction vs. time is observed. As an example Fig. 4.36 shows transient measurements in dark

performed on a 1 cm^2 OPD reverse biased at -1 V. Transient is measured 3 times. Between each measurement the OPD is disconnected from the SMU and kept without polarization for 10 minutes. Transient plots do not overlap and a trend can be identified. Despite the absolute value of the dark current changes with a different plateau level for each measure, the OPD time constant is preserved. Reasons for this behaviour can be identified in trap states, OPD capacitance and OPD degradation.

In Fig. 4.36b OPD dark currents with varying reverse bias from -1 V to -5 V are presented. Independently of the applied bias, an almost exponential dark current reduction with time is observed. OPD noise seems to increase with the applied bias.

Finally in Fig. 4.36c a long time stabilization plot is shown. Diode is DC reverse biased at -3 V and kept in contact to a Peltier element (25 °C) for about 3 days in dark condition. An almost stable signal vs. time is observed. For comparison Fig. 4.37a shows a long time dark current stabilization measurement (~3 days long) on a 1 cm^2 OPD at -5 V reverse bias with no Peltier element used. Dark current do not stabilize and follows the environment temperature variation. In particular during the day it is recorded a high dark current value and in the night, when the temperature reduces, the dark current drops as it is evident comparing the dark current oscillation with the Erlangen temperature variations (inset in Fig. 4.37). Again an exponential current reduction with time can be identified.

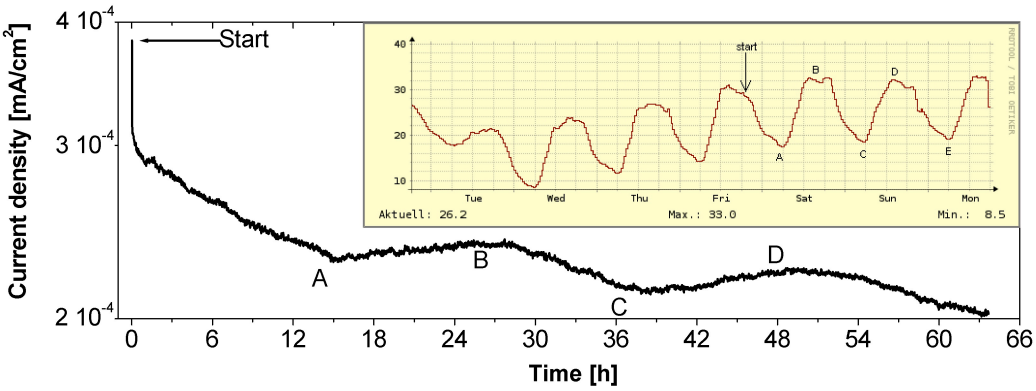

Figure 4.37. Long time OPD dark current stabilization. Diode is DC reverse biased at -5 V. Inset shows the mean Erlangen temperature [Erlangen Temp] fluctuation between Friday 9 July 2010 and the next Monday.

4.10 Effect of the temperature on the OPDs

In this paragraph effect of the temperature on the OPDs is investigated.

Contrary to metals, near room temperature, the electrical conductivity of conducting polymers increases with increasing temperature. Very recently Girtan et al. [Girtan 2013] reported a study on the resistivity of P3HT and P3HT:PCBM films with varying the temperature. Electrical resistivity from ~20 °C to ~100 °C for a P3HT and a P3HT:PCBM (1:0.8 wt.) films in dark and with white light illumination are shown in Fig. 4.38. Results indicate that adding PCBM to the P3HT results in a more conductive layer.

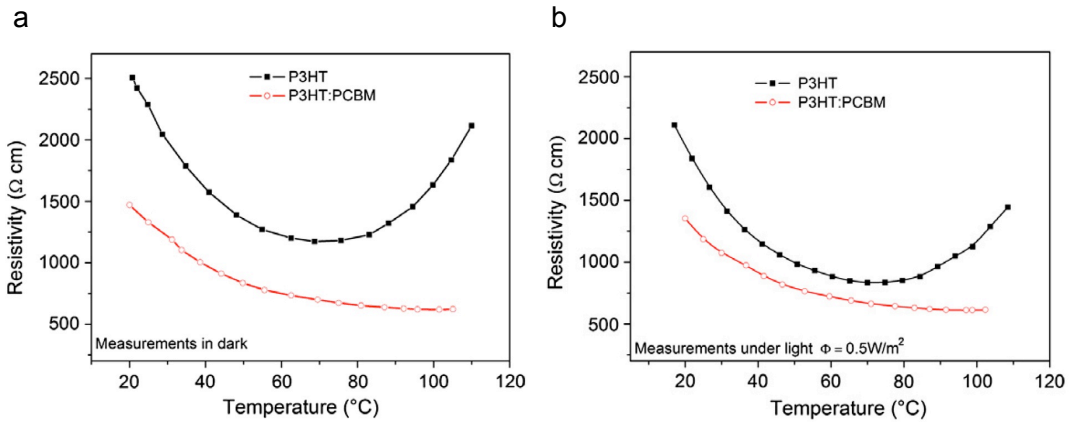

Figure 4.38. a) The electrical resistivity in function of temperature, in a planar geometry, in dark for two thin films: P3HT and P3HT:PCBM, having the same thickness (190 nm). b) The electrical resistivity in function of temperature, in a planar geometry, under illumination (white light Φ = 0.5 W/m^2) of two thin films having the same thickness (190 nm) of P3HT and P3HT:PCBM respectively [Girtan 2013].

The P3HT film shows a minimum resistivity for ~70 °C while with increasing the temperature resistivity increases. In strong contrast the P3HT:PCBM layer shows a resistivity that decreases monotonically with increasing temperature. The decrease of the resistivity is more significant when samples are irradiated indicating a photon activated mechanism in addition to the thermal activated mechanism. The phenomenon is reversible and reproducible.

Effect of the BHJ resistivity variation with temperature on an OPD is than investigated. In Fig. 4.39a OPD current densities with varying temperature from ~5 °C to to ~90 °C

are presented. The OPD is kept 10 min at the respective temperature before starting each measurement. Dark current at -5 V reverse bias rises linearly from ~1 10^{-5} mA/cm^2 at 10 °C to ~2.1 10^{-4} mA/cm^2 at 90 °C in agreement with [Girtan 2013] were a monotonically increases of the current with increasing the temperature was observed. Under green light illumination the photocurrent at -5 V reverse bias varies from ~0.25 mA/cm^2 at 10 °C to ~0.26 mA/cm^2 at 90 °C. The forward and backward current density variation with temperature is shown in Fig. 4.39b for -3 V reverse bias. With ramping the temperature up and down an exponential correlation between temperature and dark current is observed.

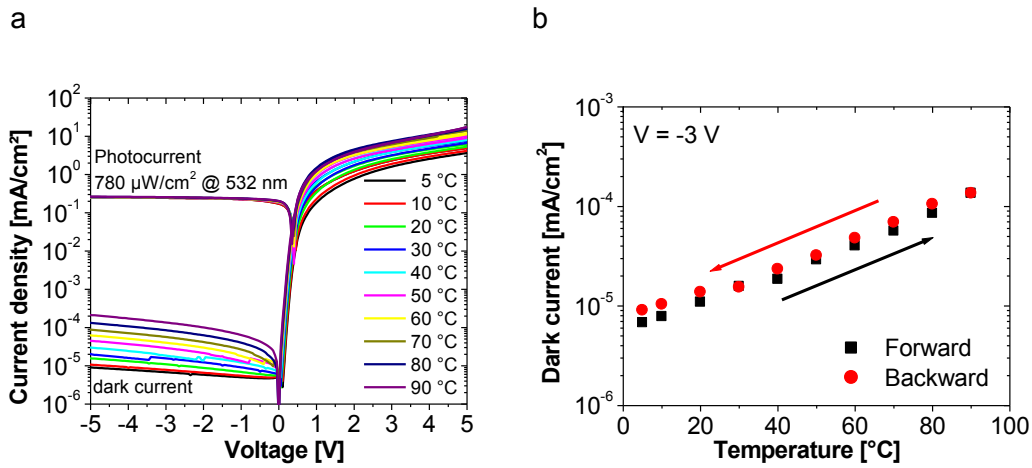

Figure 4.39. a) OPD current density measured at varying temperatures from 5 °C to 90 °C. b) Dark current density vs. temperature for forward and backward measurements. Measurements between 5 °C to 90 °C cycling.

5. Organic OPDs as X-ray detectors

X-ray is an electromagnetic radiation characterized by a shorter wavelength than visible light but longer than high energy gamma rays, in the range from about 10 nm (3 10^{16} Hz) to 0.01 nm (3 10^{19} Hz), produced by electron transitions between energy levels deep in the atom, or after a deceleration of a particle beam when penetrating a material. Discovered at the end of the 19th century, were called X due to their mysterious nature.

X-ray are usually generated by an X-ray tube, consisting of two metallic electrodes, the anode (positive) and the cathode (negative) operating in vacuum. The cathode is passed through a strong current that heats the filament and causes the release of electrons for thermoionic emission. Generated electrons are accelerated toward the anode by a high electromagnetic field (several kV) and impact a target material (tungsten, molybdenum, palladium, silver or other material). Interaction between electrons and target atoms generates high amount o energy, some of that is refracted off of the target in the form of high energy photons, or X-rays, forming the X-ray beam.

Typically, only 1% electron's energy is converted into X-rays photons, while the rest is converted into heat that can damage the anode. To avoid overheating X-ray tube has a cooling system to decrease the temperature. Modern tubes use a rotating anode to distribute the energy on a big area.

5.1 X-ray photons generation

Electrons loose energy through two processes, by deceleration through the bulk of the material or by collision with a core electron in the material atoms.

In a X-ray tube the electrons emitted by the cathode are accelerated towards the metal target anode by an accelerating voltage. Electrons, that have a high energy, interact with the atoms in the metal target. Sometimes electrons come very close to a nucleus

in the target and are deviated by the electromagnetic interaction. Electrons decelerate and loose energy that is emitted as X-ray photons (Fig. 5.1a). The energy of the emitted photons can take any value up to a maximum corresponding to the energy of the incident electron. Deflected electrons can produces additional X-ray photon, for example by interacting with a new atom. This process generates a polychromatic radiation (continuous distribution of X-rays) and is knows as bremsstrahlung (braking radiation). The resulting continuous X-ray spectrum covers a wide range of wavelengths, with a lower limit corresponding to the maximum energy of electrons ejected by the cathode.

In the electron-atom interactions (Fig. 5.1b), oncoming electrons from the X-ray tube anode interact with a core electrons, that are ejected from the shell generating a hole, because electron originating from anode continues on. Orbital electrons of higher energy levels fill the void in the inner shell and the difference in energy is emitted as a monochromatic (monoenergetic) X-ray photon. Again, ejected electrons can interact with new atoms to generate additional X-ray photons. This process is called “characteristic radiation”.

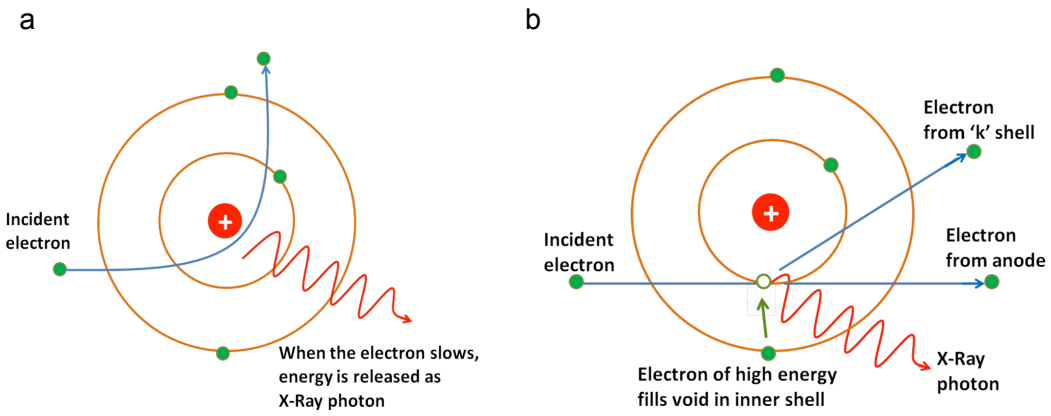

Figure 5.1: Representation of X-ray generation process: a) Bremsstrahlung and b) Electron-atom interaction.

The wavelength of the emitted X-rays photons depend on the energy difference between the electrons involved in the transition, and thus by the orbital structure of atoms involved. The characteristic X radiation emitted by an unknown material give

precise information of the atomic structure can be used to determine the chemical nature of the sample.

X-ray photons have different names as function of the energy. For example, see Fig. 5.2, X-rays produced by transitions from the n=2 to n=1 levels are called K-alpha X-rays, and those for the n=3 to n =1 transition are called K-beta X-rays. Transitions to the n=2 or L-shell are designated as L X-rays (n=3 to n=2 is L-alpha, n=4 to n=2 is L-beta).

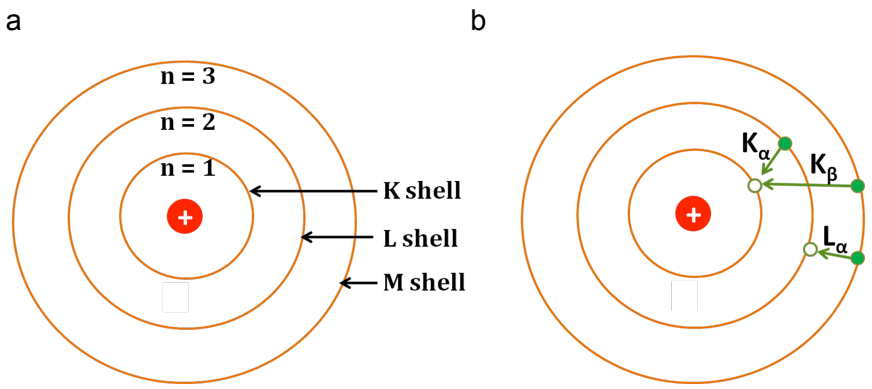

Figure 5.2: a) Atomic levels involved in X-ray emission and b) transitions from different shells.

Finally in Fig. 5.3 a generic X-ray energy spectrum generated by an X-ray tube is shown. The continuous curve of the spectrum is due to bremsstrahlung while sharp peaks are related to characteristic radiation lines.

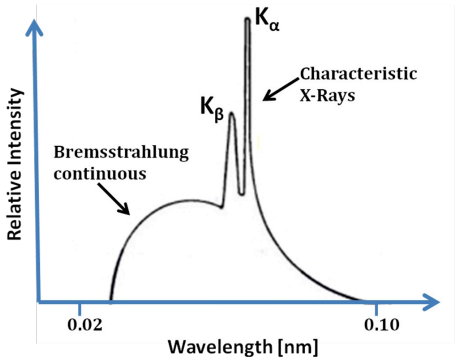

Figure 5.3 Exemplary X-ray spectrum generated by an X-ray tube.

X-ray detection

X-ray detection can be divided in 2 classes, a direct technique (direct-conversion detectors) or an indirect technique (indirect-conversion detectors) for converting X-rays into an electric charge.

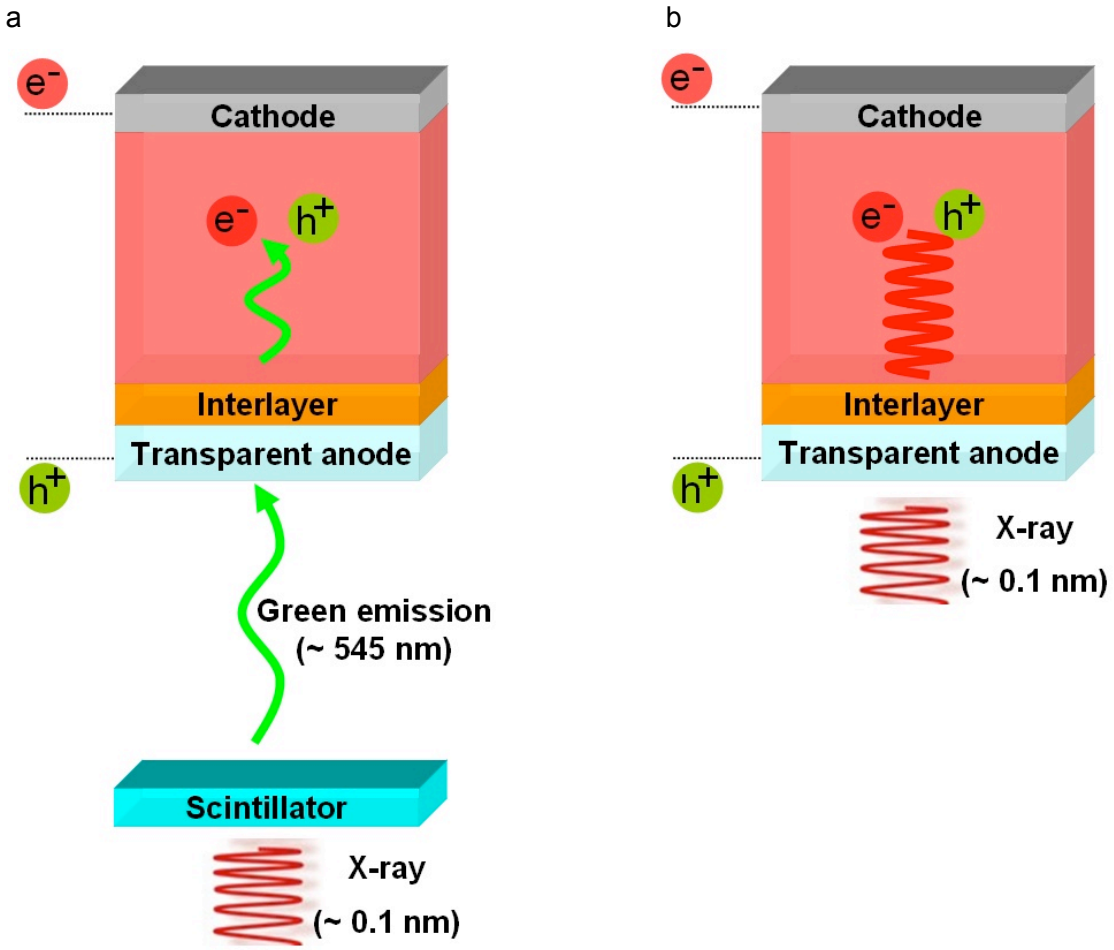

Figure 5.4: X-ray photons detection. a) indirect and b) direct X-ray conversion.

In indirect-conversion detectors (Fig. 5.4a) the X-rays are first converted to light via a scintillating phosphor, such as Gd_2O_2S:Tb or GOS (which absorbs the incident X-rays), and then the light emitted from the scintillator is detected by the photodiode. Usually the photodetector has absorption spectra that match the emission spectra of the scintillator layer.

Direct-conversion detectors (Fig. 5.4b) are capable to convert the incoming X-ray photons into an electric charge without the need of a scintillator. In this case an X-ray absorbing material is used as the principal detecting element to convert the X-ray photons directly to collectable charge carries, which represent the diode signal. The photons that interact with the absorbing material generate electron-hole pairs that are separated by an internal electric field. The electrons and holes are than extracted at the electrodes to generate an electrical signal in the form of an increased semiconductor current proportional to the incident X-ray dose. Usually direct-conversion detectors have reduced detection efficiency compared to solutions with scintillators.

The most common used material to fabricate direct conversion X-ray detectors is the amorphous Selenium (a-Se).

5.2 Gd_2O_2S:Tb Scintillator

A scintillator is a material that converts incident X-ray photons in visible light. An ideal scintillator should presents various properties, such as high light output, high X-ray absorption efficiency, low afterglow, low radiation damage, high uniformity, good chemical stability and degree of safety and spectral match to the sensitivity of the photodiode. The most common used scintillator materials are CsI:Tl, Gd_2O_2S:Pr,Eu,Tb, $Y_3Al_5O_{12}$:Yb,Ho,Eu,Cr, and Lu_2SiO_5:Ce.

Terbium-doped gadolinium oxysulfide (Gd_2O_2S:Tb, simply GOS), one of the rare earth oxysulfide group of phosphors, is one of the most promising scintillation material due to the bring green emission exhibited after excitation, the high stopping power to X-ray radiation resulted from its high density of ~7.44 g cm^{-3}, the high Z number of 64 of the Gd, and its high intrinsic conversion efficiency (12 - 25 %) of the exciting radiation.

Terbium-doped gadolinium oxysulfide is an inorganic material commercially available as powder composed by particle spheres with diameter ranging from ~1 µm to ~5 µm. Here, different techniques to create a GOS layer are presented. First GOS particles with diameter of ~2.5 µm are dispersed in isopropanol (5 mg/ml) and spray-coated at

room temperature on a glass substrate. Fig. 5.5 shows the resulting layer after 1, 2, 3 and 5 spray-coating steps. GOS particles show a tendency to aggregation

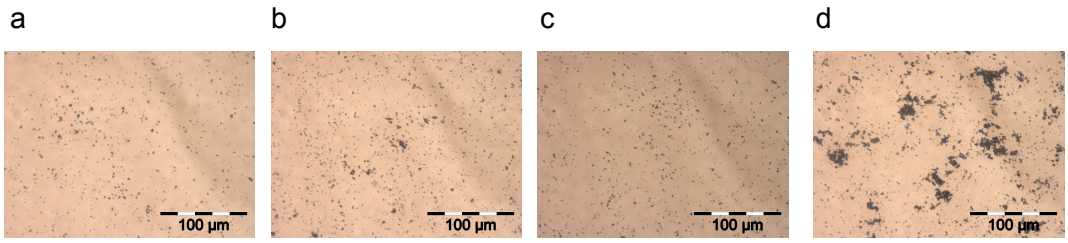

Figure 5.5: Optical pictures of GOS particles spray-coated on glass a) 1, b) 2, c) 3 and d) 5 times.

Second, GOS particles (~4 µm diameter) are dispersed in isopropanol (14 mg/ml) and doctor-bladed at room temperature on a glass substrate.

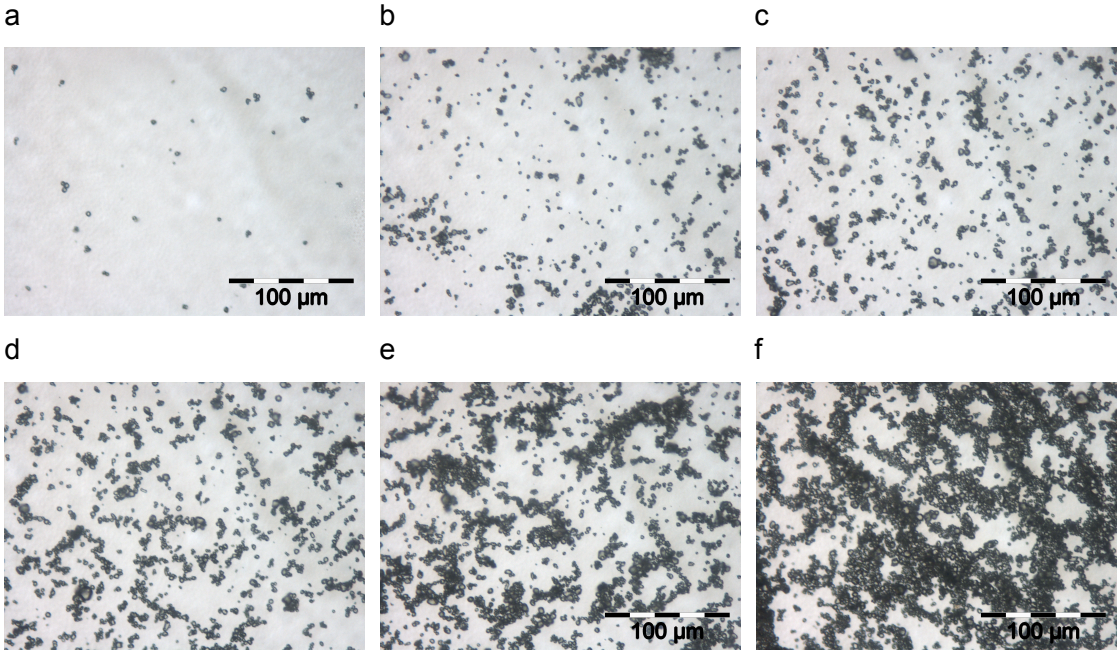

Figure 5.6: Optical view of GOS particles doctor-bladed on glass a) 1, b) 3, c) 6, d) 10, e) 15 and f) 30 times.

Fig. 5.6 shows the resulting layer after 1, 3, 6, 19, 15 and 30 doctor-blading steps. Again a particle tendency to form agglomerations can be identified.

Third, particles are mixed with epoxy glue with the aim to find a fast and easy way to deposit a thick and uniform layer of GOS on a glass substrate. GOS particles (~4 μm diameter) are mixed with standard epoxy glue in a concentration of ~ 25 %. Solution is stirred at 80 °C for some minutes to reduce viscosity and some drops deposited on a glass substrate. Samples are than encapsulated with a thin glass slide.

Fig. 5.7 shows pictures of the resulting layer with the microscope in focus on different planes of the layer. Film is ~35 μm thick.

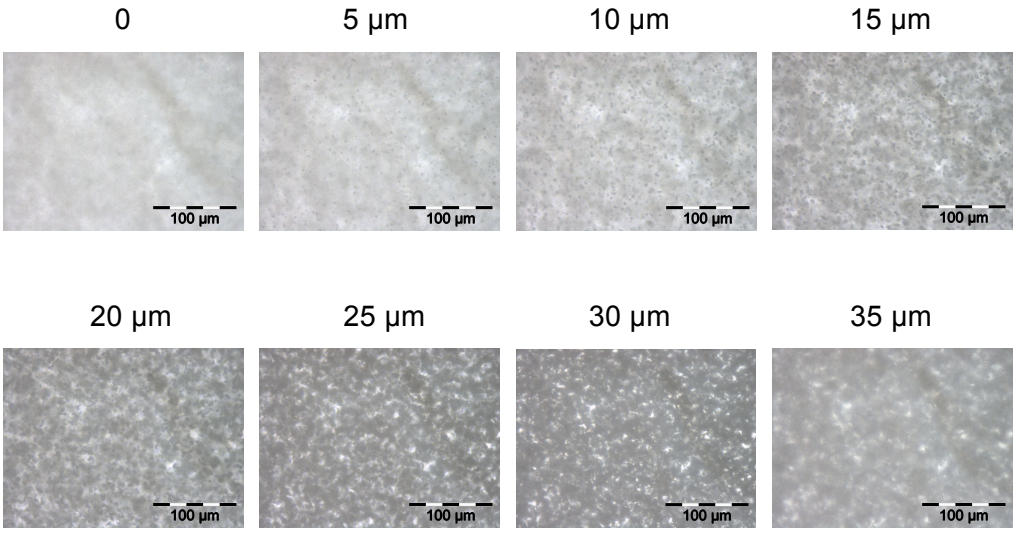

Figure 5.7: Optical view of GOS particles mixed with epoxy glue and deposited on a transparent glass substrate.

Finally, GOS particles can be sedimentated onto a glass substrate. Sedimentation is a deposition process by gravity where the GOS particles, dispersed in isopropanol, gradually precipitate to the bottom of the container, Fig. 5.8a. This is probably the easiest way to fabricate the film, compared to the previously deposition techniques. With the sedimentation technique it is possible to create a uniform GOS film in a short time with full control of the final layer thickness.

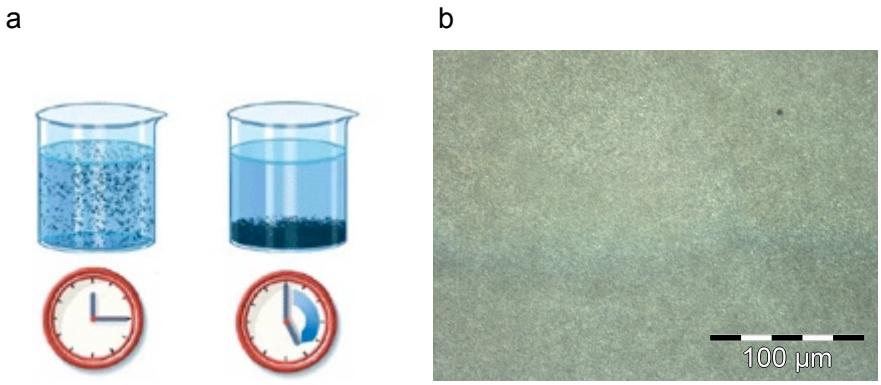

Figure 5.8: a) GOS sedimentation process. b) Optical view of sedimented GOS particles on a transparent glass substrate.

Due to the spherical shape of the GOS particles, the sedimentated material does not create a compact layer but between particles some voids remain. A fill factor of ~33 % in the fabricated layer has been observed. It can be caused by the size of the sphere not exactly equal, by the sedimentation process too fast that do not give enough time to the spheres to organize, or, more realistically, by the tendency of the GOS particles to create amorphous aggregations.

5.3 Silicon photodiode X-ray results

In this paragraph X-ray measurements on a reference silicon photodiode are shown.

A crystal silicon (c-Si) photodiode from Hamamatsu (S1337-1010BR) with 1 cm^2 active area is here characterized with light and X-ray excitations as reference photodetector.

The c-Si diode shows a dark current density < 2 10^{-7} mA cm^2 at -5 V reverse bias (Fig. 5.9a) and a spectral sensitivity up to ~1 µm wavelength independent from the applied reverse bias (Fig. 5.9b). The real value of the dark current is probably even lower because seems limited by the used Keithley SMU.

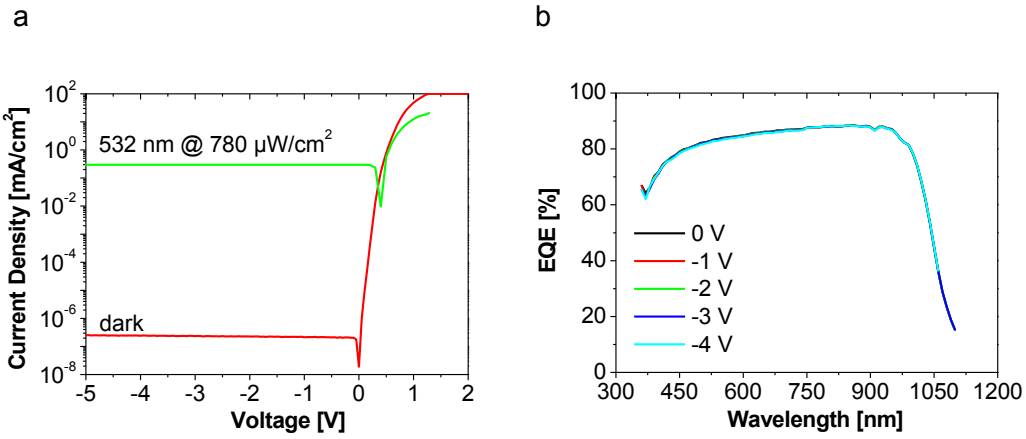

Figure 5.9: Si photodiode. a) IV and b) EQE.

X-ray pulses at 70 kV and 2 seconds length with dose rates ranging from 90 µGy/s to 3 µGy/s are than applied to the diode, Fig. 5.10. Independently from the applied reverse bias the diode shows comparable photocurrent.

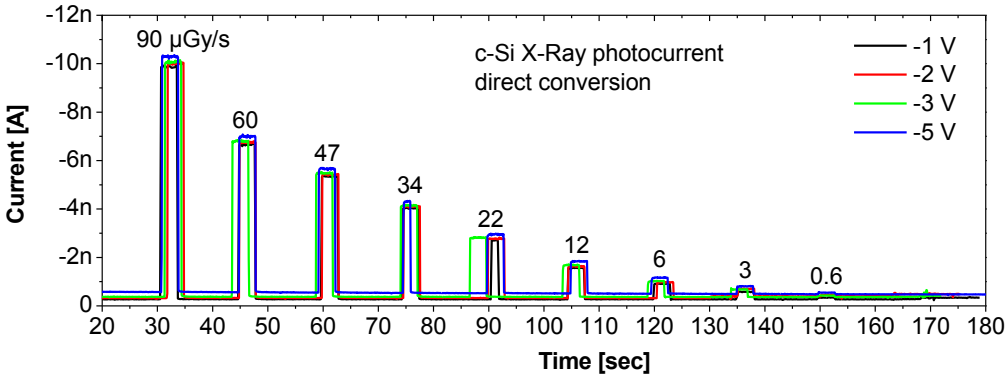

Figure 5.10: Si PD response to X-ray pulses at 70 kV energy with dose rates from 90 µGy/s to 3 µGy/s with varying the reverse bias.

Influence of the scintillator layer to the device photocurrent by X-ray photons is summarized in Fig. 5.11a. With 8 µm GOS scintillator no increase in the photoresponse can be seen compared to the direct-conversion photocurrent. With a Kodak lanex scintillator, that generates higher green light intensity than the thin GOS layer, a photocurrent increase is observed. Result indicates that due to the direct X-ray

conversion capability of the c-Si diode, the diode is not able to detect the low green emission of the thin GOS scintillator.

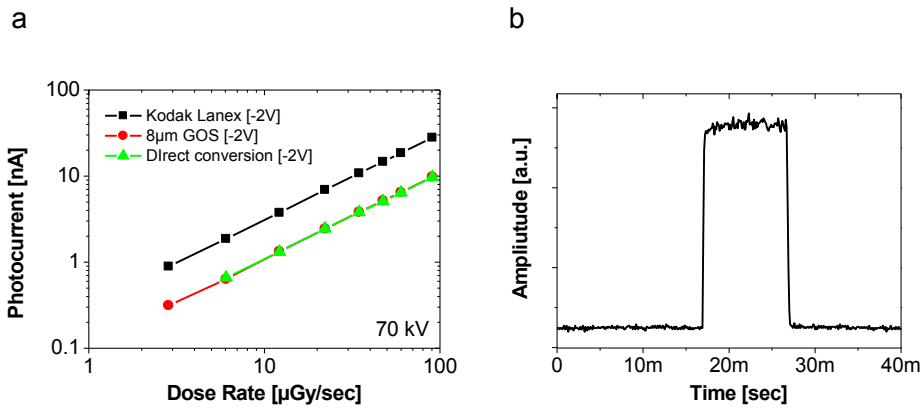

Figure 5.11: a) c-Si response with varying the dose rates. Comparing Si direct conversion and Si coupled with 8 µm GOS layer scintillator and Kodak Lanex scintillator. b) c-Si response to a 10 ms X-ray pulse at 70 kV, 420 µGy/s (direct conversion).

In Fig. 5.11b c-Si response to a 10 ms X-ray pulse at 70 kV and ~420 µGy/s dose rates is shown. Note that the dark current shows no drift and diode noise can be neglected. Photocurrent by direct conversion is ~10 nA for 90 µGy/s dose rates at low bias with a rise and fall times < 1 ms.

5.4 OPD X-ray results

In this paragraph indirect X-ray conversion with organic photodiodes is presented. In this configuration the organic photodiode with P3HT:PCBM as active material is coupled with an inorganic thin GOS scintillator layer. The scintillator absorbs the X-ray photons and generates a green light that is than absorbed and converted in charges by the organic photodiode.

Fig. 5.12 shows exemplary X-ray measurements performed on a 1 cm^2 OPD with P3HT:PCBM as active layer (stack: ITO/PEDOT:PSS/BHJ/Al) coupled with GOS scintillators with different thickness (from 8 µm to 28 µm) and irradiated with 2 sec X-

ray pulses with 70 kV energy and dose rates ranging from 90 µGy/s to 3 µGy/s. Diode is reverse biased at -3 V. This is the reference organic diode since PEDOT:PSS is the most common used IL for OPD and organic solar cells fabrication.

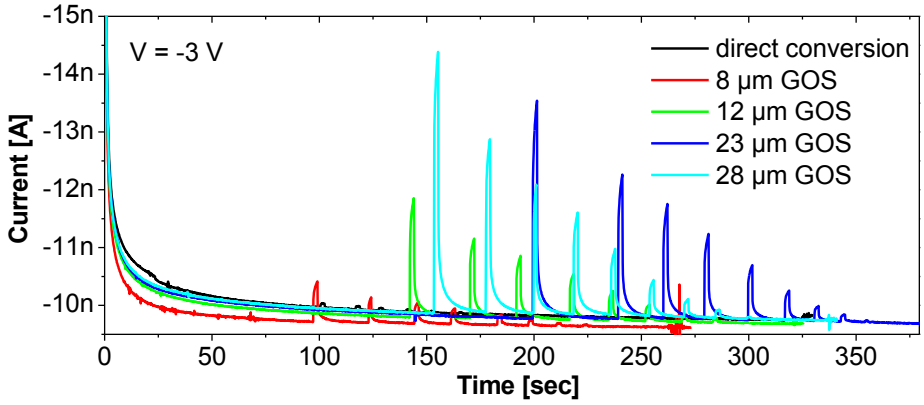

Figure 5.12: Photoresponse to X-ray photons at 70 kV energy of an OPD with PEDOT:PSS IL reverse biased at -3 V and coupled with GOS scintillator with thickness from 8 to 28 µm. X-ray dose rates are in the order 90, 60, 47, 35, 22, 12, 6 and 3 µGy/sec. X-Ray pulses length is 2 seconds.

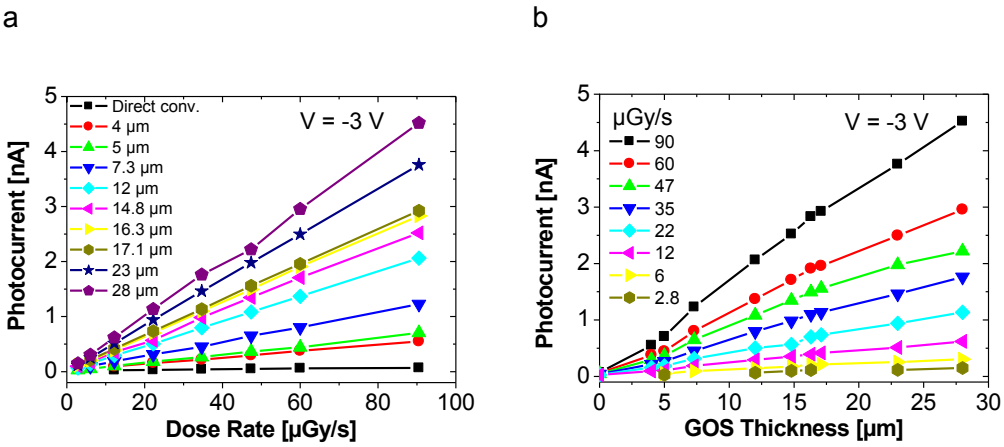

Figure 5.13: a) OPD photocurrent vs. X-ray dose rates for different GOS layer thickness. b) OPD photocurrent vs. scintillator GOS thickness with varying the dose rates. Measurements at -3 V reverse bias.

Results show that photocurrent rises with increasing the GOS layer thickness. Measured photocurrent values vs. X-ray dose rates for different GOS layer thickness

are presented in Fig. 5.13a while measured photocurrent values vs. GOS thickness with varying the dose rates are presented in Fig. 5.13b.

A linear dependence between OPD photocurrent and X-ray dose rates is identified.
A linear dependence between OPD photocurrent and GOS layer thickness is also identified.

No variation in the OPD time constant can be observed by varying the X-ray dose rates up to 90 µGy/s (Fig. 5.14a-b) or the GOS layer up to 28 µm (Fig. 5.14c-d)

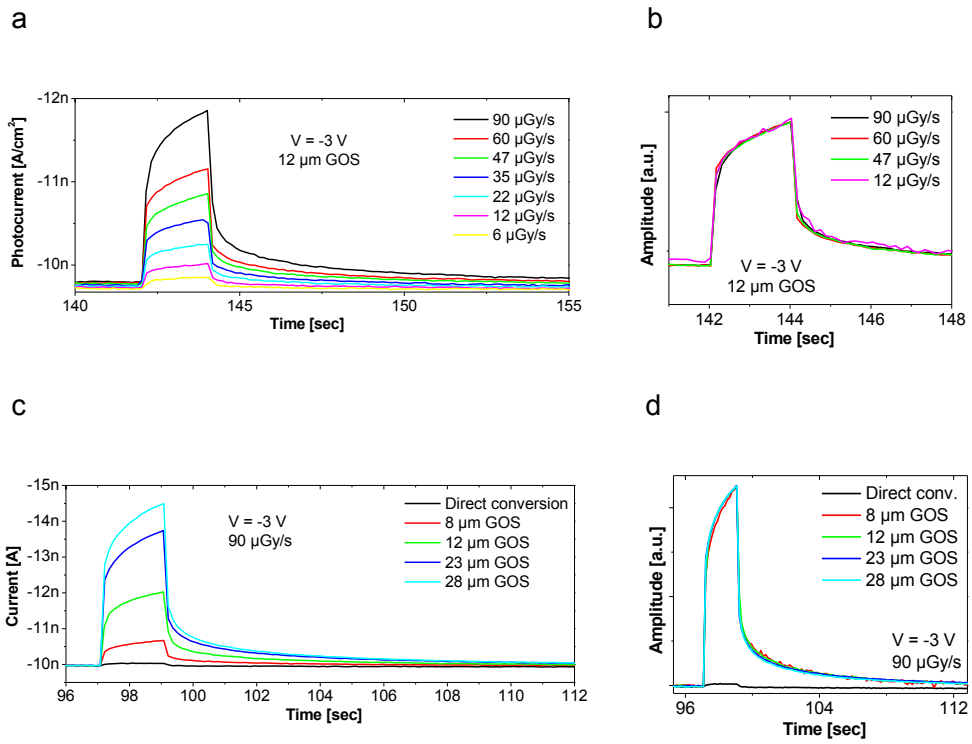

Figure 5.14. a) OPD response overlaps to X-ray photons at 70 kV with varying the dose rates. OPD is coupled with a 12 µm GOS layer. b) Normalized photoresponse with varying dose rates. c) OPD response overlap to X-ray photons at 70 kV and dose rates of 90 µGy/s with varying the GOS thickness. d) normalized photoresponse with varying GOS thickness. Diode is reverse biased at -3 V.

The OPD with PEDOT:PSS IL shows a long transient, in agreement with the light measurements were a cut-off frequency in the Hz range at low light intensities is observed [Arca 2013]. Similar results are obtained with the OPD with 2 ILs were the

first IL is the PEDOT:PSS. As an example Fig. 5.16 shows X-ray photoresponse of an OPD with stack ITO/PEDOT:PSS/P3HT/BHJ/Al. Again a long transient of a few seconds is identified. With the use of 2 ILs no improvements in the dynamic response under X-ray excitation are observed, in agreement with the light experiments.

Neglecting the BHJ direct conversion of the X-ray photons, so assuming all the photocurrent is the result of the absorption of the green light generated by the scintillator, the equivalent optical power density generated by the GOS layer can be calculated by:

$$P_{opt} = \frac{h\nu}{q}\frac{I_{ph}}{EQE} \tag{5.1}$$

with h Plank constant, q elementary charge and I_{PH} OPD photocurrent.

In Fig. 5.15 the GOS optical power intensity is shown for the 1cm² OPD presented in Fig. 5.13 reversed biased at -3 V and assuming λ = 530 nm and EQE = 70 % . A relatively thick 28 µm GOS layer irradiated with X-ray photons at 70 kV with dose rates < 10 µGy/s emits in the low nW/cm^2 range.

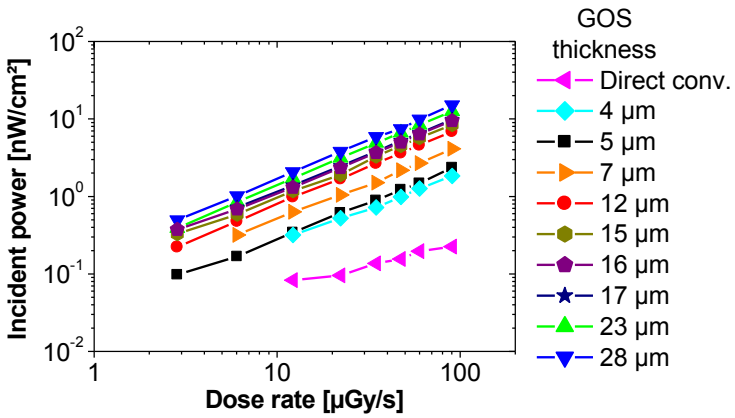

Figure 5.15: Equivalent light power densities generated by the GOS layer with varying the GOS thickness and the X-ray dose rate.

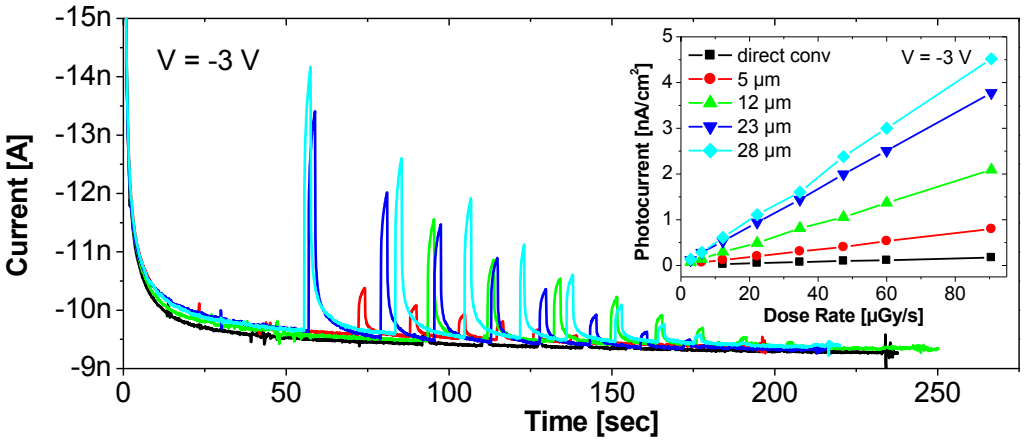

Figure 5.16: Photoresponse to X-ray photons at 70 kV energy of an OPD with PEDOT:PSS and P3HT as ILs reverse biased at -3 V. Inset shows the photocurrent vs. dose rates with varying the scintillator thickness. X-ray dose rates are in the order 90, 60, 47, 35, 22, 12, 6 and 3 µGy/sec. X-ray pulses length is 2 seconds.

Finally, influence of the IL in the OPD response time is presented. OPDs with different stacks are coupled with a layer of GOS to the bottom of the OPD substrate with transparent epoxy glue. The green fluorescence emission at 545 nm of the GOS film matches the highest spectral sensitivity of the photodiodes. GOS thin film thicknesses including voids are ~12 µm thick (~4 µm absolute GOS thickness), which is sufficiently thick for X-ray conversion with fluorescence emission intensities in the nW cm^{-2} regime.

In agreement with the light experiments, IL influences the dynamic response of the OPDs under X-ray excitations. Fast dynamic response is observed on OPDs with P3HT and SAM as ILs while PEDOT:PSS IL and devices without IL show the longest transient. Photocurrents vs. dose rates for the 7 different investigated stacks are summarized in Fig. 5.17h.

The highest photocurrent is observed on the devices with PEDOT:PSS IL and Ca/Ag as cathode (stack g). The lowest photocurrent is measured on the OPD with P3HT IL (stack a and d) due to the IL absorption of the light that reduces the quantum efficiency. Thin layers show higher photocurrent than thick layers (stacks e and f). Devices with SAM IL (stack e and f) show higher sensitivity than devices with PEDOT:PSS IL (stack b) or without IL (stack c).

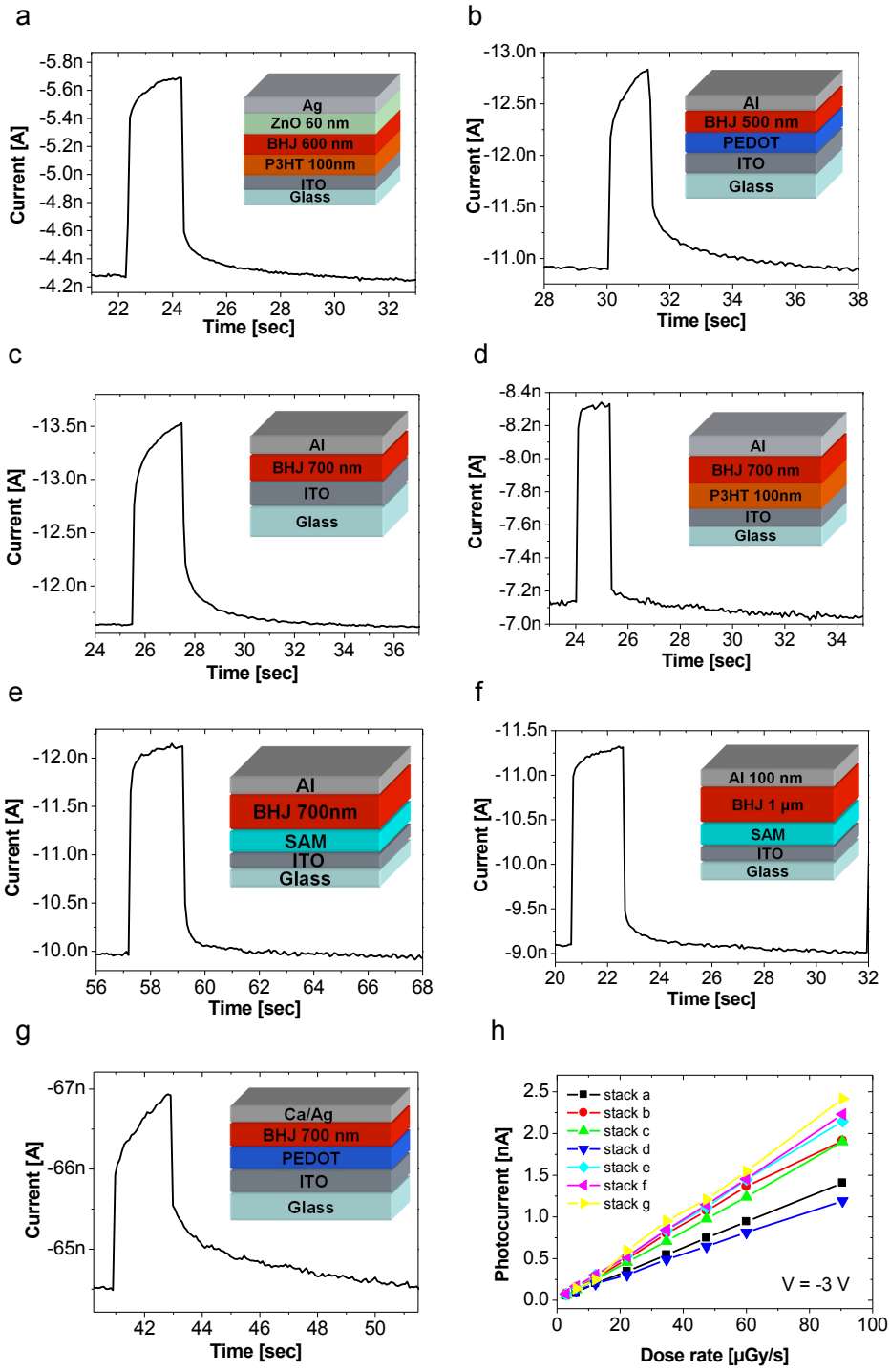

Figure 5.17: Photoresponse of 1 cm^2 OPDs with different stacks to a single X-ray pulse at 70 kV with dose rate of ~90 µGy/s. Diodes are reverse biased at -3 V and coupled with 12 µm thick GOS layer. Insets show the layer stack of the OPDs. h) Photocurrent vs. dose rates at -3 V reverse bias for the stacks from a to g in the same Figure.

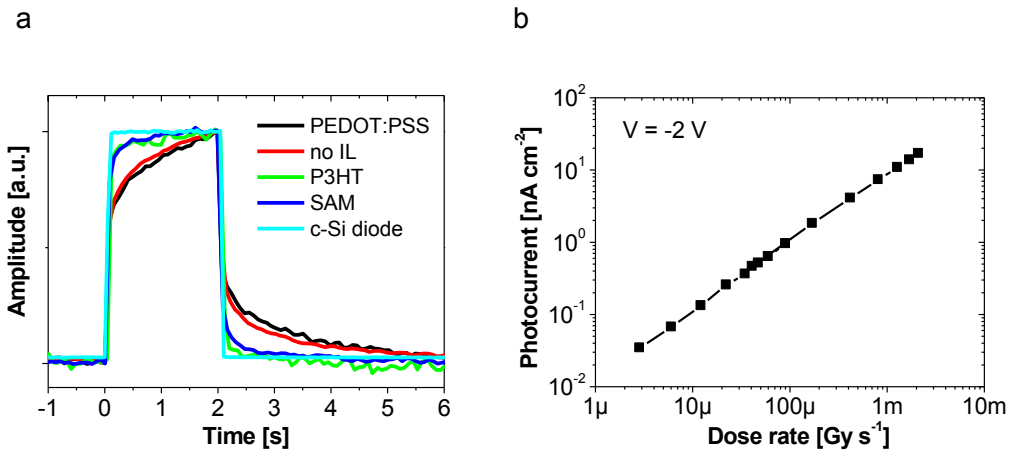

Figure 5.18: IL influence on X-ray measurements with energies of 70 keV and 12 µm GOS thin film thickness for X-ray conversion. a) Sensor response of OPDs polarized at -3 V with PEDOT:PSS, P3HT and SAM ILs and without IL to a single 90 µGy s^{-1} X-ray pulse. b) Sensors response for the OPD with PEDOT:PSS IL reverse biased at -2 V to X-ray pulses from 3 µGy s^{-1} to 2.1 mGy s^{-1}.

The influence of the ILs on the device response time is summarized in Fig. 5.18a, where the normalized sensor response to a 2 seconds X-ray pulse of 90 µGy s^{-1} (70 keV) of OPDs with PEDOT:PSS, P3HT and SAM IL and without IL is compared. Si photoresponse is added as reference. Response times agree well with visible light measurements (cf. Fig. 4.7a) with the fastest transients observed for P3HT and SAM ILs, whereas, PEDOT:PSS ILs and OPD without IL show the longest transients. In Fig. 5.18b the dynamic range of the X-ray sensor is shown with a linear correlation between dose rate and photocurrent from ~3 µGy s^{-1} up to ~2.1 mGy s^{-1}. The lowest detectable X-ray dose is ~3 µGy s^{-1} independent of the IL.

Due to Keithley 2400 hardware limitation to acquire more than ~12 datapoints/sec (distance between datapoints of ~80 ms), from these measurements photocurrent rise/fall time cannot be measure. In order to characterize the photoresponse of the OPDs to short pulses X-ray, a read-out electronic circuit to read the OPD signals with high sampling rate is developed. An important problem to solve is the high dark current load of several nA (depending on the reverse polarization) that restricts the output signal swing. To solve the problem the dark current is compensate to zero implementing a negative feedback amplifier in closed loop configuration.

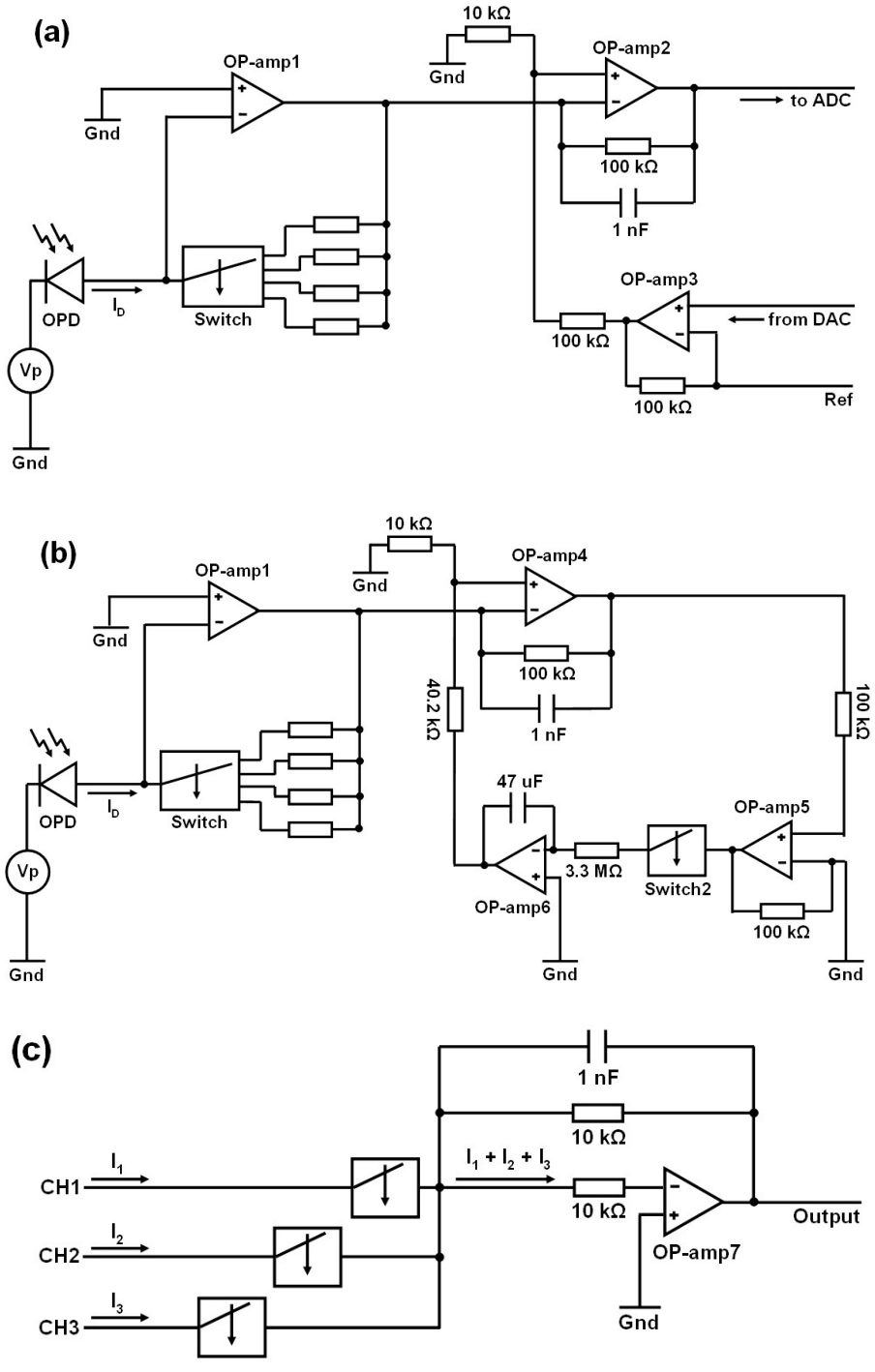

Figure 5.19: a) Digital and b) analog dark current compensation circuit. The OPD is reverse biased. c) Adder circuit with 3 channels (CH1, CH2 and CH3).

The principle of the negative feedback is that the output signal is fed-back to the input and combined with the input signal in order to control the output of the loop. In this way the board output is null when no X-ray pulse is applied and the complete output signal ranging from zero to the voltage supply can be use for the photocurrent measurement.

The dark current compensation has been implemented both analog and digital. A user defined polarization voltage between -2 V and +2 V, Vp in Fig. 5.19a and b, is applied to the cathode electrode and the diode current signal is read from the anode. Current coming from the diode, I_D in Fig. 4(a) and (b), is amplified and converted to a voltage signal by a transimpedance operational amplifier (OP-amp1 in Fig. 5.19a and Fig. 5.19b. The OP-amp1 feedback resistance is chosen by a switch resulting in a variable gain ranging from 10^3 to 10^6 V A^{-1}. For the digital solution, Fig. 5.19a, first the output signal of the OP-amp2 (LMP7721) is measured with a standard 20 Bit-ADC (ADS1248IPWR), scale it with the CPU and than the result is applied to a 16 Bit- DAC (DAC8164IAPW). The result is sent to the non-inverting input of the difference amplifier OP-amp2 through OP-amp3 and operation iterated until the output of OP-amp2 is smaller than 0.3 mV. A reference signal (Ref, Fig 5.19a) is used to keep the unipolar output of the DAC (0 to 2.0 V) to a bipolar value (-2.0 V to +2.0 V). Digital board is equipped with a CPU from Philips (ARM-Cortex-M3 LPC1764FBD100) with 120 MHz clock frequency. For the analog solution, Fig. 5.19b, OP-amp4 output is shorted with its positive input through two additional operational amplifiers (OP-amp5 and OP-amp6). Due to the high OPD current load, a large capacitor of 47 µF is used as feedback for OP-amp6. resulting in a RC time constant for the circuit of ~155 s. Important for the analog solution is Switch2 (ADG801BRT), which is close for dark current compensation and open during X-ray exposure. To drive several OPDs at the same time, in order to test the possibility to measure the data from an array, the circuit is replicated several times. Organic diodes are connected with shorted cathodes, hence the polarization bias is the same for all OPDs. In addition, a switch in every channel allows for diode selection. Signals are added and converted in voltages by a summing operational amplifier with unity gain OP-amp7, Fig. 5.19c. For the feedback loop of OP-amp7 a parallel of 10 kΩ resistor and 1 nF capacitor is used resulting in a fast circuit with RC time constant of ~10^{-5} s. Finally, signals are filtered in both boards. Low pass filtering is implemented using three ADG509 and a TC1563-2. With a USB connection and a PC software the filter cut-off frequencies is set to 0, 1, 5 or 10 kHz

and pole numbers to 1 or 2, which correspond to 20 and 40 dB dec^{-1}, respectively. For an output signal ranging from 0 to +10 V an additional OP-amp is used. To prevent OPD damage and to shield from noise sources, the input stage of the read-out electronic is galvanically separated from the rest of the circuit and the electronic board is placed in a Faraday cage. The digital solution needs less than 2 seconds for a stable signal. This time period is relative short and fits to the ramp-up time of the X-ray source. Instead, the analog board needs about 20 min to stabilize the dark current before the first X-ray signal can be acquired due to the high value of the RC time constant. Note, diodes are kept in dark condition until the current is completely compensated. Fig. 5.20a and 5.20b show the output signal generated by the digital electronic board. Three diodes are connected to the digital board inputs and all switches are set to on. Diodes are reversed biased at -1 V and illuminated with a 1 ms length single green light pulse (532 nm wavelength) with intensity of ~50 nW cm^{-2}, Fig. 5.20a black line. The single pole low-pass filter of the board is set to 5 kHz.

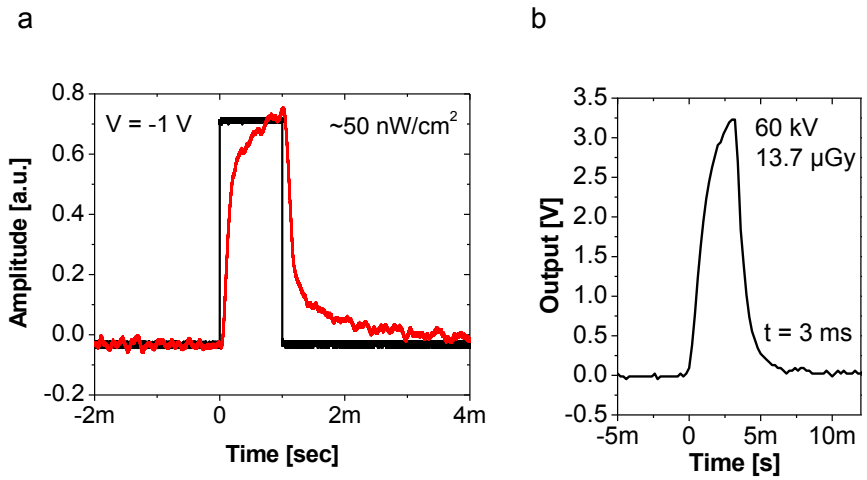

Figure 5.20: Digital board output response to a) 1 ms green light pulse at ~50 nW cm^{-2} and to b) 3 ms X-ray pulse at 60 kV with 13.7 µGy dose rate.

The electronic board reads with a high sampling rate the photocurrent signal from the diodes and generated as output a voltage pulse of ~0.76 V corresponding to a photocurrent value of ~152 nA with a high signal to noise ratio (S/N), Fig. 5.20a red line. Note, that the dark current level of the baseline is correctly compensated.

Finally, with a dedicated electronic capable of reading signals from the large active area OPDs with ms temporal resolution OPDs are characterized under short-pulse X-ray excitation. A 5 cm^2 OPD is reverse biased at -2 V, coupled to a 12 µm thick GOS scintillator and irradiated by a single-short X-ray pulse with 13.7 µGy dose at 60 kV. Fig. 5.20b shows the output of the digital board with no filter applied. A voltage pulse with amplitude of ~3.23 V corresponding to a photocurrent of ~646 nA is read-out. The rise and fall time are ~1.8 ms and ~1.4 ms, respectively. Several X-ray measurements are performed on this diode changing the dose and the X-ray pulse length (from 3 to 30 ms) and no variation of the rise time can be observed. From these measurements a mean OPD sensitivity of ~0.1 mV $µGy^{-1}$ s^{-1} cm^{-2} can be calculated, despite this value can be enhanced by increasing the gain of the amplification stage to match the appropriate requirements of a medical or industrial application.

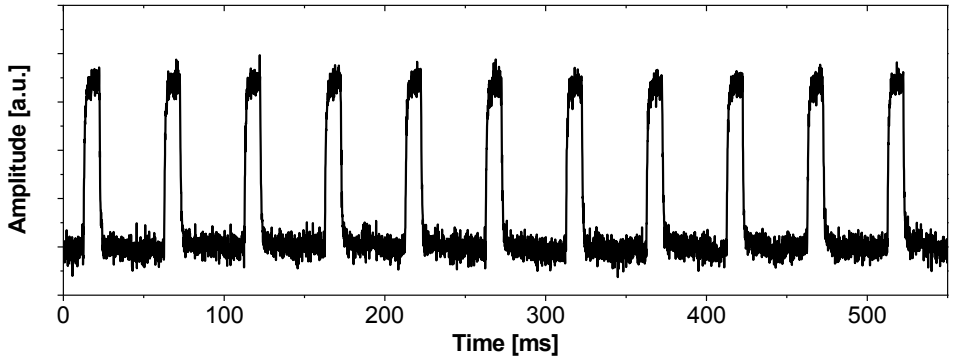

Figure 5.21: Sensor response of an OPD with P3HT IL reverse biased at -5 V and irradiated by 70 keV X-ray train pulses at 420 µGy s^{-1} (10 ms pulse, 50 ms period length).

Minimum rise and fall times of ~1 ms are observed on a 1 cm^2 OPD with P3HT IL reverse biased at -5 V and irradiated with 420 µGy s^{-1} X-ray train pulses with a length of 10 ms and a train period time of 50 ms (Fig. 5.21).

6. Conclusions and outlook

In conclusion spray-coated organic photodiodes with an active area of 1 cm^2 with high EQE > 70 % in the visible range and low dark current densities have been presented. Due to the adopted passivation layer to attenuate ITO rim effects, a low dark current densities of ~10^{-5} mA/cm^2 at -5 V reverse bias has been achieved, which is one order of magnitude lower than the state of the art [Tedde 2009]. It has also been shown that OPDs with a large active area of 5 cm^2 can be fabricated with high reproducibility.

The OPD stack has been completely analyzed and each stack parameter has been varied in order to determine how it influences the OPD characteristics. It has been show how OPD dark current and external quantum efficiency vary with varying parameters such as the semiconductor, cathode or interlayer material, the semiconductor thickness or the active area. In particular has been shown that dynamic response of organic photodiodes deteriorate to a few Hz when reducing the applied light intensity to the low nW/cm^2 range. This phenomena has been observed here for the first time due to the achieved low dark current density that make possible to detect light intensity of a few nW/cm^2. It has been also demonstrated that, contrary to expectation, the diode RC time constant is not the limiting parameter for the cut-off frequency but the trap states became the dominant mechanism at low light intensities. Effortless interface engineering allow, using the same work-flow, to gain 3 orders of magnitude in dynamic response at low light intensities.

Furthermore has been shown that the device active area or the solvent used to fabricate the OPD do not alter significantly parameters such as dark current, EQE and dynamic response. Vice versa the thickness of the active layer modulates the device spectra, in particular with increasing the device active layer thickness the OPD EQE shifts to the near infrared.

It is shown that with the spray-coating technique, low intermix occurs between layers of different materials deposited onto a previous film also if the same solvent is used. As an application, an organic photodiode for NIR sensing based on a low band-gap material with P3HT as interlayer is presented.

The OPDs here presented are suitable for industrial and medical applications, for example the OPD output signal can be used to drive an X-ray shutter.

Finally a read-out electronic to drive 5 cm^2 active area photodiodes with high sampling rate is discussed.

Dark current and dynamic response on organic photodiodes remain challenging compared to c-Si photodiodes. The dark current density of ~10^{-6} mA/cm^2 measured on a 5 cm^2 active area photodiode reverse biased at -5 V indicates that the actual dark current value can be further improved. The most promising way to further reduce the dark current seems to replace the PEDOT:PSS IL with a better electron blocking layer. Despite in this thesis only P3HT and SAM are reported as ILs, many others materials can be tested and it is reasonable to assume that with an improved IL an even better cut-off frequency at low light levels can be achieved. Furthermore the use of a material with better purity can help to improve the performances of the OPDs. With an OPD with a reduced dark current a low light intensities < nW/m^2 and X-ray photons with dose rates in the nGy/s can be potentially detected. OPDs with these performances are of attraction for all the industrial and medical applications where extremely low light detection is needed.

References

[Armstrong 2009] N. R. Armstrong, P. A. Veneman, E. Ratcliff, D. Placencia, M. Brumbach, Oxide Contacts in Organic Photovoltaics: Characterization and Control of Near-Surface Composition in Indium−Tin Oxide (ITO) Electrodes, Acc. Chem. Res., Vol. 42 (11), pp 1748–1757 (2009).

[Admassie 2006] S. Admassie, F. L. Zhang, A. G. Manoj, M. Svensson, M. R. Andersson, and O. Inganas, A polymer photodiode using vapour-phase polymerized PEDOT as an anode, Sol. Energy Mater. Sol. Cells Vol. 90 (2), pp. 133-141 (2006).

[Anderson 1949] Paul A. Anderson, The Work Function of Copper, Phys. Rev. Vol. 76(3), pagg. 388–390 (1949).

[Anishetty 2001] L. Anishetty, Schottky behavior of organic solar cells with different cathode deposition methods, PhD thesis, University of Toledo (2001).

[Arca 2013] F. Arca, S. F. Tedde, M. Sramek, J. Rauh, P. Lugli, O. Hayden, Interface Trap States in Organic Photodiodes. Sci. Rep. 3, 1324 (2013).

[Arca 2013] F. Arca, E. Kohlstädt, S. F. Tedde, P. Lugli, O. Hayden, Large Active Area Organic Photodiodes for Short-Pulse X-ray Detection, IEEE Transactions on electron devices (2013).

[Baierl 2011] D. Baierl, B. Fabel, P. Lugli, G. Scarpa, Efficient indium-tin-oxide (ITO) free topabsorbing organic photodetector with highly transparent polymer top electrode. Org. Electron. Vol. 12, pp. 1669-1673 (2011).

[Balasubramanian 1991] N. Balasubramanian, A. Subrahmanyam, Studies on Evaporated Indium Tin Oxide (ITO)/Silicon Junctions and an Estimation of ITO Work Function, J. Electrochem. Soc., Vol. 138(1), pp. 322-324 (1991).

[Braun 2009] S. Braun, W. R. Salaneck, M. Fahlman, Energy-Level Alignment at Organic/Metal and Organic/Organic Interfaces, Adv. Mater. Vol. 21(14-15) pp.1450-1472 (2009).

[Brown 2003] P. J. Brown, D. S. Thomas, A. Köhler, J. S. Wilson, J.-S. Kim, C. M. Ramsdale, H. Sirringhaus, R. H. Friend, Effect of interchain interactions on the absorption and emission of poly(3-hexylthiophene), Phys. Rev. B, Vol. 67, 064203 (2003).

[Bulliard 2010] X. Bulliard, S.-G. Ihn, S. Yun, Y. Kim, D. Choi, J.-Y. Choi, M. Kim, M. Sim, J.-H. Park, W. Choi, K. Cho, Enhanced Performance in Polymer Solar Cells by Surface Energy Control, Adv. Funct. Mater., Vol. 20, pp. 4381–4387 (2010).

[Beal 2010] R. M. Beal, A. Stavrinadis, J. H. Warner, J. M. Smith, H. E. Assender, A. A. R. Watt, The Molecular Structure of Polymer−Fullerene Composite Solar Cells and Its Influence on Device Performance, Macromolecules, Vol. 43 (5), pp. 2343–2348 (2010).

[Bazkir 2009] Ö. Bazkir, Quantum efficiency determination of unbiased silicon photodiode and photodiode based trap detectors, Rev.Adv.Mater.Sci. Vol. 21, pp. 90-98 (2009).

[Böberl 2007] M. Böberl, M. V. Kovalenko, S. Gamerith, E. J. W. List, W. Heiss, Inkjet-Printed Nanocrystal Photodetectors Operating up to 3 um Wavelengths, Adv. Mater. Vol. 19(21), pp. 3574-3578 (2007).

[Brabec book 2003] C. Brabec, V. Dyakonov, J. Parisi, N. S. Sariciftci, Organic photovoltaics, concepts and realization, Springer (2003).

[Bulliard 2010] Xavier Bulliard , Soo-Ghang Ihn , Sungyoung Yun , Yungi Kim , Dukhyun Choi , Jae-Young Choi , Min Kim , Myungsun Sim , Jong-Hwan Park , Woong Choi , Kilwon Cho, Enhanced Performance in Polymer Solar Cells by Surface Energy Control - Adv. Funct. Mater. Vol. 20, pp. 4381–4387 (2010).

[Bjorstrom 2005] C. M. Björström, A. Bernasik, J. Rysz, A. Budkowski, S. Nilsson, M. Svenssom, M. R. Andersson, K. O. Magnusson, E. Moons, Multilayer formation in spin-coated thin films of low-bandgap polyfluorene:PCBM blends, J. Phys.: Condens. Matter Vol. 17, No. 50, L529 (2005).

[Campoy-Quilles 2008] M. Campoy-Quilles, T. Ferenczil, T. Agostinelli, P. G. Etchegoin, Y. Kim, T. D. Anthopoulos, P. N. Stavrinou, D. D. C. Bradley, J. Nelson, Morphology evolution via self-organization and lateral and vertical diffusion in polymer:fullerene solar cell blends, Nature Materials, Vol. 7, pp. 158-164 (2008).

[Chen 2010] E. Chen, C. Chang, J. Shieh, S. Tseng, H. Meng, C. Hsu, S. Horng, Polymer photodetector with voltage-adjustable photocurrent spectrum Appl. Phys. Lett. 96, 043507 (2010).

[Chu 2006] C. Chu, V. Shrotriya, G. Li, Y. Yang, Tuning acceptor energy level for efficient charge collection in copper-phthalocyanine-based organic solar cells, Appl. Phys. Lett. 88, 153504 (2006).

[Coakley 2004] K. M. Coakley, M. D. McGehee, Conjugated Polymer Photovoltaic Cells, Chem. Mater. Vol. 16 (23), pp 4533–4542 (2004).

[Chen 2010] En-Chen Chen, Chia-Yu Chang, Ji-Ting Shieh, Shin-Rong Tseng, Hsin-Fei Meng, Chain-Shu Hsu, Sheng-Fu Horng, Polymer photodetector with voltage-adjustable photocurrent spectrum, Appl. Phys. Lett. 96, 043507 (2010).

[Cha 2010] H. Cha, H. Kong, D. S. Chung, W. M. Yun, T. K. An, J. Hwang, Y. Kim, H. Shim, C. E. Park, Thermally stable amorphous polymeric semiconductors containing fluorene and thiophene for use in organic photovoltaic cells, Org. Electron., Vol. 11 pp. 1534–1542 (2010).

[Chen 2011] L. Chen, X. Yu, P. Chen, P. Wang, X. Gu, J. Lu, D. Yang, Effect of oxygen precipitation on the performance of Czochralski silicon solar cells, Solar Energy Materials & Solar Cells, Vol. 95, pp. 3148–3151 (2011).

[Coe 2002] S. Coe, W.-K. Woo, M. Bawendi, V. Bulović, Electroluminescence from single monolayers of nanocrystals in molecular organic devices, Nature Vol. 420, pp. 800-803 (2002).

[da Silva 2008] A. A. da Silva, M. A. Cebim, M. Rosaly, Excitation mechanisms and effects of dopant concentration in Gd2O2S:Tb3+ Phosphor, Journal of Luminescence, Vol.128, pp. 1165–1168 (2008).

[de Boer 2005] B. de Boer, A. Hadipour, M. M. Mandoc, T. van Woudenbergh, P. W. M. Blom, Tuning of Metal Work Functions with Self-Assembled Monolayers, Adv. Mater. Vol. 17 (5), pp. 621-625 (2005).

[de Jong 2000] M. P. de Jong, L. J. Ijzendoorn, M. J. A. de Voigt, Stability of the interface between indium–tin–oxide and poly(3,4-ethylenedioxythiophene)/poly(styrene-sulfonate) in polymer light-emitting diodes, Appl. Phys. Lett., 77, 2255 (2000).

[Dennler 2009] G. Dennler, M. C. Scharber, C. J. Brabec, Polymer-Fullerene Bulk-Heterojunction Solar Cells, Adv. Mater., Vol. 21 (13), pp. 1323–1338 (2009).

[Erlangen Temp] http://www.hawo.stw.uni-erlangen.de/

[Fukuda 1999] M. Fukuda, “Optical semiconductor device,” 1st ed. Wiley-Interscience, J. Willey & Sons Inc. New York, 1999.

[Friedel 2009] B. Friedel, P. E. Keivanidis, T. J. K. Brenner, A. Abrusci, C. R. McNeill, R. H. Friend, N. C. Greenham, Effects of Layer Thickness and Annealing of PEDOT:PSS Layers in Organic Photodetectors, Macromolecules, Vol. 42 (17), pp 6741–6747 (2009).

[Girtan 2013] M. Girtan, On the stability of the electrical and photoelectrical properties of P3HT and P3HT:PCBM blends thin films, Organic Electronics Vol. 14 (1), pp. 200–205 (2013).

[Guerrero 2012] A. Guerrero, T. Ripolles-Sanchis, P. P. Boix, G. Garcia-Belmonte, Series resistance in organic bulk-heterojunction solar devices: Modulating carrier transport with fullerene electron traps, Org. Electron. Vol. 13 pp.2326–2332 (2012).

[Graeve] T. Graeve, G. P. Weckler, Large Area Digital X-ray Specific Imagers, Rad-icon Imaging Corp.

[He 2012] Y. He, C. Chen, E. Richard, L. Dou, Y. Wu, G. Li, Y. Yang, Novel fullerene acceptors: synthesis and application in low band gap polymer solar cells J. Mater. Chem., Vol. 22, pp. 13391-13394 (2012).

[Heriot 2005] S. Y. Heriot, R. A. L. Jones, An interfacial instability in a transient wetting layer leads to lateral phase separation in thin spin-cast polymer-blend films, Nat. Mater. Vol. 4, pp. 782 - 786 (2005).

[Hiramoto 1993] M. Hiramoto, T. Imahigashi, M. Yokoyama, Photocurrent multiplication in organic pigment films, Appl. Phys. Lett. Vol. 64, 187 (1993).

[Hiramoto 2002] M. Hiramoto, A. Miki, M. Yoshida, M. Yokoyama, Photocurrent multiplication in organic single crystals, Appl. Phys. Lett. Vol. 81, 8 pp. 1500-1502 (2002).

[Huang 2005] J. Huang, G. Li, Y. Yang, Influence of composition and heat traitment on the vharge transport properties of poly(3-hexylthiophene) and [6,6]-phenyl c61-butiric acid methyl ester blends, Applied Physic Letters 87, 112105 (2005).

[Huang 2007] J. Huang, Y. Yang, Origin of photomultiplication in C60 based devices, Applied Physic Letters 91, 203505 (2007).

[Hwang 2007] I.-W. Hwang, C. Soci, D. Moses, Z. Zhu, D. Waller, R. Gaudiana, C. J. Brabec, A.J. Heeger, Ultrafast Electron Transfer and Decay Dynamics in a Small Band Gap Bulk Heterojunction Material, Adv. Mater., Vol. 19(17), pp. 2307-2312 (2007).

[Hamamatsu] http://www.hamamatsu.com

[Invitrogen] http://www.invitrogen.com/

[Itaka 2006] K. Itaka, M. Yamashiro, J. Yamaguchi, M. Haemori, S. Yaginuma, Y. Matsumoto, M. Kondo, H. Koinuma, High-Mobility C60 Field-Effect Transistors Fabricated on Molecular- Wetting Controlled Substrates, Advanced Materials, Vol. 18(13), pp. 1713-1716 (2006).

[Katsume 1996] T. Katsume, M. Hiramoto, M. Yokoyama, Photocurrent multiplication in naphthalene tetracarboxylic anhydride film at room temperature, Appl. Phys. Lett. Vol.69(24), 3722 (1996).

[Kasap 2002] S. O. Kasap, J. A. Rowlands, Direct-Conversion Flat-Panel X-Ray Image Sensors for Digital Radiography, Proceedings of the ieee, Vol. 90, No. 4, pp. 591-604 (2002).

[Kang 1997] I. Kang, F. W. Wise, Electronic structure and optical properties of PbS and PbSe quantum dots, J. Opt. Soc. Am. B/ Vol. 14, 7 (1997).

[Kim 2006] D. H. Kim, Y. Jang, Y. D. Park, K. Cho, Layered Molecular Ordering of Self-Organized Poly(3-hexylthiophene) Thin Films on Hydrophobized Surfaces, Macromolecules, Vol. 39, pp. 5843-5847 (2006).

[Kim 2006] H. Kim, W. So, S. Moon, Effect of Thermal Annealing on the Performance of P3HT/PCBM Polymer Photovoltaic Cells, Journal of the Korean Physical Society, Vol. 48 (3), pp. 441-445 (2006).

[Kim 2007] J. Y. Kim, K. Lee, N. E. Coates, D. Moses, T. Nguyen, M. Dante, A. J. Heeger, Efficient tandem polymer solar cells fabricated by all-solution processing Science, 317, 5835, pp. 222-225 (2007).

[Kim 2007] J. S. Kim, J. H. Park, J. H. Lee, J. Jo, D.Y. Kim, K. Cho, Control of the electrode work function and active layer morphology via surface modification of indium tin oxide for high efficiency organic photovoltaics, Appl. Phys. Lett. 91, 112111 (2007).

[Konstantatos 2006] G. Konstantatos, I. Howard, A. Fischer, S. Hoogland, J. Clifford, E. Klem, L. Levina, E. H. Sargent, Ultrasensitive solution-cast quantum dot photodetectors, Nature 442, pp. 180-183 (2006).

[Konstantatos 2007] G. Konstantatos, J. Clifford, L. Levina, E. H. Sargent, Sensitive solution-processed visible-wavelength photodetectors. Nature Photon. Vol. 1, pp. 531-534 (2007).

[Klimov 2000] V. I. Klimov, A. A. Mikhailovsky, Su Xu, A. Malko, J. A. Hollingsworth, C. A. Leatherdale, H.-J. Eisler, M. G. Bawendi, Optical gain and stimulated emission in nanocrystal quantum dots, Science 290, pp. 314-317 (2000).

[Klimov 2006] E. Klimov, W. Li, X. Yang, G. G. Hoffmann, J. Loos, Scanning Near-Field and Confocal Raman Microscopic Investigation of P3HT-PCBM Systems for Solar Cell Applications, Macromolecules, Vol. 39(13), pp. 4493-4496 (2006).

[Keivanidis 2008] P. E. Keivanidis, N. C. Greenham, H. Sirringhaus, R. H. Friend, J. C. Blakesley, R. Speller, M. Campoy–Quiles, T. Agostinelli, D. D. C. Bradley, J. Nelson, X-ray stability and response of polymeric photodiodes for imaging applications, Appl. Phys. Lett. 92, 023304 (2008).

[Lee 2011] K. H. Lee, C. H. Park, K. Lee, Taewoo Ha, Jae Hoon Kim, J. Yun, G.-H. Lee, S. Im, Semi-transparent organic/inorganic hybrid photo-detector using pentacene/ZnO diode connected to pentacene transistor, Organic Electronics Vol. 12(7), pp. 1103–1107 (2011).

[Lian 2008] J. Lian, X. Sun, T. Gao, Q. Li, X. Li, Z. Liu, Preparation of Gd2O2S:Pr Scintillation ceramics by Pressureless Reaction Sintering Method, Journal of materials science & technology, Vol. 25, No. 2, p. 254-259 (2009).

[Liang 2009] C.-W. Liang, W.-F. Su, L. Wang, Enhancing the photocurrent in poly(3-hexylthiophene)/[6,6]-phenyl C61 butyric acid methyl ester bulk heterojunction solar cells by using poly(3-hexylthiophene) as a buffer layer, Applied Physics Letters 95, 133303 (2009).

[Li 2008] W. Li, J. Guo, X. Sun, B. Zhou, Improvement of power efficiency of polymer solar cell based on P3HT: PCBM blends, Proc. of SPIE, Solid State Lighting and Solar Energy Technologies, Vol. 6841 68411G-1 (2008).

[Li 2004] G. Li, V. Shrotriya, J. S. Huang, Y. Yao, T. Moriarty, K. Emery, and Y. Yang, High-efficiency solution processable polymer photovoltaic cells by self-organization of polymer blends, Nature Materials 4, pp. 864 - 868 (2005).

[Liang 2009] C. Liang, W. Su, L. Wang, Enhancing the photocurrent in poly(3-hexylthiophene)/[6,6]-phenyl C61 butyric acid methyl ester bulk heterojunction solar cells by using poly(3-hexylthiophene) as a buffer layer, Appl. Phys. Lett., 95, 133303 (2009).

[Lunt 2011] R. R. Lunt, V. Bulovic, Transparent, near-infrared organic photovoltaic solar cells for window and energy-scavenging applications, Applied Physics Letters 98, 113305 (2011).

[Law 2008] M. Law, M. C. Beard, S. Choi, J. M. Luther, M. C. Hanna, A. J. Nozik, Determining the Internal Quantum Efficiency of PbSe Nanocrystal Solar Cells with the Aid of an Optical Model, Nano Letters, Vol. 8(11), pp. 3904-3910 (2008).

[Marsh 2010] R. A. Marsh, J. M. Hodgkiss, S. Albert-Seifried, R. H. Friend, Effect of Annealing on P3HT:PCBM Charge Transfer and Nanoscale Morphology Probed by Ultrafast Spectroscopy, Nano Lett. Vol. 10(3), pp. 923–930 (2010).

[Michaelson 1977] H. B. Michaelson, The work function of the elements and its periodicity, J. Appl. Phys. Vol. 48(11), pp.4729 (1977).

[Mihailetchi 2003] V. D. Mihailetchi, P. W. M. Blom, J. C. Hummelen, M. T. Rispens, Cathode dependence of the open-circuit voltage of polymer:fullerene bulk heterojunction solar cells, J. Appl. Phys. Vol. 94(10), pp.6849 (2003);

[Mühlbacher 2006] D. Mühlbacher, M. Scharber, M. Morana, Z. Zhu, D. Waller, R. Gaudiana, C. Brabec, High Photovoltaic Performance of a Low-Bandgap Polymer, Adv. Mater., 18, 22 (2006).

[Meijer 2003] E. J. Meijer, D. M. de Leeuw, S. Setayesh, E. van Veenendaal, B. -H. Huisman, P. W. M. Blom, J. C. Hummelen, U. Scherf, T. M. Klapwijk, Solution-processed ambipolar organic field-effect transistors and inverters, Nature Materials, Vol. 2, pp. 678-682 (2003).

[Morana 2008] M. Morana, M. Wegscheider, A. Bonanni, N. Kopidakis, S. Shaheen, M. Scharber, Z. Zhu, D. Waller, R. Gaudiana, C. Brabec, Bipolar Charge Transport in PCPDTBT-PCBM Bulk-Heterojunctions for Photovoltaic Applications, Adv. Funct. Mater., 18, 12 (2008).

[Nardes 2007] Alexandre Mantovani Nardes, On the conductivity of PEDOT:PSS thin films, Eindhoven: Technische Universiteit Eindhoven (2007).

[Nakamura 2005] J. Nakamura, K. Murata, K. Takahashi, Relation between carrier mobility and cell performance in bulk heterojunction solar cells consisting of soluble polythiophene and fullerene derivatives, Appl. Phys. Lett., 87, 132105 (2005).

[Nakayama 2000] K. Nakayama, M. Hiramoto, M. Yokoyama, A high-speed photocurrent multiplication device based on an organic double-layered structure, Appl. Phys. Lett. Vol. 76, 1194 (2000).

[Ngo 2012] T. T. Ngo, D. N. Nguyen, V. T. Nguyen, Glass transition of PCBM, P3HT and their blends in quenched state, Adv. Nat. Sci: Nanosci. Nanotechnol. 3, 045001 (2012).

[Nagarajan 2008] S. Nagarajan, J. Kumar, F. F. Bruno, L. A. Samuelson, R. Nagarajan, Biocatalytically Synthesized Poly(3,4-ethylenedioxythiophene), Macromolecules, Vol. 41, pp. 3049-3052 (2008).

[Ng 2008] T. N. Ng, W. S. Wong, M. L. Chabinyc, S. Sambandan, R. A. Street, Flexible image sensor array with bulk heterojunction organic photodiode, Appl. Phys. Lett., Vol. 92, 213303 (2008).

[Osikowicz 2007] W. Osikowicz, M. de Jong, W. Salaneck, Formation of the Interfacial Dipole at Organic-Organic Interfaces: C_{60}/Polymer Interfaces, Adv. Mater., Vol. 19(23), pp. 4213-4217 (2007).

[Oh 2011] J. Y. Oh, W. S. Jang, T. I. Lee, J. Myoung, H. K. Baik, Driving vertical phase separation in a bulk-heterojunction by inserting a poly(3-hexylthiophene) layer for highly efficient organic solar cells, Appl. Phys. Lett., 98, 023303 (2011).

[Pacholski 2002] C. Pacholski, A. Kornowski, H. Weller, Self-Assembly of ZnO: From Nanodots to Nanorods, Chem. Int. Ed. Vol. 41(7), pp. 1188-1191 (2002).

[Park 2010] J. H. Park, T.-W. Lee, B.-D. Chin, D. H. Wang, O O. Park, Roles of Interlayers in Efficient Organic Photovoltaic Devices, Macromol. Rapid Commun., Vol. 31, pp. 2095–2108 (2010).

[Parker 1994] I. D. Parker, Carrier tunneling and device characteristics in polymer light emitting diodes, J. Appl. Phys. Vol. 75(3), pp.1656-1666 (1994);

[Perzon 2007] E. Perzon, F. Zhang, M. Andersson, W. Mammo, O. Inganäs, M. R. Andersson, A Conjugated Polymer for Near Infrared Optoelectronic Applications, Adv. Mater., 19, 20 (2007).

[Piris 2009] J. Piris, T. E. Dykstra, A. A. Bakulin, P. H. M. van Loosdrecht, W. Knulst, M. T. Trinh, J. M. Schins, L. D. A. Siebbeles, Photogeneration and Ultrafast Dynamics of Excitons and Charges in P3HT/PCBM Blends J. Phys. Chem. C, Vol. 113 (32), pp. 14500–14506 (2009).

[Parkinson 2008] P. Parkinson, J. Lloyd-Hughes, M. B. Johnston, L. M. Herz, Efficient generation of charges via below-gap photoexcitation of polymer-fullerene blend films investigated by terahertz spectroscopy, Phys. Rev. B, 78, 115321 (2008).

[Quiles 2008] M. C. Quiles, T. Ferenczi, T. Agostinelli, P. G. Etchegoin, Y. Kim, T. D. Anthopoulos, P. N. Stavrinou, D. D. C. Bradley, J. Nelson, Morphology evolution via self-organization and lateral and vertical diffusion in polymer:fullerene solar cell blends, Nat. Mater., Vol. 7, pp. 158–164 (2008).

[Ray 2011] B. Ray, P. R.Nair, M. A. Alam, Annealing dependent performance of organic bulk-heterojunction solar cells: A theoretical perspective, Solar Energy Materials& Solar Cells, Vol. 95(12), pp.3287–3294 (2011).

[Rauch PhD] T. Rauch, Spectral Enhancement of Organic Photodetectors, PhD Thesis, Karlsruher Instituts für Technologie (2012).

[Rauch 2009] T. Rauch, M. Böberl, S. F. Tedde, J. Fürst, M. V. Kovalenko, G. Hesser, U. Lemmer, W. Heiss, O. Hayden, Near-infrared imaging with quantum-dotsensitized organic photodiodes, Nature Photonics 3, pp. 332-336 (2009).

[Ramuz 2008] Marc Ramuz, Lukas Burgi, Carsten Winnewisser, Peter Seitz, High sensitivity organic photodiodes with low dark currents and increased lifetimes, Org. Electron. Vol. 9, pp. 369–376 (2008).

[Roncali 1997] J. Roncali, Synthetic Principles for Bandgap Control in Linear pi-Conjugated Systems, Chem. Rev., 97 (1), pp. 173-206 (1997).

[Rogero 2002] C. Rogero, J. I. Pascual, J. Gomez-Herrero, and A. M. Baro, Resolution of site-specific bonding properties of C60 adsorbed on Au(111), J. Chem. Phys., Vol. 116, pp. 832 (2002).

[Roman 1998]. L. S. Roman, W. Mammo, L. A. A. Pettersson, M. R. Andersson, O. Inganas, High Quantum Efficiency Polythiophene, Adv. Mater. Vol. 10(10), pp. 774-777 (1998).

[Sariciftci 1992] N. S. Sariciftci, L. Smilowitz, A. J. Heeger, F. Wudl, Photoinduced Electron Transfer from a Conducting Polymer to Buckminsterfullerene, Science, Vol. 258(5087), pp. 1474-1476 (1992).

[Snaith 2006] H. J. Snaith, L. Schmidt-Mende, M. Grätzel, Light intensity, temperature, and thickness dependence of the open-circuit voltage in solid-state dye-sensitized solar cells, Phys. Rev. B Vol. 74(4), 045306 (2006).

[Soci 2007] C. Soci, I. -W. Hwang, D. Moses, Z. Zhu, D. Waller, R. Gaudiana, C. J. Brabec, A. J. Heeger, Photoconductivity of a Low-Bandgap Conjugated Polymer, Adv. Funct. Mater., 17, 4, pp. 632-636 (2007).

[Strehlow 1973] W. H. Strehlow, E. L. Cook, Compilation of Energy Band Gaps in Elemental and Binary Compound Semiconductors and Insulators, J. Phys. Chem. Ref. Data, Vol. 2(1), pp. 163-201 (1973).

[Sargent 2005] E. H. Sargent, Infrared Quantum Dots, Adv. Mater. Vol. 17(5), pp. 515-522 (2005).

[sigmaaldrich.com] http://www.sigmaaldrich.com/

[Schafferhans PhD] J. Schafferhans, Investigation of defect states in organic semiconductors: Towards long term stable materials for organic photovoltaics, PhD thesis, Würzburg (2011).

[Shaw 2008] P. E. Shaw, A. Ruseckas, I. D. W. Samuel, Exciton diffusion measurements in poly(3- hexylthiophene), Adv. Mater., Vol. 20(18), pp.3516-3520 (2008).

[Sirringhaus 1999] H. Sirringhaus, P. J. Brown, R. H. Friend, M. M. Nielsen, K. Bechgaard, B. M. W. Langeveld-Voss, A. J. H. Spiering, R. A. J. Janssen, E. W. Meijer, P. Herwig, D. M. de Leeuw, Two-dimensional charge transport in self-organized, high-mobility conjugated polymers, Nature, Vol. 401, pp. 685-688 (1999).

[Street 2008] T. N. Ng, W. S. Wong, M. L. Chabinyc, S. Sambandan, R. A. Street, Flexible image sensor array with bulk heterojunction organic photodiode, Appl. Phys. Lett., 92, 213303 (2008).

[Savenije 2006] T. J. Savenije, J. E. Kroeze, X. Yang, J. Loos, The formation of crystalline P3HT fibrils upon annealing of a PCBM : P3HT bulk heterojunction, Thin Solid Films, Vol. 511-512, pp. 2-6 (2006).

[Sukhovatkin 2009] V. Sukhovatkin, S. Hinds, L. Brzozowski, E. H. Sargent, Colloidal quantum-dot photodetectors exploiting multiexciton generation, Science Vol. 324, pp. 1542-1544 (2009).

[Street 2011] R. A. Street, K. W. Song, S. R. Cowan, Influence of series resistance on the photocurrent analysis of organic solar cells, Org. Electron. 12, pp. 244–248 (2011).

[Sze book 1969] S. M. Sze, K. K. Ng, Physics of Semiconductor Devices (1969).

[Soci 2007] C. Soci, I. -W. Hwang, D. Moses, Z. Zhu, D. Waller, R. Gaudiana, C. J. Brabec, A. J. Heeger, Photoconductivity of a Low-Bandgap Conjugated Polymer, Adv. Funct. Mater., Vol. 17, 4, pp. 632-636 (2007).

[Tedde 2009] S. Tedde, J. Kern, T. Sterzl, J. Furst, P. Lugli, O. Hayden, Fully Spray Coated Organic Photodiodes, Nano letters, Vol. 9(3), pp. 980-983 (2009).

[Thielsch 1998] R. Thielsch, T. Bohme, R. Reiche , D. Schlafer, H.-D. Bauer, H. Bottcher, Quantum-size effects of PbS nanocrystallites in evaporated composite films, Nanostructured Materials. Vol. 10(2), pp. 131-149 (1998).

[Thompson 2008] B. C. Thompson, J. M. J. Frechet, Polymer–Fullerene Composite Solar Cells, Angew. Chem. Int. Ed., Vol. 47(1), pp. 58–77 (2008).

[Tang 2011] J. A. Tang, E. H. Sargent, Infrared colloidal quantum dots for photovoltaics: Fundamentals and recent progress. Adv. Mater. Vol. 23(1), pp. 12-29 (2011).

[Tang 2011] J. Tang, K. Kemp, S. Hoogland, K. S. Jeong, H. Liu, L. Levina, M. Furukawa, X. Wang, R. Debnath, D. Cha, K. W. Chou, A. Fischer, A. Amassian, J. B. Asbury, E. H. Sargent, Colloidal-quantum-dot photovoltaics using atomic-ligand passivation, Nature Materials, Vol. 10, pp. 765 (2011).

[Tang 1986] C. W. Tang, Two-layer organic photovoltaic cell, Applied Physics Letters, Vol. 48, pp. 183-185 (1986).

[Tedde PhD] S. F. Tedde, Design, fabrication and characterization of organic photodiodes for industrial and medical applications, PhD thesis, Technischen Universität München, 2009.

[Urdaneta 2011] M. Urdaneta, P. Stepanov, I. Weinberg, I. Pala, S. Brock, Quantum Dot Composite Radiation Detectors, Photodiodes - World Activities in 2011, Prof. Jeong Woo Park (Ed.), ISBN: 978-953-307-530-3 (2011).

[van Mullekom 2001] H. A. M. van Mullekom, J. A. J. M. Vekemans, E. E. Havinga, E. W. Meijer, Developments in the chemistry and band gap engineering of donor–acceptor substituted conjugated polymers , Mater. Sci. Eng. R, Vol. 32(1), pp. 1–40 (2001).

[von Hauff 2006] E. von Hauff, J. Parisi, V. Dyakonov, Investigations of the effects of tempering and composition dependence on charge carrier field effect mobilities in polymer and fullerene films and blends, J. Appl. Phys., 100, 043702 (2006).

[Wang 1987] Y. Wang, A. Suna, W. Mahler, R. Kasowski, PbS in polymers. From molecules to bulk solids, J. Chem. Phys., 87, 7315 (1987).

[Wienk 2006] M. M. Wienk, M. G. R. Turbiez, M. P. Struijk, M. Fonrodona, R. A. J. Janssen, Low-band gap poly(di-2-thienylthienopyrazine):fullerene solar cells, Appl. Phys. Lett., 88, 153511 (2006).

[Wise 2000] F.W. Wise, Lead Salt Quantum Dots: the Limit of Strong Quantum Confinement, Acc. Chem. Res., Vol. 33(11) pp. 773-780 (2000).

[Xu 2009] Y. Xu, Y. Wang, J. Liang, Y. Huang, Y. Ma, X. Wan, Y. Chen, A Hybrid Material of Graphene and Poly (3,4-thyldioxythiophene) with High Conductivity, Flexibility, and Transparency, Nano Res, Vol. 2, pp. 343 348 (2009).

[Xu 2009] Zheng Xu, Li-Min Chen, Guanwen Yang, Chun-Hao Huang, Jianhui Hou, Yue Wu, Gang Li, Chain-Shu Hsu, Yang Yang, Vertical Phase Separation in Poly(3-hexylthiophene): Fullerene Derivative Blends and its Advantage for Inverted Structure Solar Cells, Adv. Funct. Mater., Vol. 19, pp. 1227–1234 (2009).

[Yu 1995] G. Yu, J. Gao, J. C. Hummelen, F. Wudl, and A. J. Heeger, Polymer Photovoltaic Cells: Enhanced Efficiencies via a Network of Internal Donor-Acceptor Heterojunctions, Science Vol. 270, pp.1789-1791 (1995).

[Yao 2007] Y. Yao, Y. Liang, V. Shrotriya, S. Xiao, L. Yu, Y. Yang, Plastic Near-Infrared Photodetectors Utilizing Low Band Gap Polymer, Adv. Mater., Vol. 19, 22, pp. 3979-3983 (2007).

[Yao 2008] Y. Yao, J. Hou, Z. Xu, G. Li, Y. Yang, Effects of Solvent Mixtures on the Nanoscale Phase Separation in Polymer Solar Cells, Adv. Funct. Mater., Vol. 18, pp. 1783-1789 (2008).

[Yoo 2011] S. H. Yoo, J. M. Kum, S. O Cho, Tuning the electronic band structure of PCBM by electron irradiation, Nanoscale Res Lett., Vol. 6(1), pp. 545 (2011).

[Yang 2008] C. Yang, P. Tsai, S. Horng, K. Lee, S. Tzeng, H. Meng, J. Shy, C. Shu, Infrared photocurrent response of charge-transfer exciton in polymer bulk Heterojunction, Appl. Phys. Lett., 92, 083504 (2008).

[Zaus 2008] E. S. Zaus, S. Tedde, T. Rauch, J. Furst, G. H. Dohler, Design of highly transparent organic photodiodes, IEEE Trans. on Electr. Devic., Vol. 55(2), pp. 681-684 (2008).

[Zoombelt 2008] A. P. Zoombelt, M. Fonrodona, M. M. Wienk, A. B. Sieval, J. C. Hummelen, R. A. J. Janssen, Photovoltaic Performance of an Ultrasmall Band Gap Polymer, Organic Letters, Vol. 11, No. 4, pp. 903-906 (2009).

[Zhou 2007] Y. F. Zhou, Y. B. Yuan, L. F. Cao, J. Zhang, H. Q. Pang, J. R. Lian, X. Zhou, Improved stability of OLEDs with mild oxygen plasma treated PEDOT:PSS, Journal of Luminescence, Vol. 122-123, pp. 602-604 (2007).

[Zasavitskii 2004] I. I. Zasavitskii, E. A. de Andrada e Silva, E. Abramof, P. J. McCann, Optical deformation potentials for PbSe and PbTe, Phys. Rev. B 70, 115302 (2004).

List of abbreviations

BHJ	**B**ulk **h**etero**j**unction
IL	**I**nter**l**ayer
ITO	**I**ndium **T**in **O**xide
OPD	**O**rganic **p**hoto**d**iode
P3HT	**P**oly(**3**-**h**exyl-**t**hiophene)
PCBM	[6,6]-**p**henyl-**C**61-**b**utyric-**m**ethyl-ester
PCPDTBT	Poly[2,6-(4,4-bis-(2-ethylhexyl)-4H-cyclopenta[2,1-b;3,4-b']dithiophene)-alt-4,7-(2,1,3-benzothiadiazole)]
PD	**P**hoto**d**iode
PEDOT:PSS	Poly(3,4-ethylenedioxythiophene) poly(styrenesulfonate)
SAM	**S**elf-**A**ssembled **M**onolayer

Acknowledgements

Ajuria Jon
Bingart Evi
Buechele Patric
Endner Tobias
Fischer Rene
Hartmann David
Hayden Oliver
Helou Michael
Leberl Daniela
Littarru Gaia
Pflaum Regina
Reisbeck Mathias
Richter Andre
Richter Lukas
Richter Moses
Sramek Maria
Schmidt Oliver
Szyszkowski Sabine
Tedde Sandro
Wegler Barbara
Ye Shuyun
Zoli Guido